UCLA
UCLA Electronic Theses and Dissertations

Title
The Study Of Galaxy Formation And The Development Of MOSFIRE

Permalink
https://escholarship.org/uc/item/06q8t6pv

Author
Kulas, Kristin Rose

Publication Date
2013

Peer reviewed|Thesis/dissertation

eScholarship.org Powered by the California Digital Library
University of California

University of California
Los Angeles

The Study Of Galaxy Formation And The Development Of MOSFIRE

A dissertation submitted in partial satisfaction
of the requirements for the degree
Doctor of Philosophy in Astronomy

by

Kristin Rose Kulas

2013

© Copyright by
Kristin Rose Kulas
2013

Abstract of the Dissertation

The Study Of Galaxy Formation And The Development Of MOSFIRE

by

Kristin Rose Kulas

Doctor of Philosophy in Astronomy

University of California, Los Angeles, 2013

Professor Ian S. McLean, Chair

The epoch of $z \sim 2-3$ is a noticeably more active time in our universe for galaxies, with the global star-formation rate density at its peak (Madau et al. 1996; Bouwens et al. 2009). Galaxies during this era are experiencing many internal and external processes such as large-scale outflows from star formation or active galactic nuclei (AGN) activity, inflows from cool gas, and mergers, which can alter the properties (e.g., structure, metallicity, star-formation rate, velocity dispersion) and evolution of galaxies. This elevated level of activity makes $z \sim 2-3$ objects ideal for examining galaxy formation. In the rest-frame optical many important diagnostic lines exist that allow one to study galaxy properties, including the Balmer series, [O III]$\lambda\lambda$5007,4959 and [N II]λ6584. For galaxies at $z \sim 2-3$, however, these lines will become very faint and shift into the near-infrared wavelength regime. As a consequence of this, near-infrared spectroscopy on a large telescope plays an integral role in studying high-redshift galaxies. For my thesis I have used near-infrared spectroscopy, acquired at the Keck Observatory, to study in depth how gas supplies are regulated during the formation of galaxies. Simultaneously, I have also worked to bring to realization one of the

most advanced near-IR spectrographs for the astronomical community through my instrumentation research on MOSFIRE, the Multi-Object Spectrometer For Infrared Exploration.

The dissertation of Kristin Rose Kulas is approved.

Edward D. Young

Edward L. Wright

Alice E. Shapley

Ian S. McLean, Committee Chair

University of California, Los Angeles

2013

To my family for their love, support, and believing that I could embrace the stars and beyond

Table of Contents

Abstract . . . . **ii**

Table of Contents . . . . **vi**

List of Figures . . . . **x**

List of Tables . . . . **xiii**

1 Introduction **1**

1.1 Project I: The Kinematics Of Multiple-Peaked Lyα Emission In Star-Forming Galaxies At $z \sim 2-3$ 5

1.2 Project II: Performance Of The HgCdTe Detector For MOSFIRE, An Imager And Multi-Object Spectrometer For Keck Observatory 7

1.3 Project III: A Detailed Study Of Galaxies In A High-Redshift Protocluster With MOSFIRE 9

2 The Kinematics Of Multiple-Peaked Lyα Emission In Star-Forming Galaxies At $z \sim 2-3$ **12**

2.1 Introduction 12

2.2 Sample Selection 15

2.3 Observations And Data Reduction 19

2.3.1 NIRSPEC Observations And Data Reduction 19

2.3.2 LRIS Data Reduction 27

2.3.3 Line Centroid, Flux, And FWHM Measurements 28

2.4 Lyα Velocity Profiles . . . 29
2.5 Physical Quantities . . . 36
2.5.1 Velocity Dispersion . . . 38
2.5.2 Dust Extinction . . . 39
2.5.3 Star-Formation Rates And Intrinsic Luminosity . . . 44
2.5.4 Interstellar Absorption . . . 46
2.6 Lyα Radiative Transfer Modeling . . . 52
2.6.1 Models . . . 52
2.6.2 Comparison Between Models And Observations . . . 53
2.6.3 Additional Considerations And Caveats . . . 61
2.7 Summary And Discussion . . . 64

3 Performance Of The HgCdTe Detector For MOSFIRE, An Imager And Multi-Object Spectrometer For Keck Observatory . . . 69
3.1 Introduction . . . 69
3.2 MOSFIRE Design . . . 70
3.3 The MOSFIRE Detector . . . 72
3.4 Lab Results . . . 75
3.4.1 32-Channel Readout . . . 76
3.4.2 Optimizing The Detector Settings . . . 77
3.4.3 Detector Systems . . . 79
3.4.4 Read Noise And Dark Current . . . 80
3.4.5 Gain Setting And Linearity . . . 84

3.4.6 Bias Drifts . . . 86
3.4.7 Persistence . . . 88
3.5 On-Sky Results . . . 90
3.5.1 Read Noise . . . 90
3.5.2 Science Verification . . . 91
3.6 Summary . . . 93
4 The Mass-Metallicity Relation Of A $z \sim 2$ Protocluster With MOSFIRE . . . 96
4.1 Introduction . . . 96
4.2 Sample . . . 101
4.3 Observations And Data Reduction . . . 103
4.3.1 Broadband Ancillary Photometry . . . 103
4.3.2 MOSFIRE Spectroscopy . . . 105
4.4 Physical Properties . . . 112
4.4.1 Stellar Masses . . . 112
4.4.2 Metallicities . . . 116
4.5 Mass-Metallcity Relation . . . 118
4.6 Discussion . . . 124
4.7 Summary And Conclusions . . . 126
5 Future Work . . . 128
5.1 Project I Future Work . . . 128
5.2 Project III Future Work . . . 129

5.2.1 Velocity Dispersion 130
5.2.2 Star-Formation Rates 131
5.2.3 Fundamental Metallicity Relation 134
5.2.4 The BPT Diagram 134

6 Conclusion 140

6.1 Constraining Galaxy Formation Models With Multiple-Peaked Lyα Emission Profiles 140
6.2 Advanced Astronomical Instrumentation With MOSFIRE 143
6.3 Examination Of A High-Redshift Protocluster 144
6.4 Concluding Remarks 146

List of Figures

1.1 Atmospheric Transmission In The Near-Infrared Wavelength Regime 3

1.2 Galaxy Selection With Photometric Drop-Out Technique 4

2.1 $\mathcal{R}$-Band Images For The Sample Of 18 Objects 20

2.2 2D LRIS AND NIRSPEC Spectra For Spatially-Extended Objects 26

2.3 Lyα Velocity Profiles For The 18 Objects In Sample 31

2.4 2D Lyα Spectra Representing The 5 Groups 35

2.5 Location Of Velocity Offsets For Peak, Trough, And Absorption Lines 37

2.6 Histogram Of Distribution Of Peak-To-Peak Velocity Separation . 38

2.7 Histogram Of Velocity Dispersion 40

2.8 E(B-V) Comparison Calculated With Two Different Methods . . . 43

2.9 Example Interstellar Absorption Velocity Profile 47

2.10 Histogram Of Interstellar Absorption Line Widths 48

2.11 Comparison Of Velocity Profiles Of Multiple-Peaked And Single-Peaked Composites 51

2.12 Models Of Lyα Profiles From Expanding Shell 55

2.13 Comparison Of Models To Data 57

3.1 Design Layout Of MOSFIRE Instrument 71

3.2 Image Of Detector And Readout Electronics 75

3.3 Reference Pixel Subtraction 77

3.4 Single-Ended Versus Differential Preamp Input Mode 79

3.5 Illustration Of Multiple-Correlated Double Sample Readout Scheme 81
3.6 Read Noise With SIDECAR ASIC Readout Electronics 83
3.7 Variance Method For Calculating Detector Gain 86
3.8 Global Linearity Of Detector 87
3.9 Bias Drifts In Detector 88
3.10 Persistence Characteristics Of MOSFIRE Detector 89
3.11 Read Noise At The Telescope 91
3.12 Commissioning Image Of The Antennae Galaxy 93
3.13 MOSFIRE Team During Commissioning 95

4.1 Histogram Of BX/MD Galaxies In The HS1700 Field 98
4.2 Image Of MOSFIRE Masks Used For Observations 102
4.3 Histogram Comparison Of Stellar Masses 104
4.4 Histogram Comparison Of K_s-band Magnitudes 105
4.5 Example MOSFIRE 2D And 1D Spectrum 107
4.6 Stellar Mass Estimate Comparison 114
4.7 Example SED Fit To Broadband Photometry To Estimate Stellar Mass 115
4.8 Mass-Metallicity Relation For Individual Protocluster and Field Galaxies 120
4.9 Composite Spectra Binned By Stellar Mass For Protocluster And Field Galaxies 122
4.10 Mass-Metallicity Relation Utilizing Composite Spectra Of Protocluster And Field Galaxies 123

5.1 Velocity Dispersion Analysis For Protocluster And Field Galaxies 132
5.2 SFR Analysis For Protocluster And Field Galaxies 133
5.3 sSFR And The FMR 135
5.4 BPT Diagram For $z \sim 2$ Star-Forming Galaxies 139

List of Tables

2.1 Observation Log With Keck II NIRSPEC 22

2.1 Observation Log With Keck II NIRSPEC 23

2.2 NIRSPEC Measurement Results 30

2.3 Velocity Measurements: Lyα Emission And Interstellar Absorption 32

2.3 Velocity Measurements: Lyα Emission And Interstellar Absorption 33

2.4 Physical Quantities 45

3.1 Read Noise Measurements 82

3.2 Read Noise Measurements At Keck Observatory 92

4.1 Physical Properties In The HS1700 Field 108

4.1 Physical Properties In The HS1700 Field 109

4.1 Physical Properties In The HS1700 Field 110

4.1 Physical Properties In The HS1700 Field 111

Acknowledgments

There are many people who contributed to my accomplishment of obtaining a Ph.D that I would like to thank. From an early age there have always been teachers that encouraged me to work hard to achieve my goals. Specifically, I would like to acknowledge my introductory physics college teacher, Professor Don Harris, who teaches with a passion and a love for physics that undeniably influenced my future career path.

As a competitive tennis player, my coaches have taught me discipline and sacrifice are important to attain your goals. I would like to acknowledge Jenn Isaac, my high school tennis coach, and Steve Dunmore, my college tennis coach, for their time and effort in instructing me how to succeed with determination and persistence.

I am fortunate to have friends that have supported me through good times and bad during my life. I will be forever grateful to my best friend, Monica Lynn, for her unwavering friendship and encouragement. I would like to thank my friend Christena Wong for always telling me it is alright to make mistakes. I would like to thank Ian Crossfield and Betsy Mills, my partners in crime during graduate school classes, for all the fun experiences. I would like to acknowledge Kathy Kornei for being such a thoughtful listener. I would like to thank Kevin Hainline for all the stimulating conversion while sitting on a mountain top and for taking it in stride when I cut him out of photographs. I wish to especially thank Gregory Mace for helping me keep my sanity during the many long days (and nights) of MOSFIRE testing.

A research advisor strongly influences a person's success in graduate school and their research career. I was very fortunate to have not one, but two, incredibly supportive and dedicated advisors, Dr. Ian McLean and Dr. Alice Shapley. Ian taught me how to become an astronomical instrumentalist, giving me the confidence needed to thrive in a laboratory setting, while educating me on how to successfully lead and manage a team. His patience and guidance during my graduate career has been invaluable. Alice has taught me what it means to be an exceptional researcher, to strive for the best and to push the boundaries further on what I can accomplish. Her enthusiasm and guidance was an integral part of my success in graduate school. I would like to acknowledge that this work would not have been possible without the constant support, and friendship, of both Ian and Alice.

I would like to thank my parents, Cynthia and Calvin, for their eternal love and encouragement. They never thought it was strange that their daughter wanted to be a physicist and without their support I would never have made it to where I am today. I wish to acknowledge my younger brother Jared for being true to himself. I would like to thank my Grandmother Marian for being there during every major accomplishment in my life. I would also like to dedicate this thesis to my Grandmother Anne, who is no longer with us, but I know she would have been so incredibly proud of me.

I will be forever grateful that I found my "alpha monkey" during graduate school at UCLA. My husband Gabriel is my biggest supporter in both my academic career and in all my other endeavors. His unwavering encouragement through graduate school helped me to stay focused and he was always there to hold me up even when all I wanted to do was fall down. I consider myself blessed to be with such a wonderful, caring man who supports me unconditionally.

Chapter 2 of this thesis is a version of Kulas et al. (2012b) and is reproduced by permission of the AAS. I would like to thank my collaborators on this work: Alice Shapley, Juna Kollmeier, Zheng Zheng, Charles Steidel, and Kevin Hainline.

Chapter 3 of this thesis is a version of Kulas et al. (2012a) and is reproduced by permission of the SPIE. I would like to acknowledge my collaborators on this research: Ian McLean and Charles Steidel. I would also like to thank the entire MOSFIRE team for all their hard work that made this project possible.

Chapter 4 is a version of a paper to be submitted to the Astrophysical Journal Letters. I would like to thank my collaborators on this work: Ian McLean, Alice Shapley, Charles Steidel, Nicholas Konidaris, Gregory Mace, Gwen Rudie, Ryan Trainor, Naveen Reddy, and Keith Matthews.

The data contained in this thesis were obtained at the W.M. Keck Observatories on Mauna Kea, Hawaii. I wish to acknowledge those of Hawaiian ancestry on whose sacred mountain we astronomers are privileged to be guests. Without their generous hospitality, the observations presented herein would not have been possible. I would also like to thank the many support telescope operators and staff scientists at the Keck Observatory who were always there to help with the inevitable "fatal" crash at 2am in the morning.

Vita

2003	A.S. Physics; A.S. Natural Science; A.A. Liberal Arts Sierra College
2004-2006	Teaching Assistant for Introductory Physics University of California, San Diego
2006	B.S. Physics with a specialization in Astrophysics Minor in Mathematics University of California, San Diego
2007-2010	Teaching Assistant for Introductory Astronomy University of California, Los Angeles
2008	Teaching Assistant Coordinator University of California, Los Angeles
2008-2009	Center for Adaptive Optics ISEE Program (Formerly PDP) Co-Teacher for Summer Session Introductory Astronomy University of California, Santa Cruz
2009	M.S. Astronomy University of California, Los Angeles
2011	Bruin Hero Award *Astronomy Live!* Founder and Coordinator
2012-2013	Graduate Division Dissertation Year Fellowship
2012-2013	Abelmann-Rudnick Scholarship
2013	NASA Postdoctoral Program Fellowship

Publications

Kulas, K. R.; McLean, I. S.; Shapley, A. E.; Steidel, C. C.; *A Detailed Study of Galaxies in High-Redshift Protoclusters*, 2013, 221^{st} AAS Conference Proceedings

Kulas, K. R.; Shapley, A. E.; Kollmeier, J. A.; Zheng, Z.; Steidel, C. C.; Hainline, K. N.; *The Kinematics Of Multiple-Peaked Lyman α Emission In Star-forming Galaxies At $z \sim 2-3$*, 2012, ApJ, 745, 33

Kulas, K. R.; McLean, I. S.; Steidel, C. C.; *Performance of the HgCdTe Detector for MOSFIRE, an Imager and Multi-Object Spectrometer for Keck Observatory*, 2012, Proceedings of SPIE, 8453-63

McLean, I.; Steidel, C.; Epps, H.; Konidaris, N.; Matthews, K.; Adkins, S.; Aliado, T.; Brims, G.; Canfield, J.; Cromer, J.; Fucik, J.; **Kulas, K. R.**; Mace, G.; Magnone, K; Rodriguez, H.; Rudie, G.; Trainor, R.; Wang, E.; Weber, B.; Weiss, J.; *MOSFIRE, the Multi-Object Spectrometer For Infra-Red Exploration at the Keck Observatory*; 2012, Proceedings of SPIE, 8446-17

Montgomery, R.; **Kulas, K. R.**; *The Design and Implementation of the Galaxy Component Inquiry*, 2010, Astronomical Society of the Pacific, 436, 120

McLean, I.S.; Steidel, C.; Epps, H.; Matthews, K.; Adkins, S.; Konidaris, N.; Weber, B.; Aliado, T.; Brims G.; Canfield, J.; Cromer, J.; Fucik, J.; **Kulas, K. R.**; Mace, G.; Magnone, K; Rodriguez, H.; Wang, E.; and Weiss, J.; *Design and Development of MOSFIRE: the Multi-Object Spectrometer for Infrared Exploration at the Keck Observatory*, 2010, Proceedings of the SPIE, 7735, 77351E

Kulas, K. R.; Shapley, A. E..; Hainline, K. N.;*The Kinematics Of Multiple-peaked Lyman α Emission In Star-forming Galaxies At $z \sim 2-3$*, 2010, 216^{th} AAS Conference Proceedings

Kulas, K. R.; McLean, I. S.; *Evaluation Of The ASIC-Controlled H2-RG Science-Grade Detector For MOSFIRE*, 2010, 215^{th} AAS Conference Proceedings

Kulas, K. R.; McLean, I. S.; *Evaluation Of The ASIC-Controlled H2-RG Detector For MOSFIRE*, 2009, 213^{th} AAS Conference Proceedings

CHAPTER 1

Introduction

An important goal in the study of our universe is to understand how galaxies form and evolve. The cosmic epoch approximately 2-3 Gigayears after the Big Bang, characterized by the spectroscopic redshift parameter $z \sim 2-3$, is an active period for galaxies in the universe, with the global star-formation rate density at its peak (Madau et al. 1996; Reddy et al. 2008; Bouwens et al. 2009). During this epoch many internal and external processes, such as large-scale outflows from star formation or active galactic nuclei (AGN) activity, accretion from cold gas, and mergers, can alter the properties (e.g., structure, metallicity, star-formation rate, velocity dispersion) and evolution of galaxies. This high level of activity makes the study of objects during $z \sim 2-3$ ideal for understanding what processes are important and how gas supplies are regulated during the formation of galaxies.

Many of these processes can ideally be studied with rest-frame optical emission lines, such as Hα (the n = 3 to n = 2 electron transition for hydrogen at $\lambda = 6563$ Å), Hβ (the n = 4 to n = 2 electron transition for hydrogen at $\lambda = 4861$ Å), and the forbidden transitions of singly ionized nitrogen [N II]λ6584 and doubly ionized oxygen [O III]λ5007. By the time the light from distant galaxies reaches Earth, these emission lines are shifted into the near-infrared by the expansion of the universe and the apparent brightness has become extremely faint. Consequently, near-infrared spectroscopy on a large telescope plays an integral role in the study of high-redshift galaxies.

There exist certain wavelength regimes in the near-infrared ($0.9 - 2.5$ μm) where absorption due to water vapor (H_2O) and carbon dioxide (CO_2) in the Earth's atmosphere efficiently restricts any transmission. Fortunately, there are windows of atmospheric transparency, especially at high elevation and in arid locations on Earth like Mauna Kea, Hawaii. The passbands that astronomers use in the near-infrared correspond to these atmospheric windows; designated as the J, H, and K bands (see Figure 1.1). These windows of transmission allow for observations of the important rest-frame optical emission lines of high-redshift galaxies. Even though these windows exist, astronomers still require innovative near-infrared instrumentation in order to study such faint and distant objects.

Before the advent of the 10-meter class telescopes and the Hubble Space Telescope, there was a limited number of galaxies identified beyond $z \sim 1$. Once these facilities came online, though, numerous $z \sim 2-3$ galaxies were discovered using the optical U, G, and $\mathcal{R}$ bands, which are respectively centered at 3550 Å, 4780 Å, and 6830 Å. The $z \sim 3$ objects are typically selected using the photometric drop-out technique that utilizes the Lyman limit (Steidel et al. 1996). The Lyman limit occurs at wavelengths below 912 Å, where photons will be completely, or almost completely, absorbed by the neutral gas surrounding the star-forming regions in the galaxy. For high-redshift galaxies, the Lyman limit will shift in wavelength by a factor of $1+z$. For $z \sim 3$ objects, photons emitted at 912 Å will shift into the optical wavelength regime of the U band. A galaxy at this redshift will "drop out" of a $U-$band image while still being detected in the G and $\mathcal{R}$ bands at longer wavelengths (see top panel of Figure 1.2). These galaxies are typically called Lyman Break Galaxies (LBGs). This drop-out technique cannot be used for galaxies at $z \sim 2$ since the Lyman limit will shift out of the U band at this redshift (see bottom panel of Figure 1.2). However, objects at $z \sim 2$ can be color selected using the $UG\mathcal{R}$ bands to have similar UV luminosity and dust

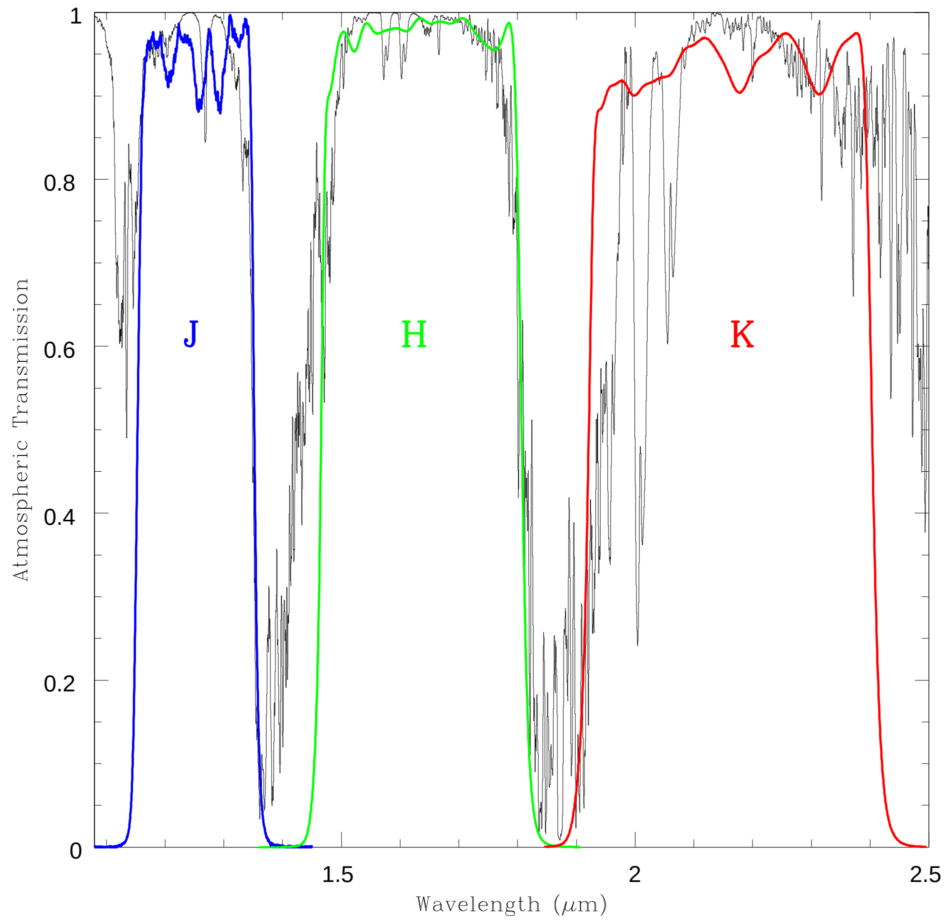

Figure 1.1 Atmospheric transmission for the near-infrared wavelength regime from $0.9-2.5$ μm. The MOSFIRE J-, H-, and K-band filters are overlaid.

extinction as LBGs (Steidel et al. 2004). Today there are thousands of known $z\sim 2-3$ UV-selected star-forming galaxies, thus enabling detailed statistical studies into how galaxies form and evolve

For my thesis research I have examined the physical processes relevant during the formation of galaxies over the epoch of $z\sim 2-3$ using several different approaches, all of which utilized near-infrared spectroscopy. The major goals of this thesis are 1) constraining the physical properties (i.e., mass, column density)

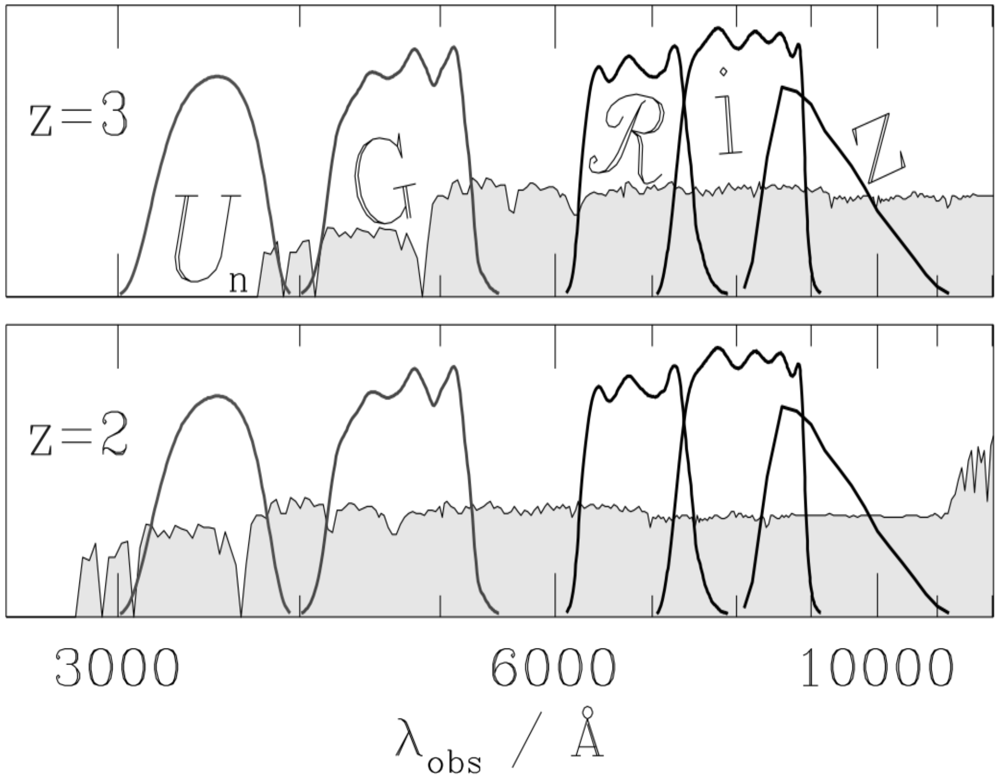

Figure 1.2 Galaxies at $z \sim 3$ can be selected from the $UG\mathcal{R}$ photometric data by applying a drop-out technique that utilizes the Lyman limit. The Lyman limit will shift into the U band for $z \sim 3$ objects, which are typically called Lyman Break Galaxies (LBGs), causing LBGs to drop-out of the U-band images while still being detected in the G- and $\mathcal{R}$-bands (top panel). This drop-out technique cannot be used to select objects at $z \sim 2$ since the Lyman limit lis located blueward of the U band at this redshift (bottom panel). However, color selection techniques using $U - G$ and $G - \mathcal{R}$ can single out $z \sim 2$ galaxies with similar UV luminosity and dust extinction as LBGs. (Figure modified from Adelberger et al. 2004)

of the large-scale outflows that appear to be ubiquitous in $z \sim 2-3$ star-forming galaxies and 2) understanding how environment (i.e., clustering) affects the formation processes of galaxies, which in turn will place observational constraints on galaxy formation models. To complete this study, I have also worked to bring to realization the highly sensitive near-infrared instrument, MOSFIRE (Multi-

Object Spectrometer for Infrared Exploration), whose multiplexing capability enables the observation of a large number of high-redshift galaxies simultaneously. My thesis research is divided into three projects that are outlined below.

1.1 Project I: The Kinematics Of Multiple-Peaked Lyα Emission In Star-Forming Galaxies At $z \sim 2-3$

The process described as "feedback," which refers to large-scale outflows of mass, metals, energy, and momentum from galaxies, is considered a crucial component in models of galaxy formation. The evidence for feedback in high-redshift star-forming galaxies comes in numerous forms such as redshifted Lyα emission and blueshifted interstellar absorption lines (Pettini et al. 2001; Shapley et al. 2005a; Steidel et al. 2010). Yet despite the evidence for ubiquitous outflows in the high-redshift universe, estimates of fundamental physical quantities such as gas column densities and mass outflow rates in these superwinds have remained elusive. Additionally, hydrodynamical cosmological simulations suggest that, at these same redshifts, there should be large amounts of infalling gas, fueling the large star-formation rates (e.g., Dekel et al. 2009). Observationally, the presence of accreting gas has remained a challenge to confirm.

The outflowing and infalling gas is composed predominately of hydrogen, which is the most abundant element in the universe. The Lyα photon, which is emitted at 1216 Å when the electron of a hydrogen atom transitions from the n = 2 to the n = 1 state, is one of the most widely used features of star formation in both the nearby and very distant universe. An important goal in the study of high-redshift galaxies is to characterize the factors modulating the escape of Lyα photons from star-forming galaxies. Understanding in greater depth how Lyα

photons escape will lend insight into the structure of the interstellar medium (ISM) and the properties of large-scale outflows, which represent critical inputs into models of galaxy formation.

However, Lyα can be subject to complex radiative transfer effects. The photons experience resonant scattering (Neufeld 1990) in addition to being influenced by the velocity and density fields of the ISM (Verhamme et al. 2008). In principle, the structure of the Lyα line encodes the velocity field and density distribution of the gas through which it has emerged. The case of multiple-peaked Lyα profiles, seen in a fraction of star-forming $z \sim 2-3$ galaxies, offers a particularly detailed look into Lyα escape due to the rich structure of the resultant line.

The first component of my thesis, *Project I*, is designed to clarify the underlying process for this multiple-peaked structure. Despite recent advances in modeling of the escape of Lyα photons from star-forming galaxies at $z \sim 2-3$ (Verhamme et al. 2008), the comparisons between models and data are often missing crucial observational information. In particular, accurate systemic redshift measurements, intrinsic nebular line-widths, and intrinsic ionizing photon fluxes are all necessary when making a meaningful comparison between models and data. These measurements can be obtained with observations of Hα ($z \sim 2$) and [O III]λ5007 ($z \sim 3$), which have shifted to near-infrared wavelengths by $z \sim 2$. I used NIRSPEC, a single-object near-infrared instrument at Keck Observatory (McLean et al. 1998), to observe Hα or [O III]λ5007 for a total of 18 UV-selected star-forming galaxies with multiple-peaked Lyα emission. With these data, I have placed detailed constraints on Lyα radiative transfer models for outflowing gas. In addition, a small subset of this sample appears to show signatures of infalling gas, which can lead to important constraints on galaxy formation models. Future work will include the creation of accurate Lyα radiative transfer models for these systems, thus allowing a detailed understanding of the fundamental physical properties of outflowing and infalling gas for star-forming galaxies at $z \sim 2-3$. This work has been published in the Astrophysical Journal (Kulas et al. 2012b).

1.2 Project II: Performance Of The HgCdTe Detector For MOSFIRE, An Imager And Multi-Object Spectrometer For Keck Observatory

Near-infrared instrumentation has only become readily available to astronomers within the last several decades due to the advancement of infrared arrays. During the period of 1974−1984 infrared devices began to be researched and constructed, but they were mostly used for military applications. In the early 1980s, small format devices did exist (e.g., 2×16 pixels), but they contained high noise levels which were not ideal for low-background applications that astronomers required. During this time several astronomers and engineers, such as Al Fowler, Judith Pipher, and Ian McLean, pioneered the development of infrared technology that would be suitable for the needs of the astronomical community. By 1987, the first astronomical results from infrared arrays on ground-based telescopes started to be announced (for a detailed historical background see McLean 2008). Since then, the advancement of infrared detectors has grown exponentially. Numerous instruments have now been developed with infrared capabilities for both ground- and space-based telescopes. In addition, advancing infrared technology is still an active area of research. Modern infrared instrumentation allows for the study of the early universe in a manner that was not conceivable only twenty years ago.

Instrumentation plays a vital role in obtaining the best possible data for answering the questions motivated in my thesis. A spectrograph instrument that operates in the near-infrared is ideal for studying the numerous important rest-frame optical emission lines such as Hα and [O III]λ5007 at $z \sim 2-3$. *Project II* of my thesis describes the instrumentation work I have completed on the Multi-Object Spectrometer for InfraRed Exploration (MOSFIRE), which is located at the Cassegrain focus on the Keck I 10-meter telescope. MOSFIRE utilizes the new Hawaii-2RG (H2RG) detector from Teledyne Imaging Sensors. The H2RG detector contains a total of 2048 $\times$ 2048 pixels and is made from mercury cadmium telluride (HgCdTe) with a 2.5 μm cut off. I have focused my research on the characterization of the H2RG detector and the detector system for MOSFIRE. To detect the faint emission and absorption lines from high-redshift galaxies, it is important for the noise of the detector itself to be as low as possible.

The H2RG detectors have been measured at Teledyne to have unprecedented read noise values of < 5 e$^-$ (compared to previous generations of infrared detectors which had noise levels around $\sim$25 e$^-$). Teledyne, though, used standard controllers to read out the detector's signal, while MOSFIRE will use the newly developed SIDECAR ASIC (System for Image Digitization Enhancement Control And Retrieval Application Specific Integrated Circuit). *Project II* of my thesis has focused on verifying the correct operation of the ASIC and obtaining a read noise value of ~ 5 e$^-$ for the MOSFIRE detector inside of the deliverable instrument. This noise level will allow MOSFIRE to reach its desired sensitivity limits. In addition, my instrumentation work has encompassed numerous tests to measure the dark current, linearity, gain, and persistence of the MOSFIRE detector. This work has been described in the SPIE Astronomical Telescopes and Instrumentation conference proceedings (Kulas et al. 2012a).

1.3 Project III: A Detailed Study Of Galaxies In A High-Redshift Protocluster With MOSFIRE

MOSFIRE was delivered during the Spring of 2012 to the Keck Observatory. Once installed, MOSFIRE demonstrated the ability to perform groundbreaking extragalactic science. High-redshift galaxies are very faint and therefore require long integration times to obtain an adequate signal-to-noise ratio. The study of high-redshift star-forming galaxies within and around over-dense regions of galaxies is ideally suited for MOSFIRE's capability to observe numerous galaxies simultaneously over a large field of view, thus enabling statistical significant samples sizes to be obtained in a moderate amount of observing time.

Galaxy properties have been demonstrated to be associated with environment in the local universe (e.g., Hogg et al. 2004; Kauffmann et al. 2004; Clemens et al. 2006; van der Wel et al. 2010; Wetzel et al. 2012). Galaxies found in the central, densest regions of clusters at $z < 1$ are typically early-type galaxies with low star-formation rates (SFRs), while more active, late-type galaxies are preferentially located in the sparser edges of the cluster field. From these observations, it is apparent that environment plays a key role in the evolution of galaxies.

Detailed cluster studies have been done out to $z \sim 1$ (e.g., Holden et al. 2009; Patel et al. 2009), but there is limited information for clusters at $z > 1$ (but see e.g., Papovich et al. 2012). Protoclusters at $z > 2$ are still in the process of forming and have not yet virialized, making them ideal for examining the origin of the environmental trends observed locally. Measuring the physical properties (e.g., stellar mass, metallicity, velocity dispersion) of protocluster galaxies will facilitate a better understanding of the processes that are relevant in dense environments and the formation times of cluster versus field galaxies, where field galaxies are defined as an object not residing within an overdense region.

For *Project III* of my thesis I used MOSFIRE to study a protocluster at redshift $z \sim 2$ in the HS1700+643 field ($\alpha = 17:01:01$, $\delta = +64:11:58$). The HS1700 protocluster was discovered during the course of a spectroscopic survey with a well-defined redshift selection function, enabling a robust evaluation of the galaxy overdensity. This selection is unlike most protoclusters, which have been discovered around radio galaxies using narrow-band (NB) imaging tuned to find Lyman Alpha Emitters (LAEs) (e.g., Venemans et al. 2007). The HS1700 field has extensive multi-wavelength data available, but lacks comprehensive near-IR spectroscopy, which contains the important diagnostic rest-frame optical emission lines. Acquiring JHK spectroscopic data with MOSFIRE will allow for the measurements of numerous physical properties that probe the star-forming regions of the target galaxies. In addition, the ancillary multi-wavelength data for HS1700 can be used for spectral energy distribution (SED) modeling to estimate physical properties such as stellar mass and to examine galaxy morphologies with respect to the measured physical properties.

Using MOSFIRE K-band spectroscopy, I have analyzed the Hα and [N II]λ6584 emission lines of galaxies within and around the $z = 2.3$ protocluster in the HS1700 field, which allows for the measurement of the gas-phase metallicity based on the $N2 \equiv \log([\text{N II}]\lambda6584/\text{H}\alpha)$ strong-line indicator. The main sample consists of 23 protocluster and 20 field galaxies with estimates of stellar mass and gas-phase oxygen abundance. With these data I have examined the mass-metallicity relation (MZR) with respect to environment at $z \sim 2$. From the MZR I determined that environment does affect how gas supplies are regulated in high-redshift galaxies, with lower mass protocluster galaxies demonstrating an enhanced metallicity compared to field galaxies at the same stellar mass. The combination of MOSFIRE near-IR spectroscopy and existing multi-wavelength photometric data has enabled the examination of physical processes that are responsible for how gas supplies are regulated during the formation of galaxies in extreme environments. A paper describing this work has been submitted to the Astrophysical Journal.

In addition to the measurement of Hα and [N II] for galaxies in the HS1700 field, I have detected the emission lines [O II], [O III], Hβ,and [S II] from the MOSFIRE JHK spectroscopic data. Prospective work with this data set will include the examination of numerous other physical properties for the protocluster and field galaxies, such as velocity dispersion, SFR, electron density, electron temperature, and ionization parameter for the local ionization state. Furthermore, I have obtained MOSFIRE HK spectroscopy of galaxies in the SSA22a field, which contains a protocluster at $z = 3.09$. I will measure the [O II], [O III], and Hβ emission lines from the HK spectroscopic data for protocluster and field galaxies in SSA22a. Analysis of the SSA22a protocluster will increase the understanding of galaxy formation to an earlier epoch and will enable a detailed investigation of possible evolutionary trends between $z \sim 3$ and $z \sim 2$ in overdense environments.

CHAPTER 2

The Kinematics Of Multiple-Peaked Lyα Emission In Star-Forming Galaxies At $z \sim 2-3$

2.1 Introduction

The process described as "feedback" is considered a crucial component in models of galaxy formation. Feedback commonly refers to large-scale outflows of mass, metals, energy, and momentum from galaxies, which therefore regulate the amount of gas available to form stars, as well as the thermodynamics and chemical enrichment of the surrounding intergalactic medium (IGM). The evidence for feedback in high-redshift star-forming galaxies comes in several forms, including blueshifts of hundreds of km s^{-1} in interstellar absorption lines relative to galaxy systemic redshifts (Pettini et al. 2001; Shapley et al. 2003; Steidel et al. 2010), and the nature of the IGM environments of vigorously star-forming galaxies, in terms of the optical depth and kinematics of the surrounding H I and heavy elements (Adelberger et al. 2003, 2005). Yet, in spite of evidence for ubiquitous outflows at high redshift, estimates of fundamental physical quantities such as gas column densities and mass outflow rates in the superwinds have remained elusive. While there is much observational evidence for outflows in high-redshift galaxies, both analytic models and hydrodynamical simulations of these systems suggest that, at the same cosmic epochs, they should be rapidly accreting cold gas from the

IGM, fueling their active rates of star formation (Birnboim & Dekel 2003; Kereš et al. 2005, 2009; Dekel et al. 2009). Searching for observational signatures of the process of cold gas accretion at high redshift remains an open challenge.

The Lyα feature is one of the most widely used probes of star formation in both the nearby and very distant universe. While Lyα photons are initially produced by recombining ionized gas in H II regions, resonant scattering through the interstellar medium (ISM) of galaxies can lead to extreme modulation of the intrinsic emission profile, in both frequency and spatial location. Absorption by dust can completely suppress Lyα emission, producing a strong absorption profile, even in galaxies with high rates of star formation. It is therefore difficult to determine the intrinsic properties of the gas giving rise to Lyα emission from the observed profile alone. Only recently has it become possible to make detailed theoretical predictions for the Lyα profiles emergent from complex systems similar to those observed at high redshift (Ahn et al. 2002; Zheng & Miralda-Escudé 2002; Hansen & Oh 2006; Verhamme et al. 2006, 2008; Dijkstra & Kramer 2012). These new calculations (e.g., Verhamme et al. 2006) typically employ a Monte Carlo approach to propagate a representative ensemble of Lyα photons through gas and dust of arbitrary spatial and velocity distribution outputting Lyα profiles as would be observed. By comparison with Lyα profiles in actual galaxy spectra, it is possible, in principle, to recover quantities such as the expansion/infall velocity of the outflow/inflow, the column density and velocity dispersion of absorbing gas, and the gas covering fraction. Therefore, modeling of observed Lyα emission profiles represents an independent method of probing the processes of feedback and accretion at high redshift.

The majority of Lyα emission profiles at high redshift fall in the category of single-peaked and asymmetric (Shapley et al. 2003; Tapken et al. 2007), which is a natural outcome of an expanding medium (Verhamme et al. 2008). However, multiple-peaked Lyα profiles, seen in a fraction of star-forming UV-selected galaxies at $z \sim 2-3$, offer a particularly detailed perspective on Lyα escape due to the rich structure of the emergent line. In principle, the structure of the Lyα line encodes the velocity field and density distribution of the gas through which it has emerged. For example, a symmetric double-peaked profile centered on the velocity-field zeropoint is a natural outcome of the radiative transfer of Lyα photons through a static medium (Osterbrock 1962). Recent advances in modeling the escape of the Lyα photons from star-forming galaxies at $z \sim 2-3$ have isolated several features of the Lyα profile that may be expected for specific gas geometries and velocity fields (e.g. Verhamme et al. 2006; Laursen et al. 2009a,b; Barnes et al. 2011; Dijkstra & Kramer 2012). Since Lyα is the most readily observed high-redshift emission line, there is enormous potential to better understand the structure of the early galaxies by interpreting Lyα line profiles.

Previous attempts to compare observed Lyα line morphologies to theoretical predictions have been missing crucial information, weakening the derived constraints on galaxy outflow and inflow properties. In particular, accurate systemic redshift measurements, nebular line widths, and intrinsic ionizing photon fluxes have been absent from most previous comparisons (but see, e.g., Yang et al. 2011; McLinden et al. 2011). These three observables are critical for anchoring the velocity scale of the models, constraining the mass and thermal motions of the gas, and determining the overall normalization for a given model. To provide the critical missing constraints on the observed kinematics of star-forming galaxies at $z \sim 2-3$ with multiple-peaked Lyα emission I have used results obtained from Hα and [O III]λ5007 emission lines. In addition, I have utilized the large database of Lyα emission lines in high-redshift objects to determine the *frequency* of the multiple-peaked systems, providing a global perspective on the potential of using Lyα morphology to reveal $z \sim 2-3$ gaseous structure.

The method used to select targets from the parent sample of UV-selected galaxies at $z \sim 2-3$ is explained in Section 2.2, while the observations and data reduction are described in Section 2.3. The Lyα velocity profiles are presented in Section 2.4 with precise velocity-field zeropoints determined from the Hα (or [O III]λ5007) measurements. In Section 2.5 the measured physical quantities for each system are reported. Section 2.6 describes current Lyα radiative transfer models, in addition to a qualitative comparison between some simple models and the measured Lyα velocity profiles. Finally, in Section 2.7 I summarize the results and discuss how the measurements will be used in future work to accurately model the processes that give rise to the multiple-peaked Lyα profiles from star-forming galaxies at $z \sim 2-3$. A flat ΛCDM cosmology with $\Omega_m = 0.3$, $\Omega_\Lambda = 0.7$, and $H_o = 70$ km s^{-1} Mpc^{-1} is assumed throughout this chapter.

2.2 Sample Selection

Target galaxies were drawn from the UV-selected sample described in Steidel et al. (2003, 2004). These UV-selected surveys have yielded over 3,000 spectroscopically confirmed star-forming galaxies at $z \sim 1.5-3.5$. The majority of the spectra cover the HI Lyα feature at 1216 Å. The observed Lyα profiles for UV-selected star-forming galaxies vary widely in strength, from damped absorption to strong emission. Of the ∼1500 objects that show net emission, a fraction exhibit a multiple-peaked profile. While this phenomenon has been previously reported (Tapken et al. 2007; Quider et al. 2009) its frequency of occurrence has never been systematically analyzed. I have used the database of star-forming galaxies to assess the frequency of multiple-peaked Lyα profiles in $z \sim 2-3$ galaxies in order to determine whether such profiles represent rare outliers or are commonplace features of the galaxy population.

To identify the frequency of multiple-peaked profiles, I first separated the full spectroscopic sample into subsets of galaxies with and without detectable Lyα emission. The $\sim$1500 galaxies with Lyα emission were then considered for further study. All of the optical (rest-frame UV) spectra were obtained using the LRIS spectrograph on the Keck I telescope (Oke et al. 1995). These spectra were taken with the 300 line mm^{-1} grating blazed at 5000 Å, or, following the LRIS-B upgrade (Steidel et al. 2004), with the 400 line mm^{-1} or 600 line mm^{-1} grism blazed at 3400 Å, and 4000 Å, respectively. The resolution of the spectra (taken through $1.''2$ slits) establishes a lower limit in velocity space on the separation of multiple peaks that can be identified. From this sample I was able to identify objects that have a minimum peak separation of 225 [370, 500] km s^{-1} for the 600 [400,300]-line grism/grating. The spectra were first separated by grism/grating and then analyzed by each resolution group individually. Approximately 60% of the spectra were obtained with the 400- and 600-line grisms, while the rest of the spectra were taken using the 300-line grating.

I programmed a systematic algorithm to search for multiple peaks within the Lyα profile. Several criteria were used to minimize contamination from noisy spectra which can yield a false indication of multiple peaks due to noise spikes. The first criterion was a signal-to-noise (S/N) lower limit of 3 on the strongest flux peak height, which was implemented to establish a consistent threshold for characterizing Lyα profiles. This criterion reduced the sample to $\sim$1000 spectra with 163, 527, and 402 spectra, respectively, from the 600- and 400-line grism, and 300-line grating. The spectra were then separated into resolution groups and the algorithm was implemented independently on each sub-sample. First, the algorithm searched between 1210 and 1225 Å in each spectrum for the maximum flux value, given that this wavelength range typically contains the observed Lyα peak in the spectra of star-forming galaxies. This maximum was identified as the primary Lyα emission peak. The continuum level was then estimated for the blue and red side separately from the mean of the flux over a $\sim$100 Å span blueward and redward of 1210 and 1225 Å, respectively. Starting from the primary peak's maximum flux point, the program stepped down towards the blue side until reaching the continuum level. If a local minimum was noted before reaching the continuum the program marked the local maximum after that minimum as another possible peak for the Lyα line. Another criterion used to avoid noise spikes was for the secondary maximum to span at least two adjacent steps in wavelength. This procedure was then repeated on the red side of the primary peak. If an additional peak was noted by the algorithm, I required the flux ratio of the additional peak to the primary peak to be greater than $\frac{1}{N}$, with N being the S/N of the primary peak. This value was chosen in order to reject any small noise spikes in the identification of the additional peak. My sample is therefore complete for primary to secondary ratios less than or equal to 3. At higher primary-peak S/N ratio I can also probe larger ratios of primary-to-secondary peak heights. In practice, however, the typical primary-to-secondary peak ratio is ~ 3. In addition to analyzing the full sample of spectra with this objective criteria, I examined the spectra by eye for any objects that might have been missed by the algorithm described above. The additional multiple-peaked objects found by eye comprise a small percentage of the total sample, roughly $\sim 15\%$.

For the 300-line grating, the percentage of spectra with multiple-peaked Lyα emission identified is 23% (92 spectra). For the 600- and 400-line grisms the values are, respectively, 27% (44 spectra) and 20% (103 spectra). In addition to the main spectroscopic sample, a set of 121 objects was followed up with

400-line grism spectra using significantly longer exposure times ($7 - 13$ hours as opposed to 1.5 hours), with correspondingly higher S/N (Bogosavljevic 2010, Ph.D Thesis). In this sample, 97 objects show Lyα emission, and 33% (32 spectra) of the emitters are identified as containing multiple-peaked Lyα emission using the criteria described above. Higher resolution (i.e., 600-line grism) and S/N (i.e., deeper 400-line grism) spectra are more likely to have identifiable multiple-peaked Lyα emission if it is present. Based on the 600-line and deep 400-line samples I therefore assert that the prevalence of multiple-peaked profiles among objects with Lyα emission is ~30% in a sample of UV-selected star-forming galaxies at $z \sim 2 - 3$. This percentage references a S/N lower limit of 3 on the strongest flux peak and a resolution limit of 225 km s^{-1}. From this analysis I have shown that multiple-peaked Lyα emission profiles can be used to statistically examine the velocity field and density distribution of the gas surrounding UV-selected star-forming galaxies at $z \sim 2 - 3$.

In order to access the rest-frame optical nebular emission lines (Hα at $z \sim 2$ and [O III]λ5007 at $z \sim 3$) enabling the determination of systemic velocities for the galaxies, the sample is restricted to those objects in the full multiple-peaked sample whose redshifts ensure that either Hα or [O III]λ5007 falls into a window of atmospheric transmission. The sharply increasing thermal background past 2.3 μm further limits the redshift range over which rest-frame optical emission lines are accessible. In the *K*-band the available redshift range is $z \sim 2.0 - 2.6$ for Hα and $z \sim 2.9 - 3.7$ for [O III]. In the *H*-band [O III] can be accessed from $z \sim 1.9 - 2.6$. After applying the restricted redshift ranges to the multiple-peaked objects determined from the algorithm described above, I identified 193 objects as potential targets for near-infrared spectroscopic follow-up. From this sample the 18 objects described in this chapter were selected, which are representative in terms of their Lyα kinematics (see Section 2.4).

2.3 Observations And Data Reduction

Both near-IR and optical spectra are required for the analysis of the kinematics of Lyα emission profiles. In this section, both types of spectroscopic data, as well as the basic empirical measurements and uncertainties are described in this section.

2.3.1 NIRSPEC Observations And Data Reduction

Near-IR spectra were obtained using the NIRSPEC instrument (McLean et al. 1998) on the Keck II telescope. These data were collected during three observing runs in 2009 July, August, and October, for a total of 5 nights. On average the total exposure time for each object was 4×900 seconds, though the number of 900 second exposures per target ranged from 3 to 6 for a total integration time of 0.75 to 1.5 hours. All targets were observed with a $0.''76 \times 42''$ long slit. For most objects the N6 filter was used, which is a broad *H*+*K* filter centered at 1.925μm with a bandwidth of 0.75μm. For objects at $z \sim 2.5 - 2.6$, the N7 filter was used, which is centered at 2.23μm with a bandwidth of 0.80μm. The spectral resolution as determined from sky lines was $\sim$ 15 Å, which corresponds to Δv ~230 km s^{-1} (R≃1300) for the N6 filter and Δv ~200 km s^{-1} (R≃1500) for the N7 filter. Conditions were photometric, with the seeing ranging from $0.''33 - 0.''70$.

Due to the faint nature of these objects in the *K*-band, each target was acquired using blind offsets from a bright star in the surrounding field. I returned to the offset star between each integration of the science target to recenter and dither along the slit. In nearly all cases dithering took place back and forth between two positions near the center of the slit. The position angle was chosen to match that of the LRIS observation unless the object appeared extended at

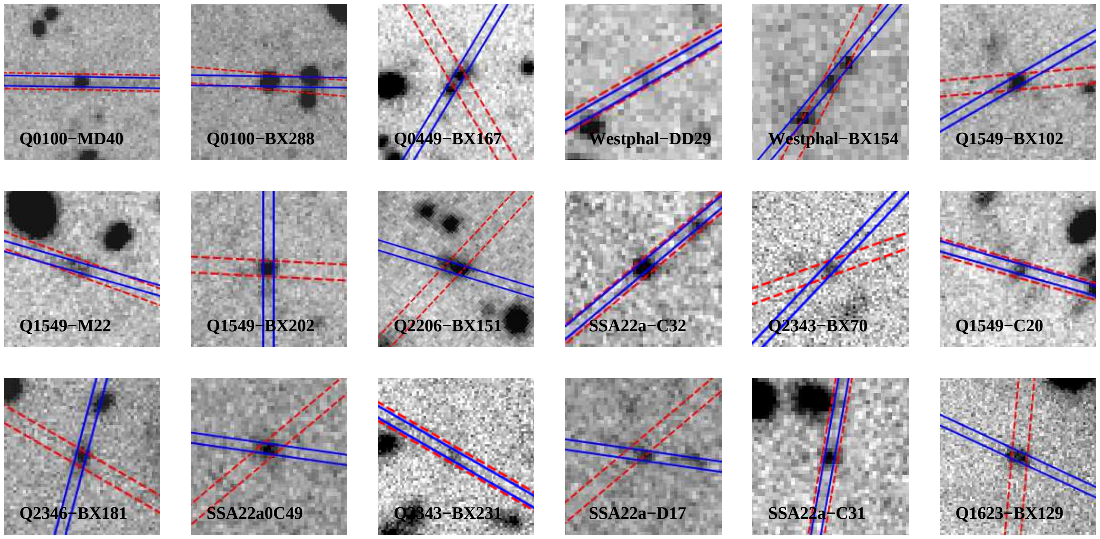

Figure 2.1 $\mathcal{R}$-band images (rest-frame UV) for the sample of 18 objects. In each image, the NIRSPEC long slit position is overlaid with blue, solid lines. The LRIS slit is overlaid with red, dashed lines. All images are $12'' \times 12''$, with north up and east to the left. Typical seeing during these exposures was $0.''8 - 1.''0$.

a different angle in the existing $\mathcal{R}$-band images (Steidel et al. 2003, 2004). I measured Hα or [O III]λ5007 for a total of 18 objects during the observing runs, which were drawn from the parent sample discussed in Section 2.2. All observational information can be found in Table 2.1. $\mathcal{R}$-band images of the objects with the NIRSPEC and LRIS slits overlaid are presented in Figure 2.1.

Data reduction was performed following the method described in Liu et al. (2008), where the sky background was subtracted from the two-dimensional unrectified science images using an optimal method (Kelson 2003, G. D. Becker 2006, private communication). After background subtraction, cosmic rays and bad pixels were removed from each exposure, which was then rotated, cut out along the slit, and rectified in two dimensions to take out the curvature both in the wavelength and spatial directions. The sky lines were fit with a low-order polynomial and a b-spline fit was used in the dispersion direction. The final rectified two-dimensional exposures for each object were then registered and combined into one spectrum. A one-dimensional spectrum was extracted from the two-dimensional reduced image along with the corresponding 1σ error spectrum. The average aperture size along the slit was $2\farcs1$, with a range of $1\farcs7$ to $2\farcs9$. The spectrum was then flux-calibrated using A-type stars observed during the NIRSPEC runs according to the method described in Shapley et al. (2005a) and Erb et al. (2003). Finally the flux-calibrated, one-dimensional spectrum was placed in a vacuum, heliocentric frame.

Table 2.1. Observation Log With Keck II NIRSPEC

Object	R.A. (J2000)	Dec. (J2000)	z_{HII}[a,b]	$\mathcal{R}$(mag)	Exposure (s)	Filter	Date (UT)
Q0100-MD40	1 03 18.971	13 17 02.841	2.2506	24.35	4 × 900	N6	Aug. 09, 2009
Q0100-BX288	1 03 20.931	13 16 23.569	2.1032	23.75	2 × 900	N6	Aug. 09, 2009
Q0449-BX167	4 52 24.624	-16 39 15.284	2.3557	24.02	4 × 900	N6	Oct. 10, 2009
Westphal-DD29	14 17 25.936	52 29 32.219	3.2401	24.82	4 × 900	N6	Aug. 10, 2009
Westphal-BX154	14 17 32.173	52 25 51.044	2.5954	23.96	3 × 900	N7	July 02, 2009
Q1549-BX102	15 51 55.977	19 12 44.220	2.1932	24.36	3 × 900	N6	July 01, 2009
Q1549-C20	15 52 00.396	19 08 40.773	3.1174	24.87	3 × 900	N6	Aug. 10, 2009
Q1549-M22[c]	15 52 02.703	19 09 40.011	3.1535	24.85	1 × 900	N6	Jul. 03, 2009
					2 × 900	N6	Aug. 10, 2009
Q1549-BX202	15 52 05.090	19 12 49.818	2.4831	24.37	4 × 900	N6	July 01, 2009
Q1623-BX129	16 25 28.732	26 49 19.182	2.3125	24.04	5 × 900	N6	July 02, 2009
Q2206-BX151	22 08 48.650	-19 42 25.569	2.1974	24.03	4 × 900	N6	July 01, 2009
SSA22a-D17[d]	22 17 18.845	0 18 16.667	3.0851	24.27	6 × 900	N6	July 02, 2009
SSA22a-C49[d]	22 17 19.810	0 18 18.729	3.1531	23.85	6 × 900	N6	July 02, 2009
SSA22a-C31	22 17 22.885	0 16 09.492	3.0176	24.61	3 × 900	N6	July 03, 2009
SSA22a-C32	22 17 25.629	0 16 13.095	3.2926	23.68	4 × 900	N6	July 03, 2009
Q2343-BX70	23 45 55.934	12 44 50.317	2.4086	24.94	4 × 900	N6	Aug. 09, 2009

Table 2.1—Continued

Object	R.A. (J2000)	Dec. (J2000)	z_{HII}[a,b]	$\mathcal{R}$(mag)	Exposure (s)	Filter	Date (UT)
Q2343-BX231	23 46 20.108	12 46 16.812	2.4999	25.15	3 × 900	N6	Aug. 10, 2009
Q2346-BX181	23 48 31.827	0 21 39.077	2.5429	23.28	3 × 900	N7	July 01, 2009

Note. — Units of right ascension are hours, minutes, and seconds, and units of declination are degrees, arcminutes and arcseconds.

[a]Rest-frame optical nebular emission-line redshifts. Objects with $z \sim 2.0 - 2.6$ have Hα measurements. Objects with $z > 3$ have [O III]λ5007 measurements.

[b]Typical uncertainty in z_{HII} is $\Delta z \sim 10^{-4}$.

[c]Object Q1549-M22 was observed on both July 3$^{\rm rd}$ and August 10$^{\rm th}$ and the science images from these nights were stacked together.

[d]Objects SSA22a-D17 and SSA22a-C49 were obtained on the same slit.

2.3.1.1 Objects With Spatially-Resolved NIRSPEC Spectra

While the majority of the objects in the sample have spatially unresolved Hα (or [O III]λ5007) emission-line spectra, three objects exhibit spatially-extended nebular emission: Q0449-BX167, Q2206-BX151, and Q1549-M22. If spatially-extended emission is coupled with rotation or velocity shear, the placement or position angle of the long slit has the potential to yield nebular emission centroid and velocity dispersion values that differ from the true properties of the galaxy. The differences may result if the slit does not evenly sample both the approaching and receding parts of the rotation curve or if systematic shear across the galaxy is interpreted as purely random motions. The three objects listed above were analyzed in more detail to determine whether their complexity might have affected the overall measurements. In the $\mathcal{R}$-band image for Q0449-BX167 there are two distinct components and the slit PA was chosen to have both components included. Q0449-BX167 has two separate components in the two-dimensional NIRSPEC spectrum that are offset in the spatial direction by $1.''3$, but not in the spectral direction. In the $\mathcal{R}$-band image, Q2206-BX151 is extended and the slit PA was chosen to encompass the extended region. In the two-dimensional NIRSPEC spectrum Q2206-BX151 is extended in the spatial direction for a total of $1.''3$. There is a small tail that extends off of the main nebular emission, which is slightly offset in the spectral direction. The flux from the tail is comparable to the noise seen in the image and was not extracted. Since the structure in the two-dimensional spectra for Q0449-BX167 and Q2206-BX151 (excluding the tail) is not shifted in the spectral direction there is no significant evidence for rotation or shear, and the nebular emission centroid and dispersion values for these objects should be robust. In fact, Q0449-BX167 and Q2206-BX151 have among the smallest velocity dispersion values of the sample. The third object, Q1549-M22, is slightly extended in the $\mathcal{R}$-band image and again the slit PA was chosen to correspond to the extended region. There are two distinct components in the two-dimensional spectrum for Q1549-M22 and they are offset by $1.''1$ and 9 Å, respectively, in the spatial and spectral directions. The two-dimensional NIRSPEC spectra for these three objects are presented, along with their corresponding two-dimensional LRIS spectra, in Figure 2.2.

Object Q0449-BX167 was originally extracted to include only the brighter component on the left hand side of the two-dimensional spectrum. To determine if the spatially-extended nebular emission affects the measurements, I re-extracted Q0449-BX167 to include both components seen in the two-dimensional spectrum. For Q0449-BX167 the centroid did not change and the velocity dispersion changed by $\Delta\sigma_v = +2.5$ km s^{-1} when comparing the more extended extraction to the original one. This difference is within the quoted errors. This analysis utilizes the values obtained from the original extraction of Q0449-BX167. Object Q2206-BX151 was originally extracted to include only the main elongated component. I re-extracted to include the tail for comparison. The centroid of the re-extraction did not change compared to the centroid measured from the original extraction. The velocity dispersion changed from an upper limit of 41 km s^{-1} (not including the tail) to a measurement of 63 km s^{-1} (including the tail). The re-extractions show that the centroid measurements used in the analysis for Q0449-BX167 and Q2206-BX151 are robust. I include the velocity dispersion values measured from the original extraction for Q2206-BX151 in the analysis with the caveat that the added complexity might affect the modeling comparison (see Section 2.6).

The fiducial measurements for Q1549-M22 are based on the extraction of both spectral components. Further analysis was conducted to understand how the spectral offset between the two components might affect the measurements.

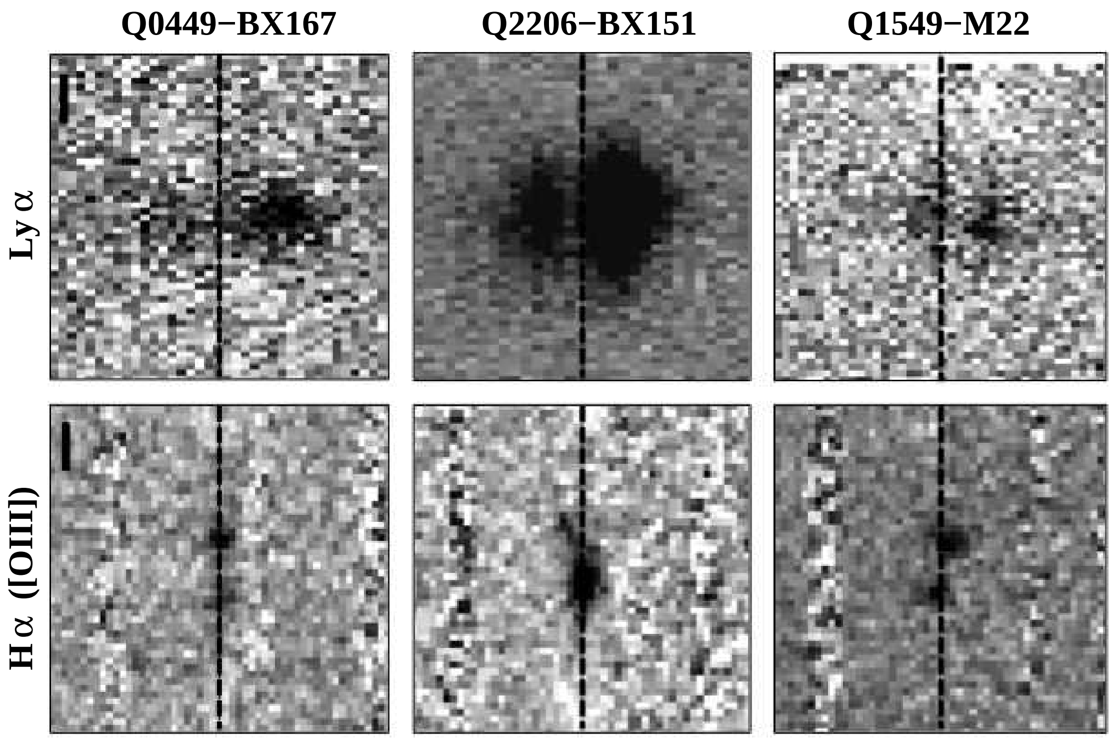

Figure 2.2 From left to right, the two-dimensional LRIS and NIRSPEC spectra for Q0449-BX167, Q2206-BX151, and Q1549-M22. These three objects exhibit spatially-extended nebular emission. The horizontal and vertical axes represent, respectively, velocity with respect to the velocity zeropoint and spatial distance along the slit. In each image, the dashed vertical line represents the systemic velocity of the system ($v = 0$), and the horizontal axis spans $\pm 1,500$ km s^{-1} in velocity. The vertical axes span $\pm 3.5''$ in the spatial direction, and a vertical scale bar of $1''$ is shown in the upper left-hand panels for Q0449-BX167. (Top) LRIS 2D Lyα spectra. (Bottom) NIRSPEC 2D spectra. The spectra of Q0449-BX167 and Q2206-BX151 show the Hα feature, while the spectrum of Q1549-M22 is centered on [O III]λ5007. Q0449-BX167 has two components separated by $1.''3$ along the slit, Q2206-BX151 is extended spatially by $1.''3$, and Q1549-M22 consists of two components separated by $1.''1$ in the spatial direction and 130 km s^{-1} in the spectral direction.

Each component was extracted and reduced separately for comparison with the integrated extraction of both components. Relative to the velocity zeropoint measured from the summed components, the offsets measured for each component separately are $\Delta v = 110$ km s^{-1} and $\Delta v = -76$ km s^{-1}. The measured velocity dispersion of the spectrum integrated over both components (153 km s^{-1}) is approximately equal to the sum in quadrature of the velocity dispersion of the individual components (125 km s^{-1} and 95 km s^{-1}). The shift from the velocity zeropoint of each component and the large measured velocity dispersion from the summed spectra (the largest in the sample) may be evidence of two separate components giving rise to the two Lyα peaks for this object. Object Q1549-M22 is still included in the sample with the caveat that its complexity in both [O III]λ5007 and Lyα may signify a different underlying phenomenon giving rise to the multiple-peaked Lyα emission from the one that I discuss in subsequent sections.

2.3.2 LRIS Data Reduction

The observations and reduction of the LRIS spectra for the target sample have been described in previous work (Steidel et al. 2003, 2004). These spectra were collected over the course of many years without consistent attention to the accuracy of the zeropoint of the wavelength solution at the 50 to 100 km s^{-1} level, given that their primary purpose was for the measurement of redshifts and basic galaxy properties. In contrast, for the work presented here it is crucial to obtain a uniform and highly accurate wavelength zeropoint in order to place the LRIS and NIRSPEC data sets on the same velocity scale. Accordingly, I re-calculated the wavelength solution of each LRIS spectrum. After computing the wavelength solution using the `IRAF` routine `identify` I adjusted the zeropoint of the solution such that bright, unblended sky lines (e.g., $\lambda5577.339$, $\lambda6300.304$) showed up at the correct wavelengths. The spectra were then corrected from an observed, air frame to a heliocentric, vacuum one.

2.3.3 Line Centroid, Flux, And FWHM Measurements

Measuring an accurate nebular emission centroid in order to obtain a precise systemic redshift for each objects was the principal objective of the NIRSPEC observations described in Section 2.3.1. The flux and FWHM are also important measurements for this analysis. The lines that I set out to measure were Hα at $z \sim 2$ and [O III]$\lambda5007$ at $z \sim 3$. The centroid, flux, and FWHM were determined by fitting a Gaussian profile to each emission line using the `IRAF` task, `splot`.

A Monte Carlo approach was used to measure the uncertainties in the centroid, flux, and FWHM. For each object 500 fake spectra were created by perturbing the flux at each wavelength of the true spectrum by a Gaussian random number with the standard deviation set by the level of the 1σ error spectrum. Line measurements were obtained from the fake spectra in the same manner as the actual data. The standard deviation of the distribution of measurements from the artificial spectra was adopted as the error on each centroid, flux, and FWHM value. The NIRSPEC measurements and associated uncertainties are given in Table 2.2. The FWHM values listed are not corrected for instrumental broadening. Based on Hα or [O III]$\lambda5007$ emission line centroid measurements, the systemic redshifts for the sample was obtained. These redshifts were used to shift both the NIRSPEC and LRIS spectra into the systemic rest frame. Based on the Monte Carlo uncertainty of the nebular emission line centroid or the RMS of the wavelength solution (depending on which was greater), I obtain an error of $\Delta\lambda \sim 0.9$ Å, which corresponds to a $\Delta v \sim 10 - 15$ km s^{-1}. Repeat observations of two objects from the sample using different slit PAs suggest a larger systematic uncertainty on the order of 50 km s^{-1}. However, this value should be considered an upper limit on the redshift uncertainty given that the slit positions between NIRSPEC and LRIS observations were matched for a significant fraction of the sample.

2.4 Lyα Velocity Profiles

Multiple-peaked Lyα emission profiles in $z \sim 2-3$ UV-selected galaxies in principle encode a wealth of information about the velocity and density fields through which they have propagated. It is known that many galaxies at this redshift range are experiencing outflows (Shapley et al. 2003; Veilleux et al. 2005). Simple galactic wind models that incorporate radiative transfer suggest that the specific velocity profile of the resultant Lyα line *relative to systemic* can be used to determine parameters of the wind such as the expansion velocity, column density of windswept material, and outflow temperatures (Verhamme et al. 2006, 2008). With the measured systemic redshifts and Lyα morphologies, the systems can now be analyzed with this comparison in mind. After being shifted to the systemic rest frame based on Hα or [O III] redshifts, the LRIS Lyα spectra were translated from wavelength to velocity space using the rest wavelength of the Lyα feature to create the Lyα velocity profiles. The velocity profiles are shown in Figure 2.3 and the corresponding velocity measurements for each peak and trough are shown in Table 2.3.

Table 2.2. NIRSPEC Measurement Results

Object	z_{HII}[a]	FWHM_{HII}[a,b]	F_{HII}[a,c]
Q0100-MD40[d]	2.2506	14.3 ± 1.0	3.6 ± 0.3
Q0100-BX288	2.1032	19.6 ± 0.4	6.7 ± 0.1
Q0449-BX167	2.3557	17.3 ± 1.4	7.8 ± 0.7
Westphal-DD29	3.2401	22.9 ± 1.3	22.9 ± 0.5
Westphal-BX154	2.5954	17.7 ± 2.0	7.7 ± 0.8
Q1549-BX102	2.1932	18.2 ± 1.1	6.1 ± 0.3
Q1549-C20	3.1174	17.3 ± 1.0	7.3 ± 0.4
Q1549-M22	3.1535	29.2 ± 2.8	8.1 ± 0.6
Q1549-BX202	2.4831	26.2 ± 9.9	4.2 ± 0.9
Q1623-BX129	2.3125	21.1 ± 2.9	3.5 ± 0.4
Q2206-BX151[e]	2.1974	15.7 ± 0.7	6.3 ± 0.3
SSA22a-D17	3.0851	25.1 ± 2.5	2.6 ± 0.3
SSA22a-C49	3.1531	18.0 ± 0.6	6.4 ± 0.2
SSA22a-C31	3.0176	19.7 ± 1.5	11.5 ± 0.9
SSA22a-C32[d]	3.2926	12.8 ± 35	5.2 ± 4.7
Q2343-BX70[e]	2.4086	16.6 ± 3.5	4.0 ± 0.6
Q2343-BX231	2.4999	21.5 ± 1.1	7.2 ± 0.4
Q2346-BX181	2.5429	28.3 ± 2.6	13.8 ± 1.2

[a]Rest-frame optical nebular emission-line redshifts. Objects with $z \sim 2.0 - 2.6$ have Hα measurements. Objects with $z > 3$ have [O III]λ5007 measurements.

[b]Observed FWHM and error in units of Å. The FWHM is a raw value, uncorrected for instrumental broadening.

[c]Emission-line flux and error in units of 10^{-17} ergs s^{-1} cm^{-2}.

[d]Measured FWHM is less than instrumental resolution.

[e]Measured FWHM is not appreciably higher than the instrumental resolution.

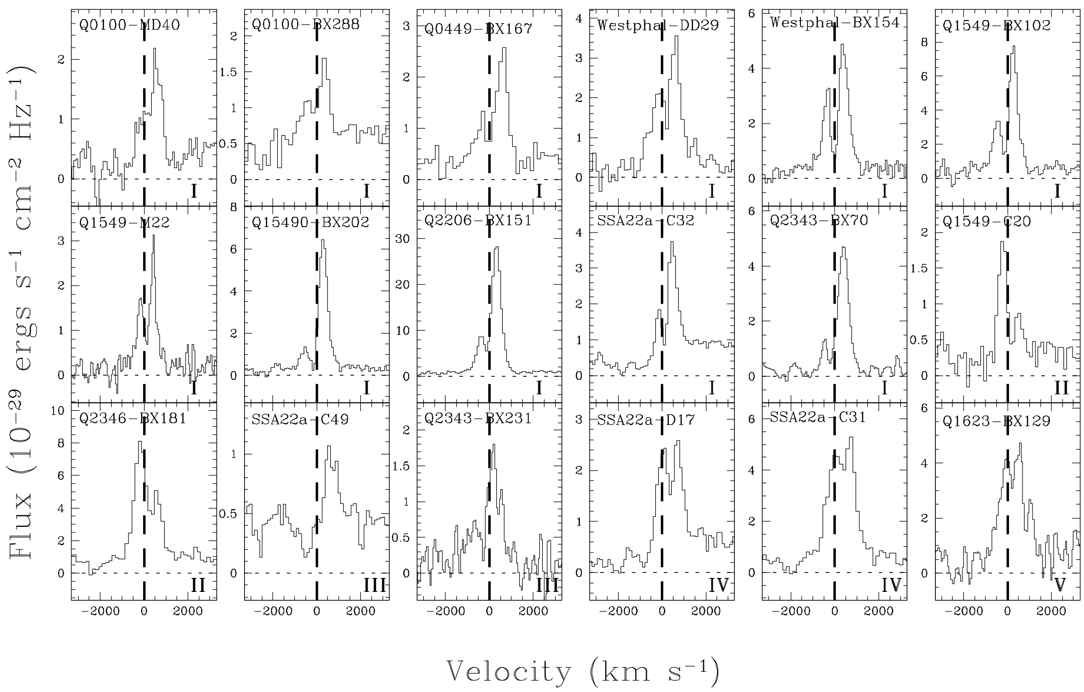

Figure 2.3 Lyα velocity profiles for the 18 objects in the sample. The zeropoint velocity as measured from the nebular emission (Hα at $z \sim 2$ or [O III]λ5007 at $z \sim 3$) is indicated on each image with a dashed line. Considerable variety is evident among the line profile peaks and their ratios. From top to bottom and left to right, the panels proceed from Group I to Group V profiles.

Table 2.3. Velocity Measurements: Lyα Emission And Interstellar Absorption

Object	z_{HII}[a]	First Peak[b]	Second Peak[b]	Trough[b]	Absorption[b]	Grism/Grating[c]
Q0100-MD40[d]	2.2506	−461	+550	+288	−19	600, 400
Q0100-BX288	2.1032	−579	+377	−104	−317	400
Q0449-BX167	2.3557	−348	+586	−60	−47	400
Westphal-DD29	3.2401	−259	+471	+202	···	300
Westphal-BX154	2.5954	−353	+404	−27	−204	600
Q1549-BX102	2.1932	−478	+264	−155	···	600
Q1549-C20	3.1174	−237	+533	+210	+14	400
Q1549-M22	3.1535	−153	+414	+111	···	600
Q1549-BX202	2.4831	−542	+301	−141	−143	600
Q1623-BX129[e]	2.3125	−42	+542	+229	−468	400
Q2206-BX151	2.1974	−417	+328	−148	···	600
SSA22a-D17	3.0851	−25	+732	+385	−1174	400
SSA22a-C49	3.1531	+518	+903	+735	−232	400
SSA22a-C31	3.0176	−15	+695	+424	···	300
SSA22a-C32	3.2926	−155	+493	+99	−24	400
Q2343-BX70	2.4086	−476	+399	−214	−33	400
Q2343-BX231	2.4999	+84	+567	+399	···	400

Table 2.3—Continued

Object	z_{HII}[a]	First Peak[b]	Second Peak[b]	Trough[b]	Absorption[b]	Grism/Grating[c]
Q2346-BX181	2.5429	−214	+626	+338	−49	400

[a]Rest-frame optical nebular emission-line redshifts. Objects with $z \sim 2.0 - 2.6$ have Hα measurements. Objects with $z > 3$ have [O III]λ5007 measurements.

[b]Velocity relative to systemic in units of km s^{-1}.

[c]All Lyα spectra were obtained on the LRIS spectrograph at Keck Observatory. These spectra were taken with the 300 line mm^{-1} grating blazed at 5000 Å, or the 400 line mm^{-1} or 600 line mm^{-1} grism blazed at 3400 Å, and 4000 Å, respectively, following the LRIS-B upgrade (Steidel et al. 2004).

[d]Object Q0100-MD40 had two spectra taken at separate observing runs, with separate gratings. Both were combined to make the final spectrum.

[e]Object Q1623-BX129 contains a third peak. The corresponding velocity is +1051 km s^{-1}, while the second trough is at +846 km s^{-1}.

The Lyα velocity profiles can be separated into groups characterized by the strengths and locations of the emission peaks with respect to the velocity-field zeropoint. The majority of objects in the sample (11/18), which I refer to as Group I, have two peaks that straddle the velocity-field zeropoint, with the stronger flux peak on the red side. This group includes objects Q0100-MD40, Q0100-BX288, Q0449-BX167, Westphal-DD29, Westphal-BX154, Q1549-BX102, Q1549-M22, Q1549-BX202, Q2206-BX151, SSA22a-C32, and Q2343-BX70. In the case of Q1549-M22, the object with two apparently distinct spectral and spatial [O III] emission components, regardless of whether the velocity-field zeropoint is shifted to $\Delta v = 110$ km s^{-1} or $\Delta v = -76$ km s^{-1}, as measured from the re-extraction of each component individually, both Lyα peaks still straddle the zeropoint. Therefore Q1549-M22 is classified as a Group I object independent of the adopted velocity zeropoint. Group II spectra, including objects Q1549-C20 and Q2346-BX181, are described by two peaks that straddle the velocity-field zeropoint, and have the stronger flux peak on the blue side. Objects Q2343-BX231 and SSA22a-C49 comprise Group III, where the bluer Lyα peak is stronger, but unlike the profiles previously described, both peaks are shifted completely redward of the zeropoint. Group IV, SSA22a-D17 and SSA22a-C31, have two peaks that straddle the velocity-field zeropoint with both peaks having approximately the same flux with the red peak marginally stronger. Object Q1623-BX129 accounts for the last group, Group V. This object has three peaks. Two of the peaks are similar to those of SSA22a-D17 and SSA22a-C31, with nearly the same flux and one on either side of the zeropoint. The third peak, which is furthest redward from the zeropoint, has the smallest flux. Examples of two-dimensional Lyα spectra from each group are displayed in Figure 2.4.

A precise velocity-field zeropoint in addition to the velocity dispersion (see Section 2.5.1) provides constraints on radiative transfer models of the Lyα emis-

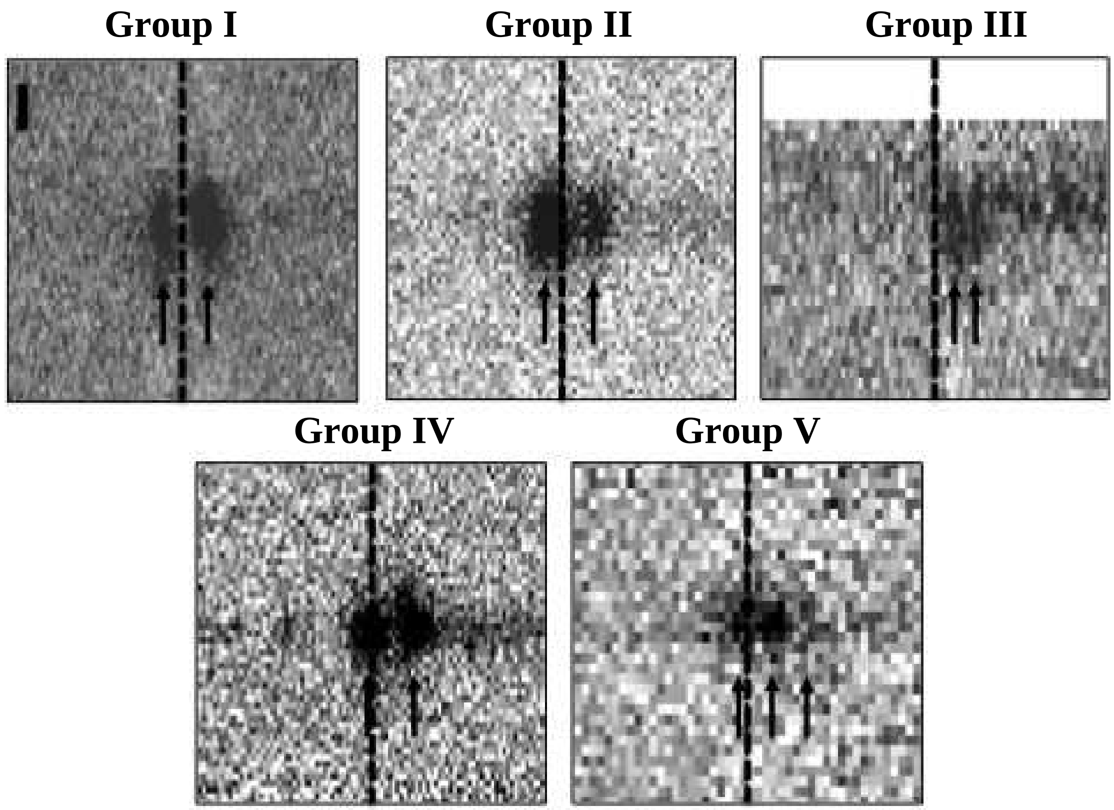

Figure 2.4 Two-dimensional Lyα emission spectra representing each of the 5 groups. For each image the horizontal axis represents velocity with respect to the velocity zeropoint, where the dashed vertical line represents the systemic velocity ($v = 0$). The horizontal axis in each panel spans $\pm 3,000$ km s^{-1}. The vertical axis represents spatial distance along the slit, with a span of $\pm 3.5''$, and a vertical scale bar of $1''$ is shown in the upper left-hand panel (labeled Group I). Group I (two peaks that straddle the velocity-field zeropoint, with the stronger flux peak on the red side) is represented by Westphal-BX154, Group II (two peaks that straddle the velocity-field zeropoint, with the stronger flux peak on the blue side) is represented by Q2346-BX181, Group III (both peaks are shifted completely redward of the zeropoint, with the stronger flux peak on the blue side) by SSA22a-C49, Group IV (two peaks that straddle the velocity-field zeropoint with both peaks having approximately the same flux with the red peak marginally stronger) by SSA22a-D17, and Group V (three peaks) by Q1623-BX129. In each panel, the locations of the Lyα peaks are indicated by arrows.

sion from the sample of galaxies (see Section 2.6). Figure 2.5 shows a graphical summary of peak velocities along with the relative fluxes of each peak for every galaxy in the sample. Additionally, some objects have detectable interstellar absorption lines, which are also labeled on Figure 2.5. The analysis of the absorption lines is described in Section 2.5.4. The velocity separation of the peaks in the Lyα profiles is also an important constraint on possible models. The mean velocity peak separation is $\langle \Delta v_{peak} \rangle = 741 \pm 39$ km s^{-1} (where the error represents the standard deviation of the mean), and the median is $\Delta v_{peak,med} = 757$ km s^{-1}.

An examination of the parent LRIS multiple-peaked sample indicates the same trends as described above. Analyzing the objects in the parent sample with a S/N lower limit of 3 on the strongest flux peak reveals that ∼65% have their strongest flux peak located on the red side of the interpeak trough (compared to 72% from the NIRSPEC sample). Despite a wide range from minimum to maximum for the peak-to-peak velocity separation, the statistics for the parent LRIS sample are comparable to those for the NIRSPEC sample, with a mean value of $\langle \Delta v_{peak} \rangle = 723 \pm 18$ km s^{-1} (where the error represents the standard deviation of the mean), and a median of $\Delta v_{peak,med} = 721$ km s^{-1}. Figure 2.6 shows the distributions of peak-to-peak velocity separation for the NIRSPEC sample and the parent LRIS sample. These distributions demonstrate that the sample of 18 objects with NIRPSEC observations is representative of the parent LRIS sample as a whole.

2.5 Physical Quantities

In this section, several relevant physical properties are discussed for the NIRSPEC multiple-peaked sample objects that can be estimated from the combined data set.

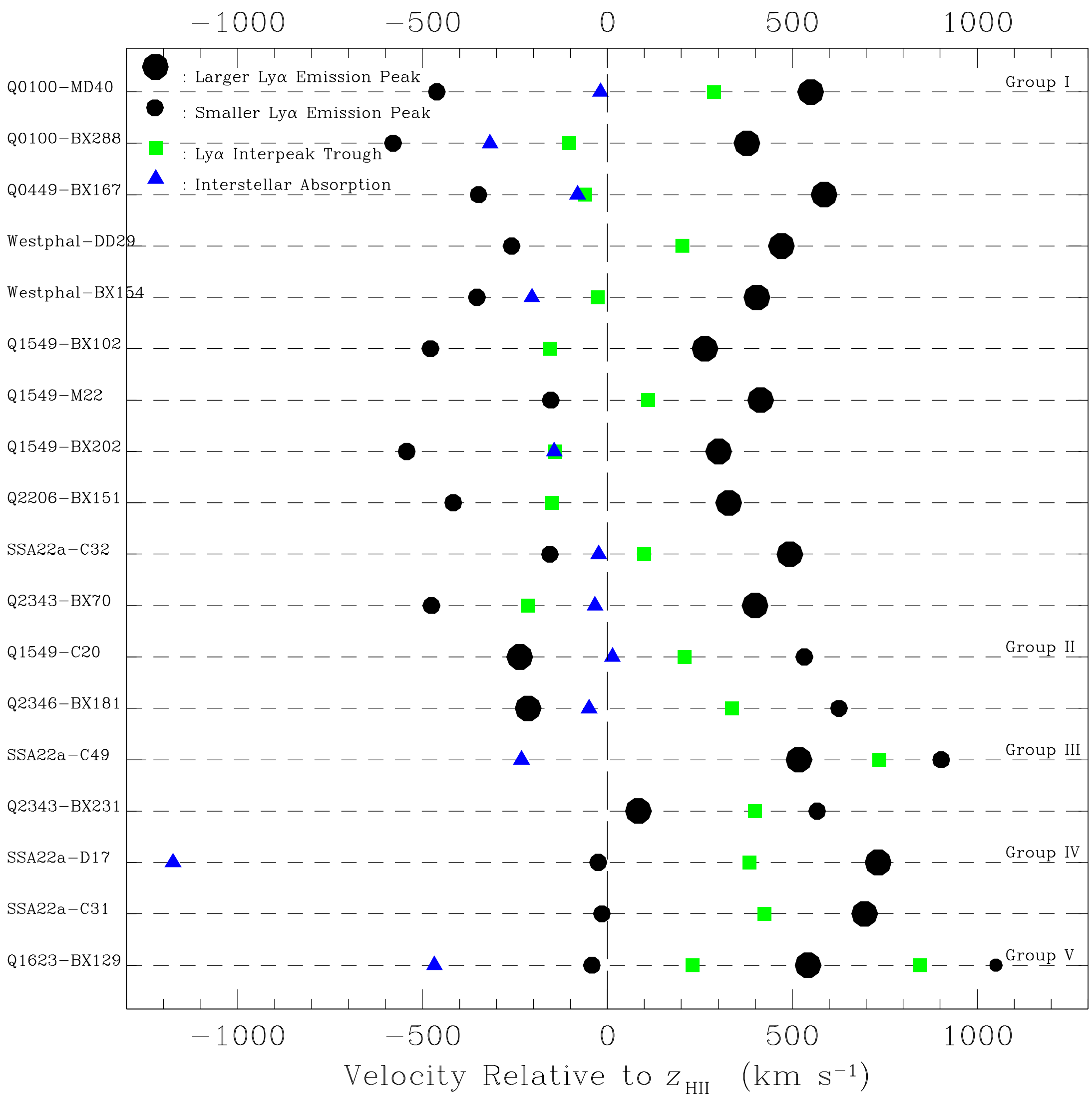

Figure 2.5 The location of the velocity for every peak, trough, and absorption line with respect to the velocity-field zeropoint. From top to bottom, the properties are displayed for Group I, II, III, IV, and V objects. Objects are offset vertically for clarity. In each line the larger [smaller] black dot represents the velocity peak with the larger [smaller] flux. The green square represents the velocity of the trough between the peaks. The blue triangle represents the absorption line velocity if it was measured for the object. For Q1623-BX129, which has three measured peaks, an even smaller black dot is used to indicate the third peak with the weakest flux.

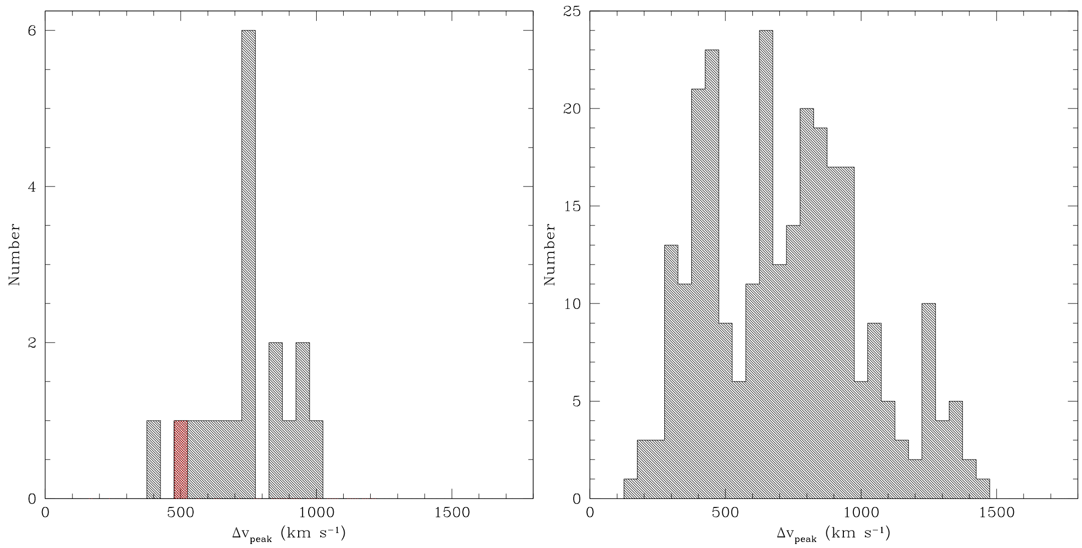

Figure 2.6 Histogram of the distribution of peak-to-peak velocity separation. (Left) The histogram for the 18 objects with NIRSPEC measurements. The red shaded bar represents the separation of the 2nd peak (the center peak) from the 3rd peak (the reddest peak) for object Q1623-BX129. The mean value for the sample is $\langle \Delta v_{peak} \rangle = 741 \pm 39$ km s^{-1}, with a median of $\Delta v_{peak,med} = 757$ km s^{-1}. (Right) Histogram of the peak-to-peak separation for the parent LRIS sample with a S/N lower limit of 3. The mean value is $\langle \Delta v_{peak} \rangle = 723 \pm 18$ km s^{-1}, with a median of $\Delta v_{peak,med} = 721$ km s^{-1}.

2.5.1 Velocity Dispersion

As traced by Hα (or [O III]λ5007) emission, the nebular velocity dispersion, σ_v, reflects the integrated emission from star forming regions, which should reveal the potential well within the central few kiloparsecs of a high-redshift star-forming galaxy. Since the Hα (or [O III]λ5007) velocity dispersion also traces the initial velocity dispersion of the Lyα photons, it is an important input parameter for models of Lyα radiative transfer and will enable a better understanding of the multiple-peaked Lyα emission systems in the sample. In this doctoral thesis, aside from a brief comparison with previous work (Section 2.6.2), I do not include a detailed analysis of the relationship between intrinsic velocity dispersion and the emergent Lyα profile. Such analysis is deferred to future work, as discussed in Section 2.7 and Section 5.

The velocity dispersion was calculated as $\sigma_v = (\mathrm{FWHM}/2.355) \times (c/\lambda_{obs})$, where λ_{obs} is the observed wavelength of Hα or [O III]λ5007. The FWHM is determined from the subtraction of the instrumental FWHM (estimated from the widths of night sky lines) from the observed FWHM in quadrature. Uncertainties in the velocity dispersion were determined using the same method described in Erb et al. (2006c). Of the 18 objects, 14 have measurable velocity dispersion. For 2 additional objects I obtained an upper limit in the velocity dispersion because the measured line width was not appreciably higher than the instrumental resolution. Finally, 2 objects have measured line widths that are smaller than the instrumental resolution and are therefore considered unresolved. Figure 2.7 shows the distribution of the velocity dispersion for the sample. The mean value for the sample of 14 objects with measurable velocity dispersion is $\langle\sigma_v\rangle = 90 \pm 9$ km s^{-1} (where the error represents the standard deviation of the mean), while the median for the full sample of 18 objects is $\sigma_{v,med}$= 82 km s^{-1}. These numbers are similar to the typical values reported by Erb et al. (2006c) and Pettini et al. (2001) for $z \sim 2-3$ UV-selected galaxies ($\sigma_v = 108 \pm 5$ km s^{-1} for $z \sim 2$ and $\sigma_v = 84 \pm 5$ km s^{-1} for $z \sim 3$).

2.5.2 Dust Extinction

Lyα emission can be significantly suppressed due to attenuation by dust. Commonly, dust extinction in $z \sim 2$ star-forming galaxies is estimated from rest-frame UV colors and an assumption of the Calzetti et al. (2000) starburst attenuation law. Alternatively, the amount of dust extinction can be estimated from the ob-

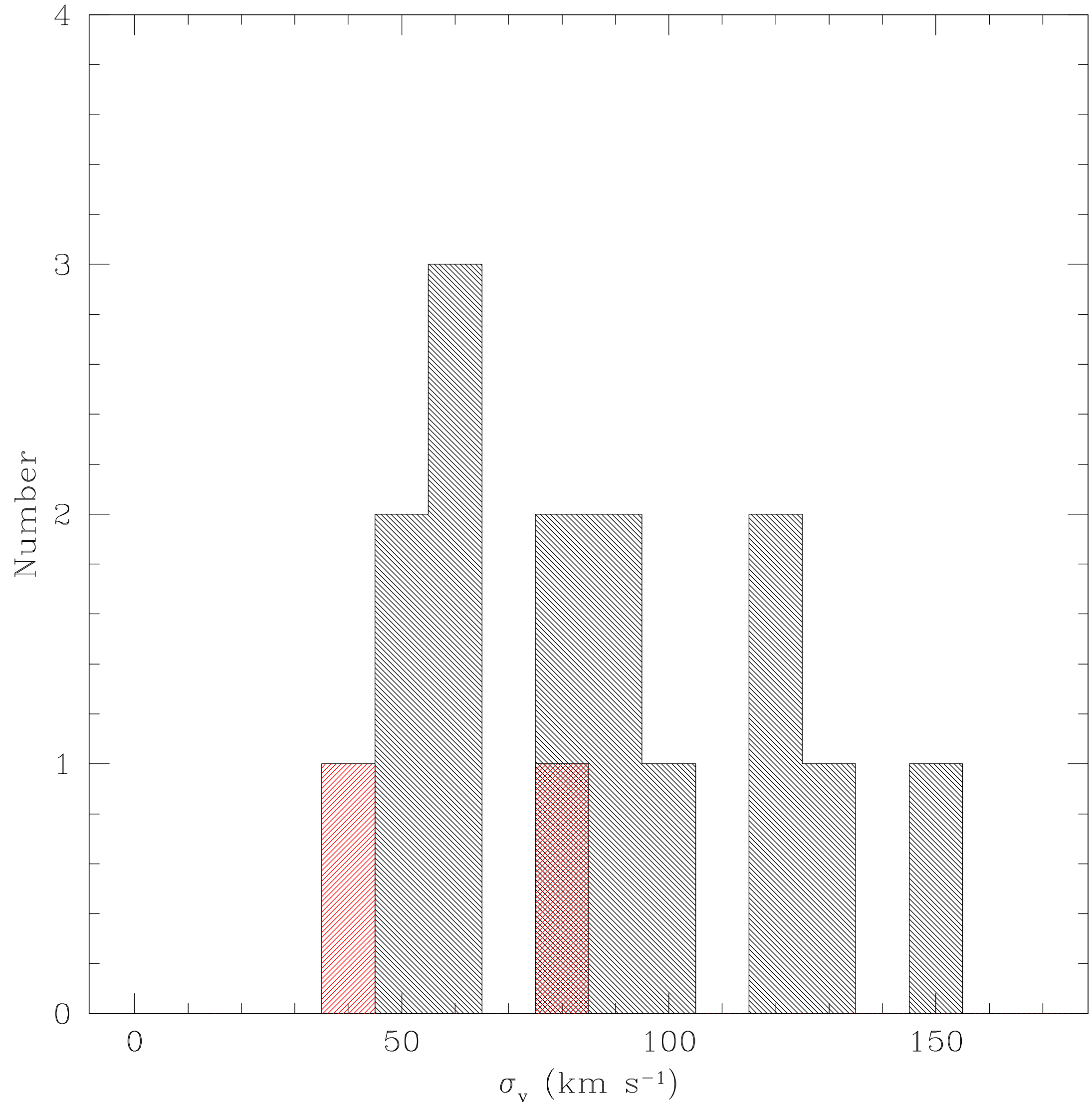

Figure 2.7 Histogram of the nebular velocity dispersion, σ_v, as traced by Hα or [O III]λ5007 measurements. The measurements for two objects with FWHM not appreciably larger than the instrumental resolution, Q2206-BX151 and Q2343-BX70, are shaded red. The two objects that are considered unresolved, Q0100-MD40 and SSA22a-C32, are not included in this figure. The mean value for the sample of 14 objects with measured velocity dispersions is $\langle\sigma_v\rangle = 90\pm\ 9$ km s^{-1}. The median value for the full sample of 18 objects is $\sigma_{v,med} = 82$ km s^{-1}.

served ratio of hydrogen Lyman to Balmer lines, since their intrinsic ratios are well described by atomic theory. An assumption of Case B recombination and $T = 10,000K$ determines the intrinsic Lyα to Hα ratio (Osterbrock 1989). Any deviation from this value is then attributed to dust extinction. In the sample, only 11 of 18 galaxies have measured Hα (the remainder have [O III]λ5007), making the first method more generally applicable for this analysis. Both methods were used to calculate $E(B-V)$ for objects with measured Hα.

For the first method, I used the $G-\mathcal{R}$ colors of the sample as determined from Steidel et al. (2003, 2004). If the Lyα line fell in the G-band (at $z \sim 2.48-3.28$) the color was corrected for emission-line contamination using $\Delta m = 2.5 \times \log(1 + \frac{EW}{\Delta G})$, where $\frac{EW}{\Delta G}$ is the ratio of the observed equivalent width of the Lyα emission feature to the bandwidth of the G filter (1100 Å). The correction, Δm, was then added to the $G-\mathcal{R}$ color. The $G-\mathcal{R}$ color for objects at $z > 2.45$ was also corrected for IGM absorption in the G-band (Madau 1995). An intrinsic SED model was assumed as well to estimate the dust extinction. The Bruzual & Charlot (2003) model was used assuming solar metallicity and constant star formation rate with a stellar age of 570 Myr for $z \sim 2$ and 202 Myr for $z \sim 3$ objects. The choice of stellar age for objects at $z \sim 2$ was based on results from Erb et al. (2006c), who found a median age of 570 Myr for star-forming galaxies in this redshift range. The stellar age of 202 Myr adopted for the $z \sim 3$ galaxies was based on results from Shapley et al. (2005a). The calculated values of $E(B-V)$ are listed in Table 2.4.

For the second method, based on the ratio of Lyα and Hα emission lines, the flux ratio $\frac{Ly\alpha_{(int)}}{H\alpha_{(int)}} = 8.7$ was adopted (Osterbrock 1989). The following equation can be used to determine the dust extinction:

$$\frac{Ly\alpha_{(obs)}}{H\alpha_{(obs)}} = 8.7 \times 10^{-0.4E(B-V)(\kappa_{Ly\alpha}-\kappa_{H\alpha})} \tag{2.1}$$

In this equation $\kappa_{Ly\alpha}$ and $\kappa_{H\alpha}$ refers to the selective extinction at the wavelengths of Lyα and Hα, respectively, as defined in Equation 4 of Calzetti et al. (2000). $E(B-V)$ can then be calculated based on the observed ratio of Lyα to Hα flux. All of the calculated $E(B-V)$ values from this method exceed those measured from the rest-frame UV colors, and the median excess is a factor of 1.5 (Figure 2.8). This difference may be explained with reference to Calzetti et al. (2000), which states that the stellar continuum in local star-forming galaxies should suffer less reddening than the ionized gas. Furthermore, Lyα may suffer additional extinction due to resonant scattering and an effectively longer path length through the interstellar medium. In practice, it is difficult to obtain a robust estimate of the Lyα to Hα ratio due to the effects of differential slit loss. Erb et al. (2006b) find that NIRSPEC Hα spectra using the $0.''76$ slit may result in a typical factor of ~ 2 loss, while Steidel et al. (2011) find that LRIS $1.''2$ slit spectra of Lyα may result in typical losses of a factor of ~ 5. In detail, the relative loss of Lyα to Hα depends on the spatial distribution of the emission in each of these lines. Overall, the Lyα losses appear to outweigh those of the Hα losses, which will tend to cause an underestimate in the Lyα to Hα ratio. Because of the systemic uncertainty of the Lyα to Hα ratio and due to the fact that I can only estimate $E(B-V)$ for half of the sample using the (uncertain) intrinsic ratio method, I adopt the values calculated from the rest-frame UV colors. The average value for the sample when employing the first method is $\langle E(B-V)\rangle = 0.09$, which is bluer than the typical value seen at these redshifts, $\langle E(B-V)\rangle = 0.15$ (Reddy et al. 2008). This difference is not surprising given that the sample is entirely composed of objects with Lyα emission and given the apparent anticorrelation between Lyα emission EW and dust extinction (Shapley et al. 2003; Kornei et al. 2010).

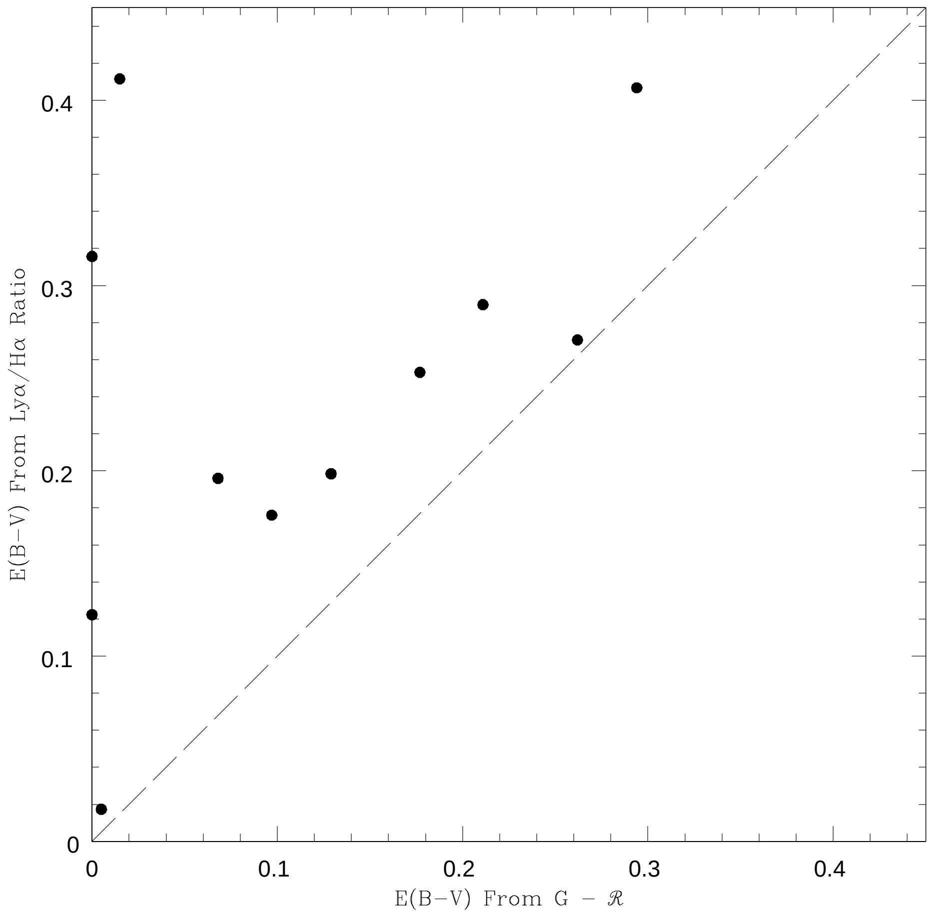

Figure 2.8 Comparison between $E(B-V)$ values calculated from the $G-\mathcal{R}$ colors (x-axis) and the Lyα to Hα ratio (y-axis). All of the calculated $E(B-V)$ values from the ratio of Lyα and Hα emission lines exceed those measured from the rest-frame UV colors by a median factor of 1.5. This difference can be explained if the stellar continuum suffers less reddening than the ionized gas (Calzetti et al. 2000). In addition, Lyα may suffer additional extinction due to resonant scattering. I adopt the $E(B-V)$ values measured from the rest-frame UV-colors for the entire sample since the Lyα to Hα ratio method can measure $E(B-V)$ for only 11 out of the 18 galaxies.

2.5.3 Star-Formation Rates And Intrinsic Luminosity

Star-formation rates (SFRs) were calculated from the rest-frame UV luminosity. For sources at $z \sim 2$, I used the G-band as a proxy for rest-frame UV luminosity. At $z \sim 3$, $\mathcal{R}$-band is used as an equivalent probe. The observed magnitudes were first corrected for dust extinction using $m_{corr} = m_{app} - (\kappa \times E(B-V))$, where κ is defined in Section 2.5.2. Given the range of redshifts in the $z \sim 2$ sample the G-band effective wavelength of 4780 Å corresponds to a rest-frame wavelength range of $1330 - 1540$ Å. For the $z \sim 3$ sample the $\mathcal{R}$-band effective wavelength translates to a rest-frame effective wavelength of $1590 - 1700$ Å. These rest-frame wavelengths were used to determine κ values. The corrected magnitude was then used to determine the flux, F_ν. Using the luminosity distance, I calculated the rest-frame UV luminosity density according to $L_\nu = (4\pi {D_L}^2 F_\nu)/(1+z)$. From Kennicutt (1998a), the relation of $\mathrm{SFR}(M_\odot\ \mathrm{yr}^{-1}) = 7.8 \times 10^{-29}\ L_\nu(\mathrm{ergs\ s^{-1}\ Hz^{-1}})$ was used to determine the SFRs assuming a Chabrier (2003) IMF. The SFRs for the sample range from $6-110\ M_\odot\ \mathrm{yr}^{-1}$. The average value is $32\ M_\odot\ \mathrm{yr}^{-1}$, which is fairly typical of UV-selected star-forming galaxies at $z \sim 2-3$ (Erb et al. 2006b). The intrinsic Lyα luminosity, $L_{Ly\alpha}$, can be derived from the SFR using the conversion described in Kennicutt (1998b) and again assuming a Chabrier (2003) IMF:

$$L_{Ly\alpha}(\mathrm{ergs\ s^{-1}}) = \frac{\mathrm{SFR}\ (M_\odot\ \mathrm{yr}^{-1})}{5.1 \times 10^{-43}} \tag{2.2}$$

Based on the average SFR of $32\ M_\odot\ \mathrm{yr}^{-1}$, the intrinsic Ly$\alpha$ luminosity is $\langle L_{Ly\alpha} \rangle = 6.3 \times 10^{43}$ ergs s^{-1}. The intrinsic Lyα luminosity is an important quantity for the models because it allows an accurate description of the photon source from the galaxies. SFRs and $L_{Ly\alpha}$ values are listed in Table 2.4.

Table 2.4. Physical Quantities

Object	σ_v [a]	$E(B-V)$ [b]	SFR[c]	$L_{\mathrm{Ly}\alpha}$ [d]
Q0100-MD40	$\cdots$	0.00	6	1.25
Q0100-BX288	84.8^{+3}_{-3}	0.02	11	2.16
Q0449-BX167	50.3^{+14}_{-19}	0.20	51	10.10
Westphal-DD29	102.5^{+10}_{-11}	0.00	73	14.90
Westphal-BX154	52.4^{+18}_{-24}	0.26	110	21.70
Q1549-BX102	64.6^{+10}_{-13}	0.10	13	2.51
Q1549-C20	55.2^{+11}_{-13}	0.04	9	1.83
Q1549-M22	153.1^{+19}_{-20}	0.15	27	5.23
Q1549-BX202	119.7^{+63}_{-84}	0.07	14	2.78
Q1623-BX129	89.5^{+22}_{-25}	0.00	9	1.74
Q2206-BX151	< 40.5	0.01	8	1.66
SSA22a-D17	124.9^{+19}_{-20}	0.08	24	4.84
SSA22a-C49	60.5^{+6}_{-7}	0.07	33	6.61
SSA22a-C31	82.0^{+14}_{-15}	0.00	8	1.59
SSA22a-C32	$\cdots$	0.04	31	6.19
Q2343-BX70	< 78.5	0.13	12	2.35
Q2343-BX231	86.3^{+8}_{-9}	0.29	47	9.20
Q2346-BX181	131.8^{+17}_{-17}	0.18	97	19.20

[a]Velocity dispersion measured in units of km s^{-1}.

[b]$E(B-V)$ value derived from $G-\mathcal{R}$ color.

[c]Star-formation rate measured in units of $M_\odot$ yr^{-1}.

[d]Intrinsic Lyα luminosity measured in units of 10^{43} ergs s^{-1}.

2.5.4 Interstellar Absorption

The evidence for feedback in high-redshift galaxies comes in several forms, one of which is the nature of rest-frame UV interstellar absorption lines. Interstellar material is swept up in a galaxy-wide outflow, causing a blueshift in the associated absorption lines. In the sample over half of the objects have detected interstellar absorption lines. These include both low-ionization (Si IIλ1260, Si IIλ1526, and C IIλ1334) and high-ionization (Si IV$\lambda\lambda$1393,1402 and C IV$\lambda\lambda$1548,1549) lines.

For all but two objects the absorption lines identified in the spectra are low-ionization species. The S/N of these lines is not exceptionally strong on an individual basis. In principle, all of the low-ionization lines arise in the same gas and should share the same z_{abs} and velocity profiles. Based on this idea I continuum-normalized and averaged the Si IIλ1260, Si IIλ1526, and C IIλ1334 velocity profiles to obtain better S/N. Figure 2.9 shows an example of one of the objects, Westphal-BX154, with averaged low-ionization lines, as well as object SSA22a-C49, which has measurements of both low- and high-ionization lines. The velocity offsets in the sample measured from the absorption line centroids range from $\Delta v_{abs} = +14$ to $-1,174$ km s^{-1}, relative to the systemic velocity. The average value of the interstellar absorption velocity offset for the sample is $\langle \Delta v_{abs} \rangle = -227$ km s^{-1}, which is indicative of large scale outflows (Pettini et al. 2001; Shapley et al. 2003; Steidel et al. 2010).

The line width of the interstellar absorption features was measured as $\sigma_{abs} =$ (FWHM/2.355) $\times$ (c/λ_{obs}), where λ_{obs} is the observed wavelength of the interstellar absorption line. The FWHM was corrected for instrumental resolution (σ_{inst} = (FWHM$_{inst}$/2.355) = 95, 155, 190 km s^{-1} for the 600, 400, 300-line grism, respectively). The line width, σ_{abs}, is a probe of the range of velocities present in the interstellar gas, which is an important observational constraint for

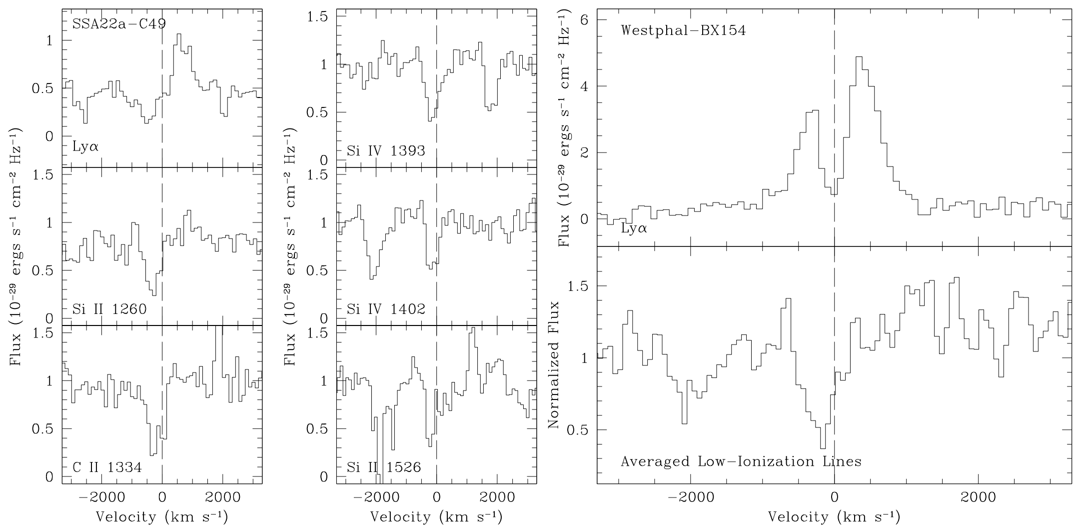

Figure 2.9 Interstellar absorption velocity profiles for two objects in the sample. Interstellar absorption lines were measured for 12 out of the 18 objects in the sample, and the majority have centroids that are blueshifted relative to the velocity zeropoint. (Left) Comparison of the Lyα and low- and high-ionization interstellar absorption velocity profiles for SSA22a-C49. All of the absorption-line velocity centroids appear blueward of the velocity-field zeropoint, whereas the Lyα velocity profile is shifted completely redward of the velocity-field zeropoint. (Right) Comparison of the Lyα and averaged low-ionization interstellar absorption velocity profiles of Westphal-BX154. The low-ionization lines, Si IIλ1260, Si IIλ1526, and C IIλ1334, were averaged to obtain better S/N. The absorption line velocity centroid is blueshifted relative to the velocity-field zeropoint. The two peaks of the Lyα velocity profile straddle the velocity-field zeropoint.

Lyα radiative transfer models (see Section 2.6). The average σ_{abs} for the 12 objects in the sample with absorption line measurements is 190 ± 63 km s^{-1} (where the error represents the standard deviation of the distribution of measurements). This line width is consistent with measurements made by Shapley et al. (2003) of $\langle\sigma_{abs}\rangle = 238 \pm 64$ km s^{-1} in a composite spectrum of 811 $z \sim 3$ Lyman Break Galaxies (LBGs) and Quider et al. (2009) of $\sigma_{abs} \sim 170{-}255$ km s^{-1} in the strong gravitationally lensed galaxy, "the Cosmic Horseshoe", at $z = 2.38$. The σ_{abs} values were measured from the combined low-ionization lines for each object except for SSA22a-C32, SSA22a-C49 and SSA22a-D17, where individual low-ionization lines were measured and then averaged. Figure 2.10 shows the distribution of the interstellar absorption line widths for the sample.

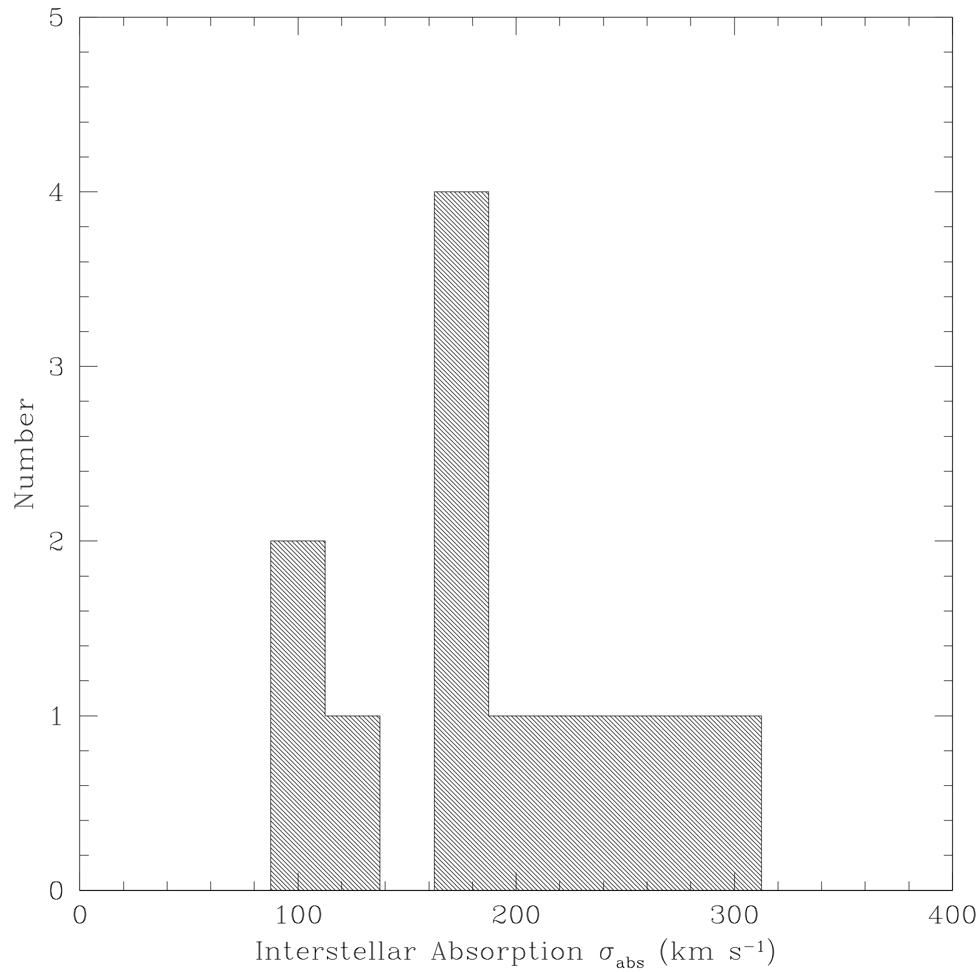

Figure 2.10 Histogram of interstellar absorption line widths, σ_{abs}. All σ_{abs} values were measured from the combined low-ionization lines for each object, except for SSA22a-C32, SSA22a-C49 and SSA22a-D17, where individual low-ionization lines were measured and then averaged. The mean value of the sample is $\langle\sigma_{abs}\rangle = 190 \pm 63$ km s^{-1}. The line width is an important parameter for modeling Lyα radiative transfer because it reveals the dynamics of the absorbing interstellar gas.

Additionally, I investigated if there was an inherent difference in the interstellar absorption line profiles for multiple-peaked compared to single-peaked Lyα emission spectra. For this comparison I constructed composite LRIS rest-frame UV spectra for the sample of 18 multiple-peaked objects and for a sample of 29 galaxies from Steidel et al. (2010) with single-peaked Lyα emission profiles and precisely measured systemic redshifts based on NIRSPEC observations of Hα. To create the composite spectrum I utilized the `IRAF` routine, `scombine`, computing the average of the rest-frame spectra at each wavelength with a minimum/maximum pixel rejection. The composite spectrum was then continuum normalized using a cubic spline fitting function. The Lyα profile in the composite spectrum of the sample is characterized by two clear peaks, with a stronger peak on the red side. This profile is expected since the majority of the profiles resemble such a configuration (i.e., Group I). For the single-peaked composite spectrum, the measured line widths of the interstellar absorption lines are systematically larger than those in the multiple-peaked composite spectrum, with $\langle \sigma_{abs} \rangle = 140 \pm 26$ km s^{-1} for the multiple-peaked composite and $\langle \sigma_{abs} \rangle = 220 \pm 19$ km s^{-1} for the single-peaked composite. The line widths, $\langle \sigma_{abs} \rangle$, were calculated from the averaged Si IIλ1260 and C IIλ1334 lines, which were chosen because of their higher S/N. A Monte Carlo approach, similar to the one described in Section 2.3.3, was used to estimate the error. This difference in interstellar absorption line widths may indicate that the range of velocities found within the interstellar gas must be narrower in order to create a multiple-peaked profile instead of a single-peaked profile.

A comparison of Lyα emission profiles indicates that the centroid of the Lyα emission peak in the single-peaked composite is the same as the centroid of the redder peak in the multiple-peaked composite spectrum. Figure 2.11 illustrates the differences between the total and Group I composite spectra from the sample and the stack of the 29 single-peaked Lyα emission objects from Steidel et al. (2010). I note here that only two out of the 29 single-peaked spectra included in the single-peaked composite were taken with the 600-line grism, while 600-line spectra comprise 5 out of 18 in the multiple-peaked composite. To determine if a possible second peak was missed in the single-peaked composite due to decreased resolution, I smoothed the multiple-peaked composite to the resolution of the single-peaked composite. The second peak in the multiple-peaked composite is still distinctly evident after smoothing, demonstrating that the observed multiple-peaked phenomenon is not simply a result of better resolution. Also of note is the fact that the redshift distribution for the multiple-peaked spectra is bimodal (with objects at $z \sim 2.1 - 2.6$ and $z \sim 3.0 - 3.3$) and characterized by a mean value of $\langle z \rangle = 2.67 \pm 0.42$, with a median of $z = 2.54$. The redshift distribution for the single-peaked spectra has $\langle z \rangle = 2.31 \pm 0.13$, with a median of $z = 2.31$. To control for any possible effects of redshift evolution, I also compare the subset of $z \sim 2$ objects with the single-peaked spectra, and find the same spectral trends.

Finally, the interstellar absorption line kinematics allow for the consideration of the possibility of an alternate scenario for a multiple-peaked Lyα emission profile. The multiple-peaked nature of Lyα emission can also be explained in terms of the interpeak trough tracing absorption from neutral HI with the same kinematics as the material giving rise to the interstellar metal absorption lines. According to this scenario, the trough and the interstellar absorption centroids would be aligned in velocity space. Figure 2.5 shows that, with the possible exception of Q1549-BX202 and Q0449-BX167, the Lyα trough velocity centroid does not line up with the interstellar absorption centroid for any of the objects in the sample with interstellar absorption measurements – ruling out this possible hypothesis.

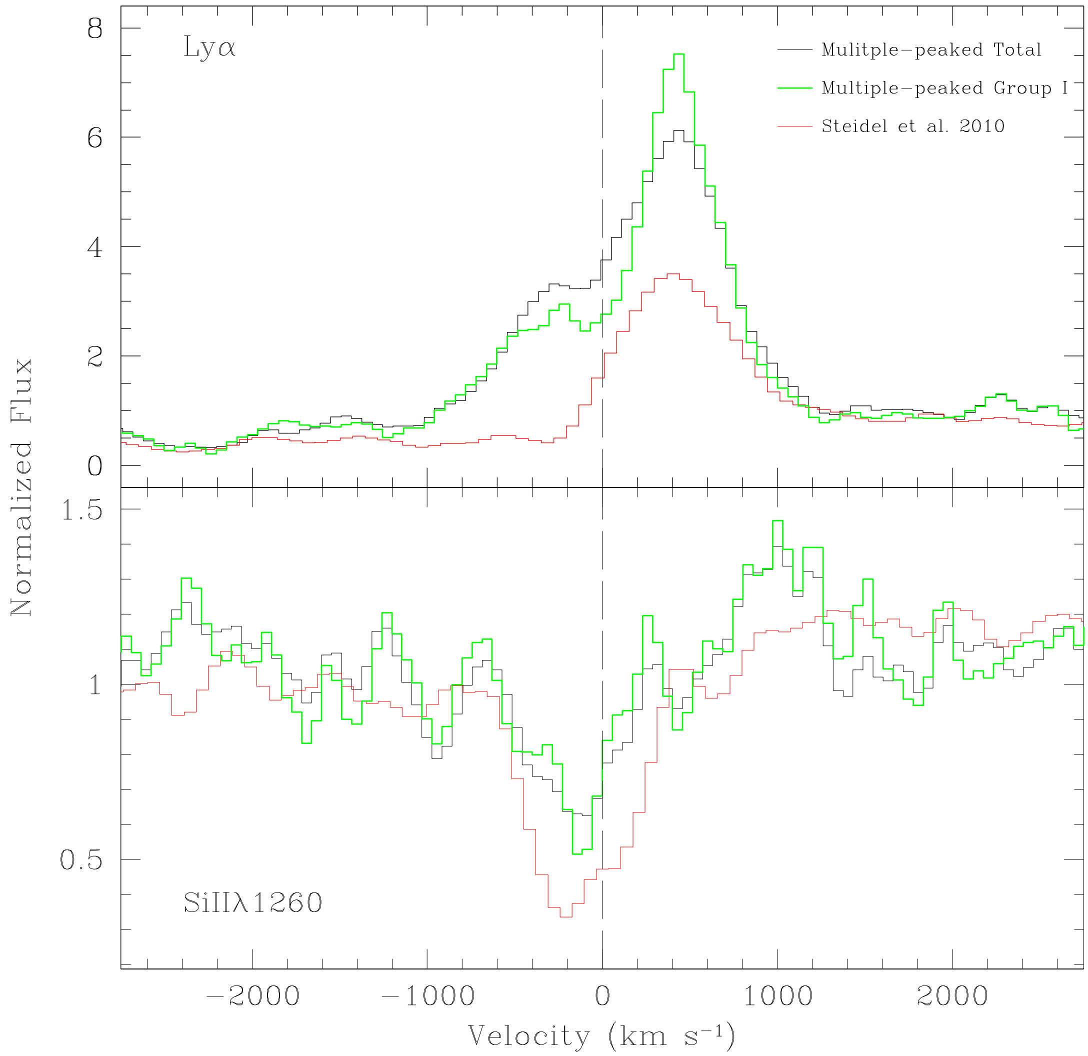

Figure 2.11 Comparison of velocity profiles for the composite of the 18 multiple-peaked objects with NIRSPEC measurements, the subset of 11 objects that comprise Group I, and 29 single-peaked spectra from Steidel et al. (2010). (Top) The Lyα velocity profile for each composite spectrum. The emission centroid from the single-peaked composite spectrum matches the centroid of the red peak from both of the double-peaked composite spectra. (Bottom) The interstellar absorption velocity profile of Si IIλ1260 for each composite spectrum. The line widths for the single-peaked profile ($\langle\sigma_{abs}\rangle = 220 \pm 19$ km s^{-1}) are systematically larger than for the multiple-peaked profile ($\langle\sigma_{abs}\rangle = 140 \pm 26$ km s^{-1}). The line width for the Group I composite is $\langle\sigma_{abs}\rangle = 100 \pm 31$ km s^{-1}. The interstellar absorption lines are also inherently deeper for the single-peaked compared to the multiple-peaked composite.

2.6 Lyα Radiative Transfer Modeling

2.6.1 Models

Explaining the emergent profile of Lyα emission in star-forming galaxies has been the subject of many theoretical and observational studies because of the easy observability of the Lyα line and the complex processes that govern how it emerges from galaxies. Models for the propagation and escape of Lyα photons have been based on both Monte Carlo radiative transfer and simple analytic calculations for a variety of idealized gas density and velocity distributions (Hansen & Oh 2006; Steidel et al. 2010; Verhamme et al. 2006, 2008) as well as post-processing of 3D cosmological hydrodynamical simulations (Laursen et al. 2009a; Barnes et al. 2011). For analytic models, the gas density and velocity distributions assumed include static, expanding, and infalling shells with both unity and non-unity covering fraction, expanding and infalling uniform-density haloes in which the gas velocity depends monotonically on galactocentric distance, open-ended tubes, and spherical distributions of discrete clouds with a range of velocity profiles. In some of these models, the effect of dust extinction has been treated explicitly (Verhamme et al. 2006, 2008; Hansen & Oh 2006; Laursen et al. 2009b).

One of the simple models that has been most closely compared with individual LBG spectra is that of an expanding shell of gaseous material (Verhamme et al. 2006, 2008; Schaerer & Verhamme 2008). In this picture, energy from supernova explosions sweeps up the ISM of star-forming galaxies into a geometrically thin but optically thick spherical shell. With the advent of efficient algorithms to perform resonant-line radiative transfer, it has been shown that such a system can be made to reproduce the observed Lyα profiles of high-redshift galaxies (Verhamme et al. 2006, 2008). Verhamme et al. (2006) deconstruct the Lyα line morphology in order to determine how specific features in the Lyα profile can be related to physical parameters of model systems as well as specific photon trajectories. For example, a shell expanding with uniform velocity V_{exp} will produce a primary redshifted peak at approximately $v = 2V_{exp}$ corresponding to photons that have undergone a single backscattering event en route to the observer. Photons that undergo zero backscatterings emerge in an asymmetric double-peaked structure centered about a velocity $v = -V_{exp}$. Finally, photons that experience multiple backscattering events emerge redward of the primary peak. At fixed expansion velocity, the red-side peaks become indistinguishable from one another and the blue-side peak becomes more blueshifted as the Doppler parameter, b, increases. Increasing the column density but keeping the expansion velocity and thermal velocity fixed results in an enhanced inter-peak separation and broader peaks. Verhamme et al. (2006) also consider the effect of dust attenuation on the emergent Lyα profile, showing how it can reduce the overall Lyα escape fraction, as well as modulate the shape of the profile in velocity space.

2.6.2 Comparison Between Models And Observations

In order to investigate whether such a system can reproduce the data presented here, I used the radiative transfer code developed in Zheng & Miralda-Escudé (2002) and Kollmeier et al. (2010) to generate the observed Lyα spectra emerging from expanding/infalling shell models similar to those presented in Verhamme et al. (2006), with a range of shell column densities, expansion velocities and Doppler parameters. Figure 2.12 shows a subset of such models, for a central monochromatic source of Lyα photons propagating outward through an expanding shell with a column density of $N_{HI} = 2 \times 10^{20}$ cm^{-2}, expansion velocities of $V_{exp} = 100$, 300, and 400 km s^{-1}, and Doppler b-parameters of 40, 80, 120, and

250 km s^{-1}. It should be noted that the Lyα radiative transfer calculation does not depend on the exact physical dimensions of the system for a given column density, expansion velocity, and Doppler parameter as long as the shell is kept geometrically thin. The models have been smoothed to the typical resolution of the LRIS data, for a fair comparison with the observations. Future modeling (Kollmeier et al., in prep.) will include a distribution of injection frequencies for Lyα photons that matches the nebular velocity dispersions measured from Hα and [O III], as well as a more extensive set of gas density and velocity distributions for radiative transfer calculations.

By far the most common Lyα profile observed within the NIRSPEC multiple-peaked sample is the "Group I" type, with two peaks straddling the velocity-field zeropoint, and a stronger red-side peak. Given the frequency of this profile type, it is of particular interest to compare it with Lyα radiative transfer models. In addition to the Lyα emission properties, I mention here that the typical low-ionization interstellar absorption blueshift for Group I objects is slightly smaller than the sample average, with $\langle \Delta v_{abs} \rangle_{\rm Group\ I} = -90$ km s^{-1} (based on the 7 out of 11 Group I objects with interstellar absorption line measurements). The average low-ionization interstellar absorption line width for Group I objects is $\langle \sigma_{abs} \rangle \sim 160$ km s^{-1}, corresponding to $b = 226$ km s^{-1}, if the line width is interpreted as the thermal velocity of a single expanding component of gas (which may indeed not be the correct interpretation of the interstellar absorption profiles, see, e.g., Steidel et al. 2010, and Section 2.6.3).

As seen in Figure 2.12, the best match with the typical Group I profile is obtained using the $N_{HI} = 2 \times 10^{20}$ cm^{-2}, $V_{exp} = 100$ km s^{-1}, $b = 40$ km s^{-1} model. In this model, which also features two peaks straddling the velocity-field zeropoint and a stronger red peak, the blue peak appears at $\Delta v = -370$ km s^{-1},

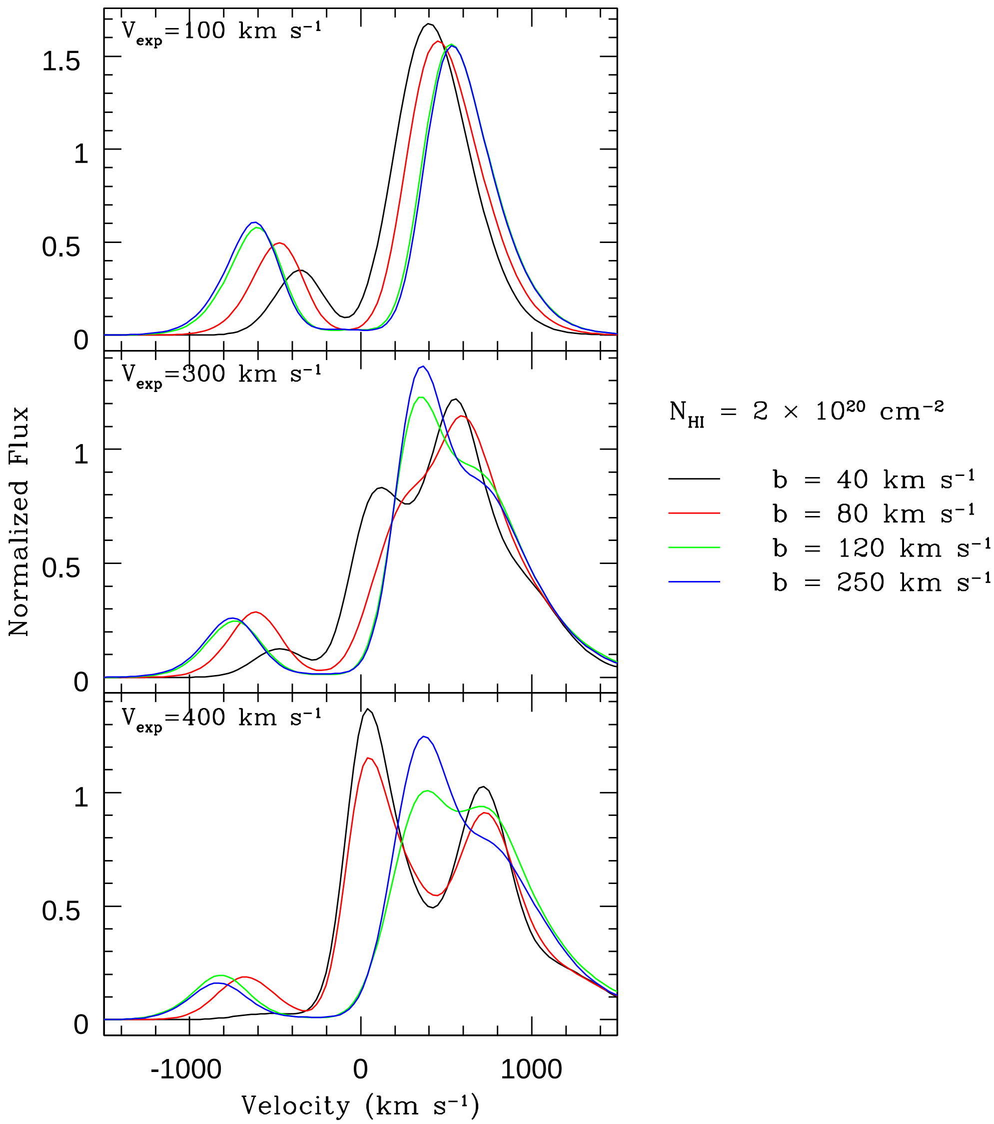

Figure 2.12 Emergent Lyα profiles from an expanding shell with a central monochromatic source. In all panels, the hydrogen column density of the expanding shell is $N_{HI} = 2 \times 10^{20}$ cm^{-2}. The top, middle, and bottom panels show the emergent profiles for shells with expansion velocities of, respectively, V_{exp} =100, 300, and 400 km s^{-1}. In each panel, black, red, green, and blue curves respectively indicate profiles for Doppler parameters of b =40, 80, 120, and 250 km s^{-1}. Each predicted model curve has been smoothed to the typical resolution of the LRIS spectra.

while the red peak appears at $\Delta v = +430$ km s^{-1}. The model matches the average Group I properties both in terms of the locations of the Lyα peaks relative to zero, as well as the interpeak separation, although the predicted contrast between the red and blue peak heights is too large. At the same time, the predicted absorption profile for such an expanding shell (which should be traced well by the low-ionization features arising in neutral hydrogen gas) would have $\langle \sigma_{abs} \rangle \sim b/\sqrt{2} \sim 30$ km s^{-1}, i.e., *significantly* lower than what is observed for Group I objects. This difference represents a fundamental discrepancy between the shell model and the full complement of Group I data – even if the average Lyα emission profile can be roughly reproduced.

Figure 2.13 shows the $N_{HI} = 2 \times 10^{20}$ cm^{-2}, $V_{\rm exp} = 100$ km s^{-1}, $b = 40$ km s^{-1} model, along with other $V_{exp} = 100$ km s^{-1} expanding shell models with smaller column density (i.e., $N_{HI} = 1 \times 10^{17}$ cm^{-2} or $N_{HI} = 1 \times 10^{19}$ cm^{-2}) and larger Doppler parameters ($b \geq 120$ km s^{-1}). Overplotted on each panel is the continuum-subtracted composite spectrum from Group I, which has been normalized to the primary peak height of each model. The models with the smaller column density also predict emergent profiles with two peaks straddling the velocity zeropoint and a stronger red-side peak. However, in comparison to the Group I composite spectrum, the smallest column density model features a peak velocity separation that is too small ($\Delta v = 640$ km s^{-1}), and, in both lower column density cases, the emission peaks themselves are too narrow. An important limitation in this analysis is the oversimplification of comparing a model characterized by a specific set of physical parameters with a composite spectrum. While the composite spectrum offers a boost in S/N relative to an individual spectrum, it also includes the spectra of many individual galaxies that likely span a range of parameters (e.g., $N_{HI}, b, V_{\rm exp}$).

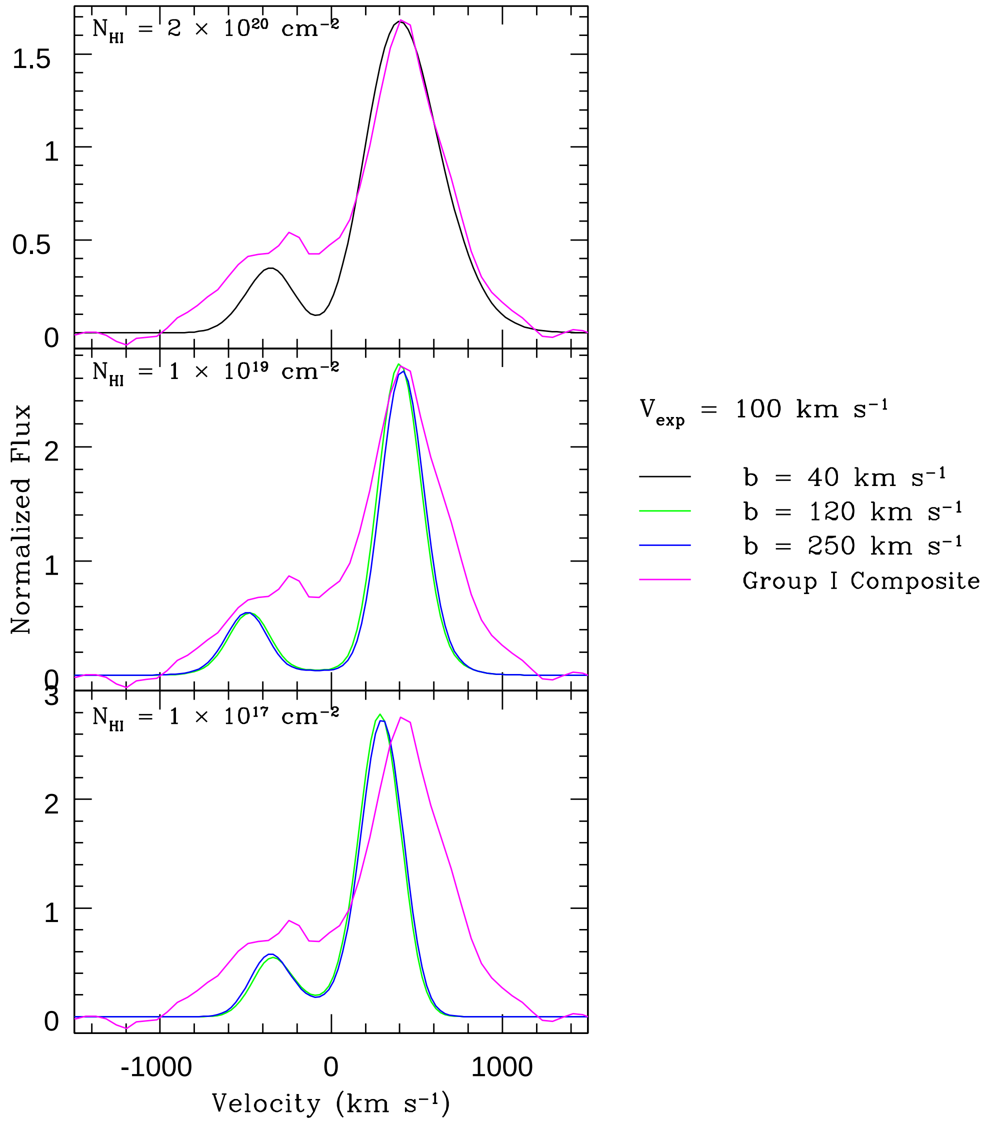

Figure 2.13 Emergent Lyα profiles from simple shell models that are qualitatively similar to Group I spectra. All panels show the predicted profiles for a central monochromatic source passing through an expanding shell with V_{exp} =100 km s^{-1}. The top panel features a model with $N_{HI} = 2\times10^{20}$ cm^{-2} and Doppler parameter b = 40 km s^{-1}. The middle and bottom panels show the results for models with $N_{HI} = 1 \times 10^{19}$ cm^{-2} and $N_{HI} = 1 \times 10^{17}$ cm^{-2}, respectively. In both of these panels, the predicted profiles are shown for Doppler parameters b = 120 and 250 km s^{-1}. Overplotted on each panel is the Group I continuum-subtracted composite spectrum. The Group I spectrum was normalized to match the primary peak height of each model. The $N_{HI} = 2 \times 10^{20}$ cm^{-2} model has the closest resemblance to the typical properties of the Group I Lyα spectra in terms of both precise peak locations and line widths.

The Lyα profiles for objects in Group II are also characterized by two peaks straddling the velocity-field zeropoint, but with a stronger blue peak. A double-peaked profile with a dominant blue peak represents a key signature of infalling gas (Zheng & Miralda-Escudé 2002; Dijkstra et al. 2006; Verhamme et al. 2006; Barnes et al. 2011). In terms of the shell models presented in Figure 2.12, the predicted Lyα profile for an infalling shell of material with a specific column density and Doppler parameter can be derived by simply flipping the corresponding expanding-shell model about the line $\Delta v = 0$. As shown in Verhamme et al. (2006) and Dijkstra et al. (2006), infalling spherical haloes of gas will also yield double-peaked profiles with a stronger blue peak, assuming either uniform emissivity or a central point source. The lack of significant blueshift in the observed low-ionization interstellar absorption lines of Group II objects (with Q1549-C20 actually showing a slight redshift) lends additional support to a model of infalling gas. In detail, however, there are mismatches between the particular infall models mentioned above and the observed Group II spectra. The average peak separation for the Group II objects is $\langle \Delta v_{peak} \rangle \sim 800$ km s^{-1}, with the blueshifted peak located at $\Delta v \sim -200$ km s^{-1}. The infalling halo model of Verhamme et al. (2006) predicts a peak separation of only $\langle \Delta v_{peak} \rangle \sim 460$ km s^{-1}, which is significantly smaller than the observed one (see their Figure 5). While an infalling shell model with $V_{infall} = 100$ km s^{-1} and $b = 40$ km s^{-1} produces roughly the correct peak separation and stronger blue peak, the locations of the blue and red peaks in the infalling shell model relative to zero velocity do not match those of the observed Group II spectra.

Like the spectra in Group II, Group III spectra also exhibit a stronger blue peak in the Lyα profile, but both blue and red peaks are redshifted relative to the velocity-field zeropoint, and most likely trace outflowing rather than inflowing gas. Only one of the two Group III objects (SSA22a-C49) has measurable low-ionization interstellar absorption. From these features, I measure a significant blueshift of $\Delta v \sim -230$ km s^{-1}, and a line width of $\sigma_{abs} \sim 230$ km s^{-1}. In terms of the simple shell models shown in Figure 2.12, the closest match to Group III is found for $V_{exp} = 400$ km s^{-1}, and $b = 40$ km s^{-1}. As discussed by Yang et al. (2011), the blueshifted peak in a shell model decreases in strength as V_{exp}/b increases. This trend is reflected in the large V_{exp}/b model discussed here, with its lack of significant flux bluewards of zero, and two peaks redshifted relative to zero. Although there is qualitative agreement between the model and Group III spectra, in so far as both have two peaks redshifted relative to zero, and no significant flux bluewards of zero, the actual peak separations and locations in the model and data do not agree in detail. The model predicts $\Delta v_{peak} \sim 600$ km s^{-1}, while the Group III objects have $\Delta v_{peak} \sim 400$ km s^{-1}. Furthermore, the blue peak in the model is shifted by only $\sim +100$ km s^{-1} relative to zero, while the blue peak in SSA22a-C49 is shifted by $> +500$ km s^{-1} relative to zero. Finally, the relatively small Doppler parameter of $b = 40$ km s^{-1} would give rise to significantly narrower low-ionization interstellar absorption line widths than those observed. While Group III objects most likely indicate the presence of an outflow, the models described here still present some mismatches with the Group III data.

Distinguishing between Group II and Group III objects by establishing the velocity-field zeropoint has potentially important consequences. Over the last several years, the process of galaxy growth through cold gas accretion has received much attention in the theoretical literature. Both analytic calculations (Birnboim & Dekel 2003) and numerical simulations (Fardal et al. 2001; Kereš et al. 2005, 2009; Dekel et al. 2009) suggest that high-redshift galaxies primarily grow by smoothly accreting cold gas from the surrounding IGM. Identifying observational signatures of infalling gas is crucial for testing the theoretical paradigm of cold accretion. In particular, since the predicted signatures of accreting gas in low-ionization metal absorption lines are so weak, due to the low metallicity of infalling material (Fumagalli et al. 2011), the Lyα feature may represent the best hope for detecting cosmological infall. Beyond the Group II and Group III objects in the NIRSPEC sample, $\sim$ 30% of the double-peaked spectra in the LRIS parent sample have a stronger blue peak. If the velocity-field zeropoint can be established in these objects, to test whether the stronger blue peak is also blueshifted relative to zero (i.e., distinguishing between Group II and Group III spectra), their Lyα spectra may provide evidence for and constraints on the nature of gas infall in star-forming galaxies at $z \sim 2-3$.

For the remaining three spectra (Groups IV and V), no qualitative matches were found among the simple models presented here. Indeed, for SSA22a-D17 and SSA22a-C31 (Group IV), there are two peaks with roughly equal heights, as seen in a static configuration. However, the locations of the peaks are not symmetrically distributed around the velocity-field zeropoint, as would be expected for a static shell, and the interpeak trough is redshifted by several hundred km s^{-1}. Furthermore, SSA22a-D17 has an extremely large low-ionization interstellar absorption blueshift measured, with $\Delta v \sim -1170$ km s^{-1}, which additionally rules out the static case. Q1623-BX129 has two strong peaks with roughly equal heights and similar locations to those of SSA22a-D17 and SSA22a-C31, plus a third, redder peak, which is significantly weaker. A larger model parameter space will be required to match the profile shapes of these three objects.

In summary, while general qualitative matches can be found for the Group I, Group II, and Group III Lyα profile types, I find notable specific discrepancies between the models and the totality of the data presented here – with particular attention to the interstellar absorption profiles. One important issue is that the shell models that provide the best matches to, e.g., Group I profiles ($V_{exp} = 100$ km s^{-1}, $b = 40$ km s^{-1}), are not able to match simultaneously the broad low-ionization interstellar absorption troughs characterized by a median of $\sigma_{abs,med} \sim 190$ km s^{-1}. I also highlight the importance of these new NIRSPEC measurements for untangling the nature of these Lyα spectra. Measurements of the velocity-field zeropoint (i.e. from the Hα or [O III] redshift) are key for distinguishing between Group II (inflow) and Group III (strong outflow) objects. Furthermore, determining the velocity width of the input Lyα spectrum (based on the Hα or [O III] velocity dispersion), so that it is not a free parameter of Lyα radiative transfer models, reduces the degeneracies associated with fitting physical models to Lyα profiles. Indeed, when fitting the double-peaked Lyα profile for an object with unconstrained systemic velocity and input Lyα velocity dispersion, Verhamme et al. (2008) find two expanding-shell model solutions that differ by 5 orders of magnitude in inferred hydrogen column density (see their Figure 8). One of the best-fit models has an inferred intrinsic Lyα FWHM$=700$ km s^{-1} – a factor of three larger than the average for the sample! Furthermore, the placement of the velocity-field zeropoint differs by ~ 500 km s^{-1} for the two best-fit models in question. Verhamme et al. (2008) conclude that neither solution is satisfactory and that future observations are needed to constrain their models. With systemic redshift and velocity dispersion measurements, such degeneracy in best-fit models is no longer allowed, potentially leading to much tighter constraints on the underlying physical picture.

2.6.3 Additional Considerations And Caveats

In the preceding discussion, within the framework of expanding/infalling shell models, I presented an interpretation of the observed low-ionization interstellar absorption line widths in terms of the random thermal broadening of gas in the shell. An alternative explanation of interstellar absorption line widths is presented in Steidel et al. (2010), according to which absorption is produced by a population of discreet clouds at a large range of galactocentric radii (i.e., not a thin shell). The expansion velocities of these clouds increase smoothly and monotonically with increasing radius, and their covering fraction is a decreasing function of radius. In such a model, in which photons scatter off of the $\tau_{Ly\alpha} = 1$ surfaces of discrete clouds, the nature of the bulk gas kinematics modulates the emergent Lyα profiles, as opposed to the neutral hydrogen column density and Doppler b-parameter of individual clouds. This clumpy outflow model accounts for the typical interstellar absorption profiles both along the line of sight to individual UV-selected star-forming galaxies at $z \sim 2-3$, as well as along averaged offset sightlines with impact parameters up to ~ 100 physical kpc, and predicts extended Lyα emission consistent with the observations (Steidel et al. 2011).

At the same time, high-resolution 3D cosmological hydrodynamical simulations that follow the radiative transfer of Lyα photons through the gas distributions surrounding high-redshift galaxies are highlighting the importance of orientation effects. The gas column density and velocity distributions in these simulated galaxies are anisotropic and irregular, characterized by clumps and filaments of infalling and outflowing cold gas (Laursen et al. 2009a; Barnes et al. 2011). This anisotropy leads to a strong dependence of the shape of the emergent Lyα profile on viewing angle. For example, if the line of sight to a galaxy intercepts a filament of infalling gas, a blue-asymmetric peak may be observed, even in the presence of outflowing gas in the system (Barnes et al. 2011). A close comparison is required between the predictions of such simulations and the full ensemble of Lyα profiles observed in LBGs, as well as incorporating detailed Lyα radiative transfer calculations from Zheng & Miralda-Escudé (2002) and Kollmeier et al.

(2010) into the clumpy outflow model of Steidel et al. (2010).

Another potentially important effect to consider is absorption by the IGM (Dijkstra et al. 2007; Zheng et al. 2010). Recent simulations by Laursen et al. (2011) have demonstrated that the blue peak in an emergent double-peaked Lyα profile may be suppressed due to absorption by neutral hydrogen external to a galaxy. For the purposes of such analysis, "IGM" is defined as gas located at a radius greater than ~ 1.5 times the dark-matter halo virial radius. IGM absorption may be significant even at redshifts well below the epoch of reionization. This result is relevant to the interpretation of the Group I profile types. In such objects, the Lyα peak bluewards of the systemic velocity is weaker than the red peak. I have compared these profiles to simple galactic-scale models for outflowing gas, in which the asymmetry arises due to the radiative transfer of Lyα photons, and have ignored the possible effects of IGM absorption on the observed red-to-blue peak ratio. One simple test for the importance of IGM absorption consists of examining the distribution of red-to-blue peak ratios as a function of redshift within the LRIS double-peaked parent sample. For this test, I divide the sample into high- ($z \sim 3$) and low-redshift ($z \sim 2$) subsamples at a threshold redshift of $z = 2.7$, and calculate the median red-to-blue peak ratio for each subsample. If IGM effects are significant, one would expect to see the red-to-blue peak ratio evolve towards lower values at lower redshifts, as the blue peak becomes less suppressed by IGM absorption (under the assumption that the two samples have the same intrinsic distributions of double-peaked Lyα profile shapes before being subject to IGM absorption). In fact, I find that the median red-to-blue peak flux ratios for $z \sim 3$ and $z \sim 2$ subsamples are 1.3 and 1.5, respectively, and not statistically distinguishable. Therefore, IGM absorption does not appear to have a significant impact on the observed multiple-peaked Lyα profile shapes in the sample.

Finally, I must admit the possibility of an entirely different explanation for the origin of multiple-peaked Lyα emission profiles, such as galaxy mergers. A multiple-peaked profile would naturally result from a system in a merger state, with different peaks corresponding to different merging components (Cooke et al. 2010; Rauch et al. 2011). The continuum and emission-line morphology of objects in the sample are crucial to consider when examining possible merger models. Figure 2.1 shows the (seeing-limited) $\mathcal{R}$-band morphologies for objects in the sample. The majority of the targets appear to be consistent with single components at this resolution. A small number of objects, however, are slightly extended (e.g. Q2206-BX151, Q1549-M22) or appear to have multiple components (e.g. Q0449-BX167, Westphal-BX154). Three of these objects have already been discussed in Section 2.3.1.1 in terms of their complex two-dimensional spectra. If the multiple-peaked Lyα profiles were simply caused by mergers, there should be evidence of multiple-peaked emission in the rest-frame optical nebular lines (i.e., Hα and [O III]λ5007). These features more closely trace the systemic velocity and dynamics and are typically not as sensitive to bulk outflow motions as the Lyα emission line. As described in Section 2.3.1.1, only Q1549-M22 shows possible signs of nebular lines with multiple-peaked behavior in the spectral direction, ruling out mergers as a possible explanation for the majority of these Lyα profiles.

2.7 Summary And Discussion

There is strong observational evidence for the ubiquity of large-scale outflows in high-redshift star-forming galaxies. Gauging the overall impact of these large-scale outflows on the evolution of the galaxies sustaining them remains an open challenge. Theoretical considerations suggest that, at the same cosmic epochs, the *inflow* of cold gas is also a very important process in the evolution of star-forming galaxies. Multiple-peaked Lyα profiles in star-forming UV-selected galaxies at $z \sim 2-3$ offer a unique probe of both outflows and inflows in the early universe. The complex line structure potentially provides constraints on many important gas flow parameters. Specifically, the locations of peaks with respect to the velocity-field zeropoint, their separations, and flux ratios are all additional pieces of information not seen in single-peaked Lyα profiles. Along with observational data such as accurate systemic redshifts, intrinsic nebular line widths, and intrinsic ionizing photon fluxes, one can distinguish among the possible processes underlying these systems.

I have shown that the phenomenon of multiple-peaked profiles appears in a significant fraction ($\sim 30\%$) of UV-selected star-forming galaxies at $z \sim 2-3$ with Lyα emission. After identifying possible candidates for this study, I presented a sample of 18 multiple-peaked objects with observed Hα or [O III]λ5007 nebular emission lines, which were used to establish accurate systemic redshift measurements. The average velocity dispersion, σ_v, and the mean star-formation rate in the sample are comparable to values measured from the full population of UV-selected star-forming galaxies at $z \sim 2-3$. At the same time, given the focus on Lyα-emitting galaxies, the average $E(B-V)$ in the sample is bluer than what is typically measured. Detected interstellar absorption lines for objects in the sample show, on average, a blueshift, which is suggestive of large-scale outflows driven by supernovae or winds of massive stars. Additionally, the interstellar absorption line widths are measured to be $\langle\sigma_{abs}\rangle \sim 200$ km s^{-1}, which is similar to values found in other studies of star-forming galaxies at $z \sim 2-3$. A comparison of the interstellar absorption line widths to a sample of star-forming galaxies with single-peaked Lyα emission show the single-peaked objects to have consistently larger interstellar absorption line widths. The difference in interstellar absorption line widths may signify that the ranges of gas velocities are different for multiple-peaked compared to single-peaked Lyα emission objects.

I have qualitatively compared the observed Lyα profiles with simple models of expanding and infalling gaseous shells and halos, given the attention such models have recently received in the literature (Verhamme et al. 2006, 2008; Schaerer & Verhamme 2008). The closest match between these simple models and these data is found for Group I type profiles, which make up 11 out of 18 of the NIRSPEC sample objects, and are characterized by a red-asymmetric double peak straddling the velocity-field zeropoint. Group I type profiles can be produced in an expanding shell model, with a high-column density ($N = 2 \times 10^{20}$ cm^{-2}), moderate expansion speed ($V_{exp} = 100$ km s^{-1}), and small Doppler parameter, ($b = 40$ km s^{-1}). At the same time, the observed low-ionization interstellar absorption line profiles for Group I objects are significantly broader than the features that would arise from an expanding shell with $b = 40$ km s^{-1}, and signal a problem with the above interpretation for the Group I Lyα spectra. Certain aspects of Group II and Group III Lyα spectra are also reproduced by the simple models considered here, though, in detail, the matches are not perfect. For the remaining handful of objects in the NIRSPEC multiple-peaked sample, the suite of models considered here cannot be used to explain the observed profiles, both in terms of Lyα peak locations, relative strengths, and numbers.

It is also of interest to compare Lyα radiative transfer models with high-redshift data of significantly higher S/N and resolution than the spectra presented here. Quider et al. (2009) present the multiple-peaked Lyα emission profile of the strongly gravitationally lensed galaxy, "the Cosmic Horseshoe", for which the magnification is estimated to be a factor of ~ 24. The Cosmic Horseshoe has a very well-defined stellar systemic redshift, from which the Lyα spectral profile can be calculated in velocity space. While an expanding shell model from Verhamme et al. (2006) with $N_{HI} = 7 \times 10^{19}$ cm^{-2}, $V_{exp} = 300$ km s^{-1}, and $b = 40$ km s^{-1}, provides a qualitative match to the two redshifted peaks in the Cosmic Horseshoe Lyα profile, the small Doppler b-parameter in the model is again at odds with the broad low-ionization interstellar absorption profile. Furthermore, in detail, the locations of the Lyα peaks in the predicted model spectrum do not line up with those of the observations. Both typical and strongly-lensed UV-selected star-forming galaxies with well-determined systemic redshifts and, accordingly, Lyα profiles calculated robustly in velocity space are now providing important observational constraints on Lyα radiative transfer models. These objects highlight the need for considering simultaneously the emergent Lyα emission profile, and the profile of low-ionization interstellar absorption, which must be matched within a unified framework (Steidel et al. 2010).

While I have mainly focused here on the discrepancies between models and data, and have therefore not yet been able to derive the physical parameters of the gaseous flows surrounding UV-selected star-forming galaxies at high redshift, this analysis as an important initial step. It will simply not be possible to constrain the gas density and velocity distributions in these circumgalactic flows without the simultaneous establishment of the location of the multiple-peaked Lyα profile and interstellar absorption features in velocity space. I have presented such measurements here for a sample of objects whose red- and blue-asymmetric multiple-peaked Lyα profiles at least qualitatively suggest a range of processes including both outflows and infall. Additional critical observables presented here which will be considered in future modeling are the input velocity distribution of Lyα photons as traced by the velocity dispersion of either Hα or [O III]λ5007 emission, and the degree of dust attenuation as traced by rest-frame UV colors and Lyα/Hα flux ratios. With a realistic model that successfully matches the combination of intrinsic and emergent Lyα velocity distributions as well as interstellar absorption profiles, an accurate gas density and velocity distribution as a function of radius can be obtained. These distributions will potentially allow the rates at which cold gas mass is flowing in and out of galaxies to be constrained, which represents one of the most important goals in the study of galaxy formation.

CHAPTER 3

Performance Of The HgCdTe Detector For MOSFIRE, An Imager And Multi-Object Spectrometer For Keck Observatory

3.1 Introduction

Near-infrared spectroscopy is crucial for studying the important rest-frame optical emission lines in high-redshift galaxies. These emission lines are used to estimate the physical properties of galaxies, which can lend insight into galaxy formation and evolution. Until recently, only single object near-infrared spectrographs have been available, resulting in a slow build up of samples of high-redshift galaxies with measured rest-frame optical emission lines. The Multi-Object Spectrometer For Infrared Exploration (MOSFIRE) was designed to obtain hundreds of near-infrared spectra spanning a variety of environments and physical conditions, increasing our knowledge of high-redshift galaxy populations. MOSFIRE is a near-IR spectrograph with four atmospheric bands: Y(0.97-1.12μm), J(1.15-1.35μm), H (1.46-1.81μm), or K(1.95-2.39μm). It is located at the Cassegrain focus of the Keck-1 telescope on Mauna Kea, Hawaii. The optical design provides both imaging and multiple-object spectroscopy over a field of view (FOV) of $6.'14 \times 6.'14$ with a resolving power ($\frac{\lambda}{\Delta\lambda}$) of R $\simeq$ 3,500 for a slit width of $0.''7$ (2.9 pixels along the dispersion). A unique feature of MOSFIRE is it's multiplexing capability with the Configurable Slit Unit (CSU). The detector is a sensitive 2K $\times$ 2K H2RG HgCdTe array with a 2.5 μm cut-off. To reach MOSFIRE's desired sensitivity limits which were designed to probe faint high-redshift galaxies, the detector must achieve low noise levels, < 5 e^-. Described here is the testing and analysis of the MOSFIRE detector that I led to fully characterize it's properties to guarantee MOSFIRE could attain it's sensitivity goals. My results have demonstrated that the MOSFIRE detector has very low dark current, low noise, excellent quantum efficiency across our wavelength range and good uniformity. It is also a very flat device, which is important for MOSFIRE's fast camera beam. In addition, the reference pixels have been shown to be effective in eliminating the readout shifts between the 32 outputs. The only intrinsic behavior that may limit performance is charge persistence (residual images) from previous exposures, which is a common issue with the majority of infrared detectors. The MOSFIRE detector is now fully operational.

3.2 MOSFIRE Design

Figure 3.1 shows the design layout for the MOSFIRE instrument. The cryogenic CSU, which has been developed in collaboration with the Swiss Center for Electronics and Micro Technology (CSEM), can create up to 46 slits and is reconfigurable under remote control in less than 6 minutes without any thermal cycling of the instrument. Slits are formed by moving opposing bars from both sides of the focal plane. An individual slit has the length of $7''.0$, but bar positions can be aligned to make longer slits. When the bars are moved apart to their full extent and the grating is changed to a mirror, MOSFIRE becomes a wide-field imager with a fine pixel scale of $0''.18$ per pixel. The Flexure Compensation System (FCS) was designed to achieve the goal of less than 1 pixel residual image

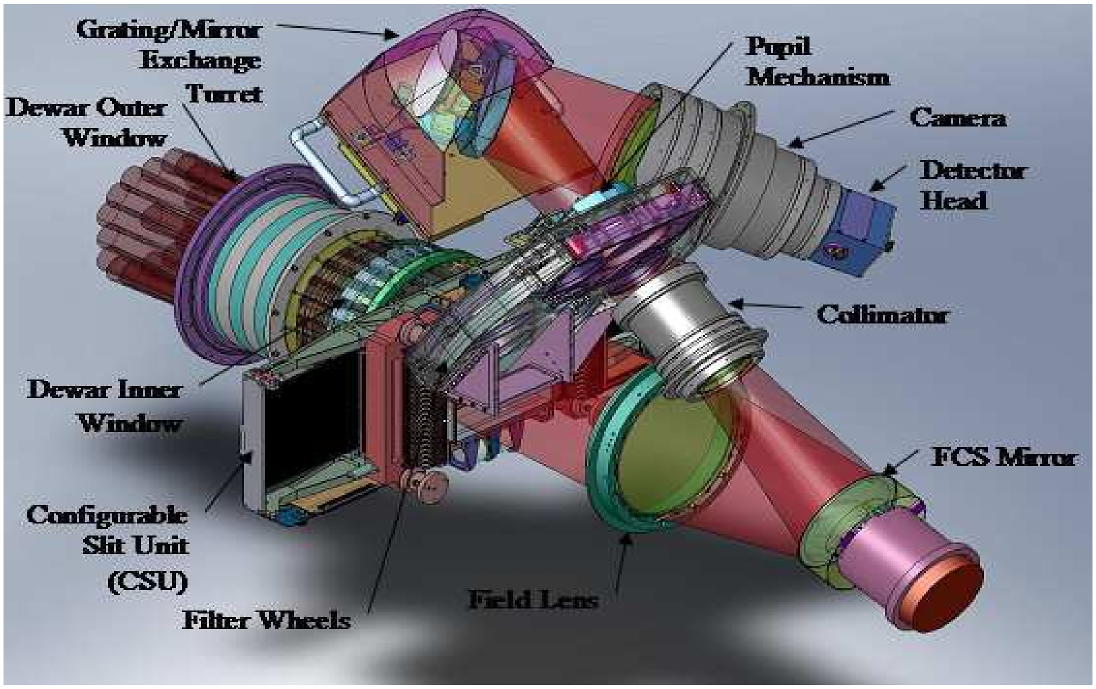

Figure 3.1 The design layout for the MOSFIRE instrument. The majority of this chapter focuses on work completed on the detector head component of the instrument.

motion across the possible gravity orientations at the Cassegrain focus. The FCS uses three pistons behind a tip/tilt mirror to offset any flexure that occurs at different instrument position angle and elevation, thus enabling MOSFIRE to be gravity invariant.

MOSFIREs optical design is predicated on the 18 μm pitch of the Teledyne Hawaii2-RG (**H**gCdTe **A**stronomy **W**ide **A**rea **I**nfrared **I**mager with **2**K x 2K resolution, **R**eference pixels and **G**uide mode; H2RG) detector. The H2RG detector contains a total of 2048×2048 pixels and is made from mercury cadmium telluride (HgCdTe) with a 2.5 μm cut off and the substrate removed to enhance the quantum efficiency at the shorter wavelengths. High quantum efficiency (QE $\geq 65\%$) is required to achieve our instrument throughput goals. The on-sky measured detection rates between OH lines in the darkest parts of the Y, J, H, and K bands are, respectively, 0.3, 0.3, 0.6, 0.4 e^-/s/pixel for a 0$''$.7 slit assuming ∼3 pixels sampling in the dispersion direction (R≃ 3,500) for optimistic conditions. A dark current of <0.03 e^-/s/pixel and an effective read noise below $\sim 5e^-$ would result in background-limited performance for exposures longer than 90 seconds. A typical spectroscopic integration time is 180 seconds in the K band based on the experience of the MOSFIRE team with the OH variability. As stated in the MOSFIRE Design document, the limiting magnitudes (Vega) for a S/N ratio of 10 in 1000 seconds in spectroscopic mode at R≃3500 are J = 20.4, H=20.1, and K = 18.6. To achieve these limits we assume 0.05 e^-/s dark current, an effective read noise of 4 e^-, and the background appropriate for spectral regions between OH lines, evaluated over a 3 pixel resolution element and assuming a 0.5 arcsec^2 extraction aperture. Imaging limits assume a 3×3 pixel (0$''$.54) aperture for a point source under good seeing conditions (McLean et al. 2010).

3.3 The MOSFIRE Detector

When it was selected for MOSFIRE in 2006, the H2RG and the SIDECAR ASIC (**S**ystem for **I**mage **D**igitization **E**nhancement **C**ontrol **A**nd **R**etrieval **A**pplication **S**pecific **I**ntegrated **C**ircuit) were recently developed technology from Teledyne Imaging Sensors. Stimulus for the development for the ASIC came from the James Webb Space Telescope (JWST) due to their need to reduce power and eliminate long cables. It was not known at that time if the ASIC could achieve the kind of low noise performance typical of other controllers. As stated above, we require a very low read noise and dark current to reach our sensitivity goals. Previous generations of infrared detectors have read noise values of ∼ 25 e^- and dark current of ∼ 0.5 e^-/s/pixel. To mitigate the risk and demonstrate that the H2RG and ASIC would meet MOSFIRE's sensitivity requirements, I lead extensive testing of two engineering-grade devices and MOSFIRE's science-grade detector over a period of four years. During this time, we worked closely with Teledyne on several iterations of ASIC hardware and software to achieve the final configuration. The engineering-grade detectors were tested over a duration of approximately two and a half years. The science-grade detector was then tested for an additional one and a half years before MOSFIRE achieved "first light" at Keck.

The HAWAII2-RG is designed to operate in a number of different performance modes. Lowest read noise is achieved with the 100 kHz "slow" data rate, which is MOSFIRE's operation rate. The H2RG detector can be read out with 1, 4 or 32 outputs. The first uses the lowest power, but the latter provides the highest frame rates. Fast readout rates are essential for MOSFIRE's broad-band imaging capabilities. The delivered configuration, and the configuration used for the majority of testing described in this chapter, employed 32 readout channels. With overhead, v2.3 of the HxRG code provided by Teledyne yields a minimum exposure time of 1.45 seconds, or a frame rate of $\sim$0.7 Hz, when using 32 channels. The MOSFIRE detector software supports single, correlated double sample (CDS), multiple-correlated double sample (MCDS), or up-the-ramp (UTR) readout modes. See Section 3.4.4 for a more detailed description of the allowed readout modes.

The MOSFIRE science-grade detector was selected based on a consistent set of tests carried out on multiple devices by Teledyne. The selected device has a quantum efficiency of 0.88 e^-/photon (88%) at 1.0 - 2.4 μm and a measured flatness of 0.00437 mm. A median read noise of 3.45 e^- rms was achieved using 32 Fowler pairs in Teledyne's test set up. All of Teledyne's testing, however, was conducted with a standard controller and not the ASIC. Therefore the ASIC's performance with the H2RG had never been verified. The primary goals for this project were three-fold:

1. To demonstrate the correct operation of the MOSFIRE detector at cryogenic temperature while using the newly-developed SIDECAR ASIC.
2. To determine or verify the properties of the MOSFIRE detector prior to installation into the final instrument. In particular, it is very important to determine the ultimate noise performance. MOSFIRE's goal is < 5 electrons rms. Detector performance will be related to the science goals of the MOSFIRE project.
3. To verify the correct operation of the final detector system, including the focus control mechanism and temperature stabilization circuit. This includes the installation of the detector system into the instrument and the confirmation of the correct operation of the detector after MOSFIRE was delivered to Keck Observatory.

Teledyne offers H2RG devices with an ASIC that implements all of the detector readout functions (see Figure 3.2). The ASIC provides clocks and bias voltages to the detector and digitizes the detector outputs. The SIDECAR ASIC is packaged separately on a small board that is located inside the dewar next to the detector head. The ASIC provides a selection of gain settings and 16-bit digitization so that the signals leaving the dewar are already in digital form. No external amplifiers, level shifters or Analog-to-Digital Converters (ADC) are required. Weight and power are significantly reduced compared to standard controllers. In addition, since the ASIC is located directly next to the detector, the

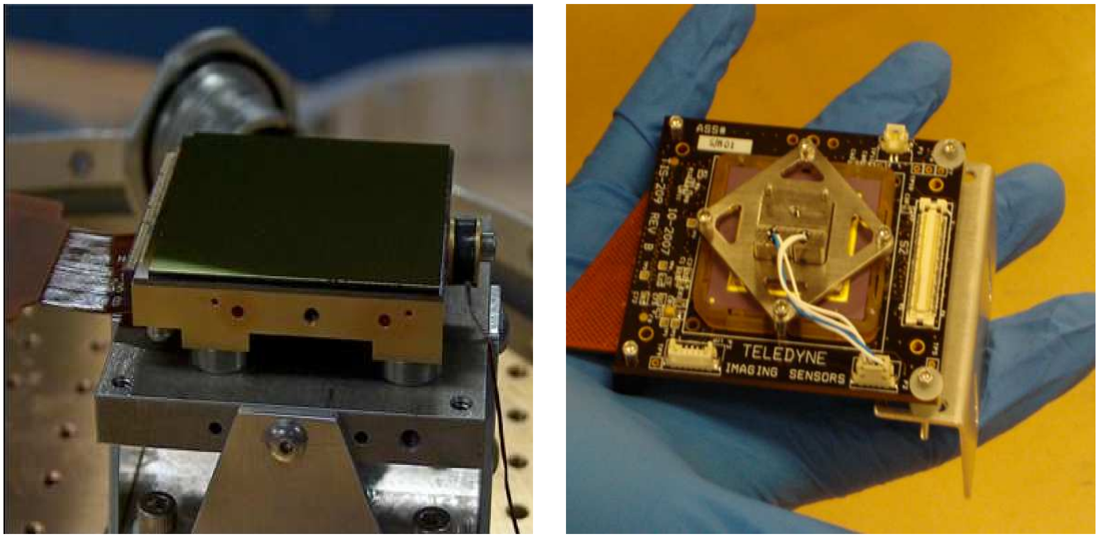

Figure 3.2 (Left) One of the engineering-grade detectors in the test dewar. (Right) The ASIC electronics is shown next to a person's hand to demonstrate the compactness of the readout system. This small size allows the ASIC to be adjacent to the detector and to operate at the same temperature as the rest of the instrument, which is 120 K (-244 °F).

signal is almost immediately converted from analog to digital. Previous generations of controllers would require the analog signal to travel through a long cable, increasing the chance of electrical interference disrupting the signal. In MOSFIRE, the ASIC cryogenic board is at the same temperature as the bulkhead or optical bench (120 K). Just outside the dewar wall is the JADE 2 (**J**WST **A**SIC **D**rive **E**lectronics 2) board, which provides the interface between the ASIC and the USB 2.0 connection.

3.4 Lab Results

Numerous tests were carried out on engineering-grade detectors and our science-grade device to develop our Detector Server software, establish that the ASIC meets our requirements, and characterize the performance before MOSFIRE was installed on the Keck-I telescope. Many properties were tested in several configurations to discover the best operating setup for MOSFIRE's specific science goals. There were three different lab configurations that the MOSFIRE detectors were tested in. The first configuration consisted of a small test dewar located at the UCLA Infrared Lab, which was used for preliminary assessment of the detector, ASIC, and JADE 2. After extensive testing was completed inside of the test dewar, the detector was then installed into the MOSFIRE detector head and the entire module, including a field-flattening lens and detector focus mechanism was cooled and evaluated inside of a larger test dewar. The final configuration for testing was completed inside of the fully-integrated MOSFIRE instrument before it was delivered to Keck Observatory.

3.4.1 32-Channel Readout

MOSFIRE's imaging capability requires the use of the 32-channel readout configuration to enable a fast readout time. Every channel is read out from a different amplifier, each of which has a small offset bias that changes from readout to readout. To compensate for the fluctuations in each channel, Teledyne incorporated reference pixels (the R in H2RG) in a 4 pixel boarder around the detector. These pixels, which are not sensitive to light, track the amplifier offsets. The reference pixels at the top and bottom of each channel (4×64 pixels each) can be used to resolve the offset issue. I have created a simple algorithm that takes the median value of the top and bottom reference pixels in each channel and then subtracts that median value from each pixel in the respective channel. This algorithm has been implemented into the detector server so that the offsets are rectified before the final image is read out. Figure 3.3 demonstrates how channel-to-channel variation can be rectified with the use of reference pixels.

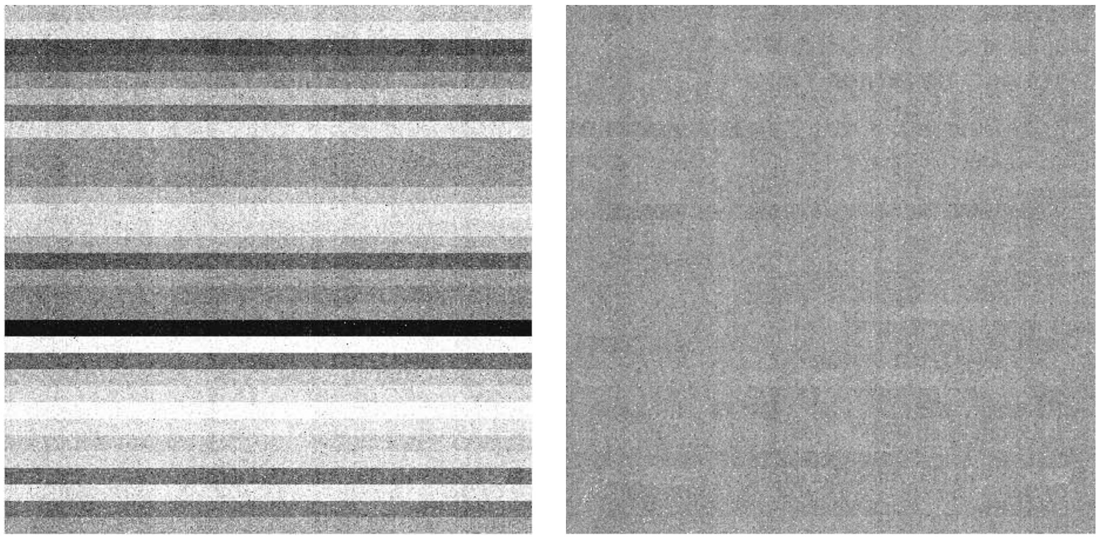

Figure 3.3 (Left) Three second image of the science-grade detector using correlated double sample (CDS) readout mode before reference pixel subtraction. The image has been rotated 90 degrees clockwise so the spectral format runs parallel with the readout channels. (Right) Image after reference pixel subtraction has been implemented. The median values of the reference pixels at the top and bottom, which corresponds to the right and left in the rotated image, of each channel are subtracted from each analogous channel to eliminate the offsets.

3.4.2 Optimizing The Detector Settings

Several configurations of the JADE2 card were tested to optimize the system. One of the main changes to the JADE 2 card that was made to reduce noise was to configure the JADE 2 to bypass the USB power for a separate 5V power supply. Several different grounding schemes were also tested to find the setting with the lowest introduced noise. In addition, the JADE 2 card was enclosed in an aluminum box to reduce the possibility of electrical interference with external sources.

There were several voltage settings for the detector that had to be adjusted to find the lowest noise values. One of the settings that was examined was the reverse bias of the detector, which is controlled by two voltage settings, Vreset and Dsub. The reverse bias controls the depletion region in each pixel. An increase in reverse bias will result in a larger depletion region, which will decrease the capacitance. Reducing the capacitance will lower measured noise from the accumulated charge, but will increase the dark current in the device. Teledyne runs their detectors during testing at 0.25 Volts reverse bias, which corresponds to Vreset = 0.30V and Dsub = 0.55V. Several possible combinations of Vreset and Dsub were investigated and the final configuration that was decided upon was a reverse bias of 0.3 Volts, with Vreset = 0.3V and Dsub = 0.60V, which decreased our pixel capacitance and noise with a negligible penalty in dark current (see Section 3.4.4). Several values of the detector's gate voltage for the internal current sources, Vbiasgate, were also tested to understand the affects it would have on the noise levels. Values ranging from $1.84 - 2.3$ Volts were tested. Surprisingly, the voltage that Teledyne uses for their detector testing, Vbiasgate = 2.3V resulted in the largest noise values in our system. The final value for the bias gate voltage was determined to be Vbiasgate = 2.0V.

One of the main setting changes that made a significant difference on the overall noise level of the MOSFIRE detector was switching from the single-ended to differential preamp input mode (see Figure 3.4). With single-ended mode, the input preamp voltages are differenced with respect to ground, while in differential mode the input voltages are differenced with respect to each other. Since differential mode is independent of ground, it is less likely to have noise issues. This modification decreased the noise level by ~ 7 e^- in CDS mode.

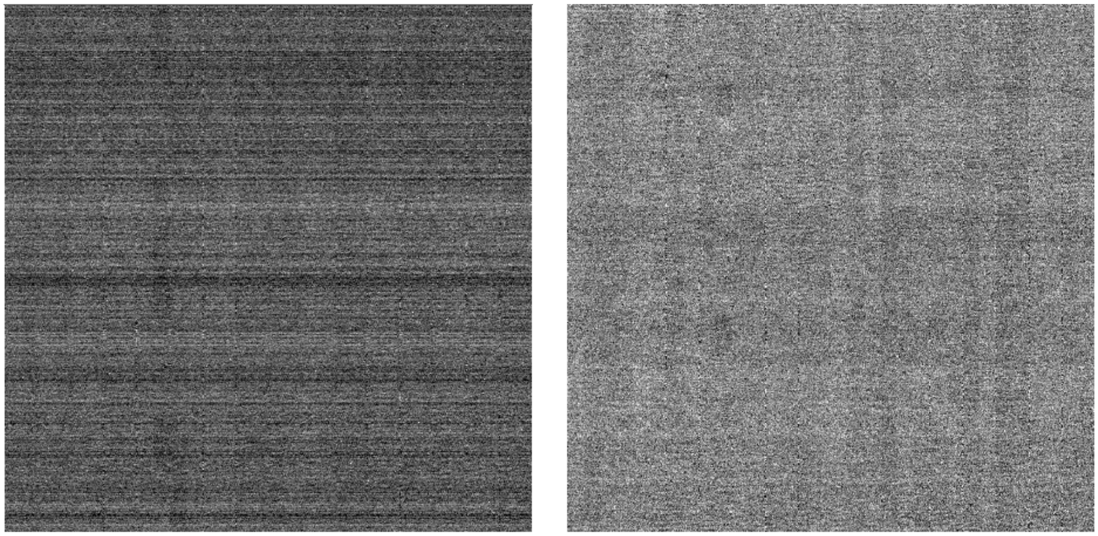

Figure 3.4 (Left) Single-ended preamp input mode for a 2 second CDS with reference pixel subtraction. (Right) Differential preamp input mode for a 2 second CDS with reference pixel subtraction. The differential input mode reduced the noise for the MOSFIRE detector considerably.

3.4.3 Detector Systems

It was discovered in May of 2010 that the field flattener lens, which sits directly in front of the detector, contains radioactive Potassium-40. To quantify the affect this would have on our image quality, I took several long (1000 seconds) exposures to compare to images taken before the detector had been installed into the final MOSFIRE detector head with field flattener lens. The images taken with the lens in place had approximately $\sim 29,000$ pixels which were more than 3 sigma away from the mean pixel value of the entire frame. This amount of pixels is 0.7% of the entire detector array and is approximately a factor of 2 greater than for images analyzed without the lens in place. No modifications were considered necessary as this value was deemed to have a negligible impact on the science capabilities of MOSFIRE.

The detector is mounted inside of the detector head which is kept at a constant temperature of 77 Kelvin while the rest of the MOSFIRE instrument is held at 120 Kelvin. Since MOSFIRE was designed for use in multiple spectral orders 3, 4, 5, 6 (K, H, J, Y), the detector head was constructed with a focus mechanism to obtain optimal focus in each wavelength band. A coordinate measuring machine (CMM) was used to measure all surfaces of the detector head with respect to themselves and each other to ensure that there was no tilt in the detector system and that the detector was coplanar with the optical axis. In addition, to keep possible stray light from reflecting onto the detector, I hand-painted several surfaces of the detector head with an Aeroglaze flat black polyurethane coating. First light was achieved in the lab on July 1st of 2010 shortly after the detector system was integrated into MOSFIRE. During subsequent tests it was revealed that the instrument is very close to being parfocal in all bands and so it was decided to fix the focus stage at a single location.

3.4.4 Read Noise And Dark Current

Teledyne's testing of the H2RG has shown that extremely low read noise levels, below 5 e^-, can be reached. Teledyne, however, conducted their tests using standard controllers and not the SIDECAR ASIC. One of my main goals was to verify that the ASIC system worked as well as a standard controller and could be used to reach the same low levels of read noise obtained by Teledyne. The readout modes allowed for the MOSFIRE detector are single, correlated double sample (CDS), multiple-correlated double sample (MCDS), or up-the-ramp (UTR) with a minimum exposure time of 1.45 seconds. A CDS exposure will take one frame at the beginning of the exposure and one at the end of the integration and then subtract the first frame from the second. This scheme calculates the true signal without any offset from the detector itself. MCDS consists of N number of non-destructive reads taken at both the beginning and the end of an exposure (Figure 3.5). The N reads are then averaged for each group. The final image is constructed from differencing the first group from the second group.

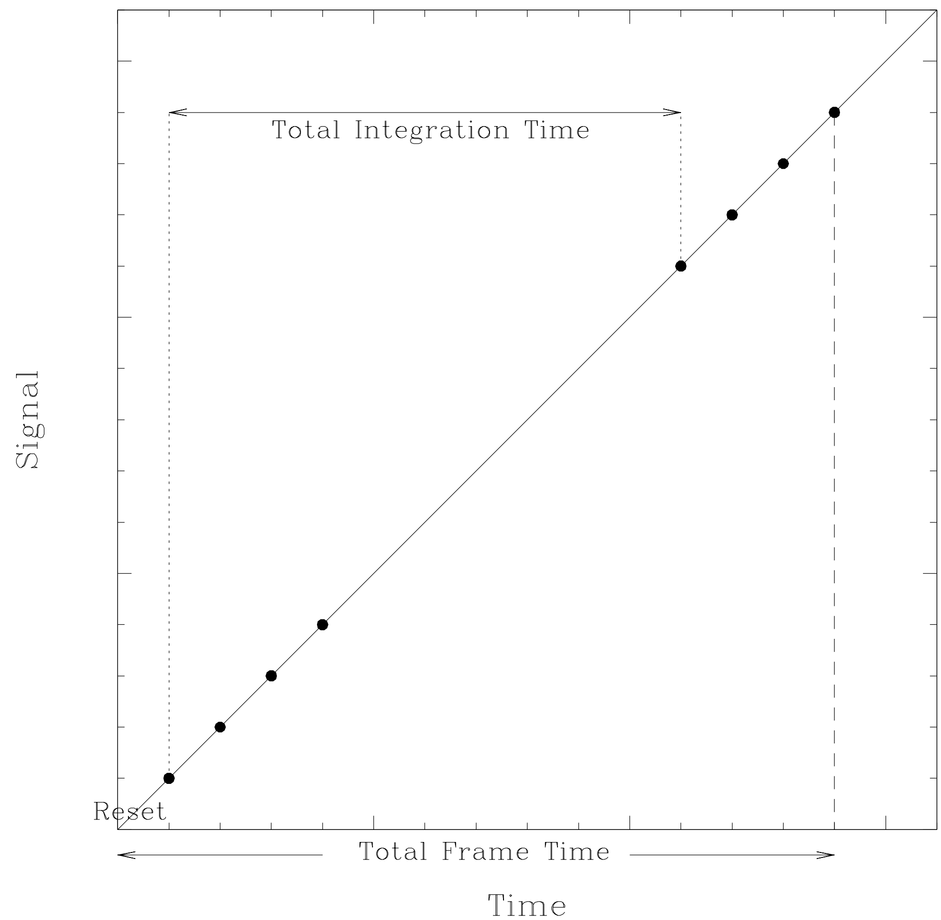

Figure 3.5 An illustration of the multiple-correlated double sample (MCDS) read out scheme. The horizontal axis represents time after the detector has been reset, while the vertical axis represents signal on the detector. This example demonstrates an MCDS 4 exposure, which should decrease the read noise by a factor of $\sqrt{4} = 2$. The total integration time on the detector is from the first read of the first group to the first read of the second group. The total amount of time it takes to read out the final frame is from the detector reset to the last read of the second group.

Table 3.1. Read Noise Measurements

MCDS Reads	Data Set #1	Data Set #2	Theoretical
1	17.4	17.1	17.3
4	8.8	8.9	8.6
8	6.5	6.5	6.1
16	4.9	4.9	4.3
32	3.8	3.8	3.1
64	3.3	3.4	2.2
100	3.0	3.1	1.7
128	3.1	3.1	1.5

Note. — All noise values are reported in e^-

MCDS, or Fowler sampling as it is also known in recognition of Al Fowler who was one of the first to realize it's importance (Fowler & Gatley 1990), can be used to obtain better read noise values. Theoretically, MCDS readout will impact the read noise by a factor of $1/\sqrt{N}$. For clarification, an MCDS 4 exposure will have four reads taken at the beginning and four reads taken at the end (see Figure 3.5). This should reduce the noise by a factor of 2 from the fiducial read noise value. Figure 3.6 shows our results, with the MOSFIRE detector reaching a read noise of 4.9 e^- by an MCDS 16 exposure. By 64 reads the noise has reached a level of 3 e^-. There are two different data sets shown in Figure 3.6, as well as what would be expected theoretically from the assumption that the noise would decrease by $\sqrt{N}$. Table 3.1 list the results of the read noise measurements. There is an apparent flattening of the read noise level past MCDS 100, which can be modeled by a contribution of $1/f$ noise becoming the dominate noise source.

Dark current was tested by comparing a long dark frame (1800 seconds) to a short dark frame (2 seconds). A value of <0.008 e^- s^{-1} $pixel^{-1}$ was measured on average, which is approximately a factor of 100 times improvement over previous

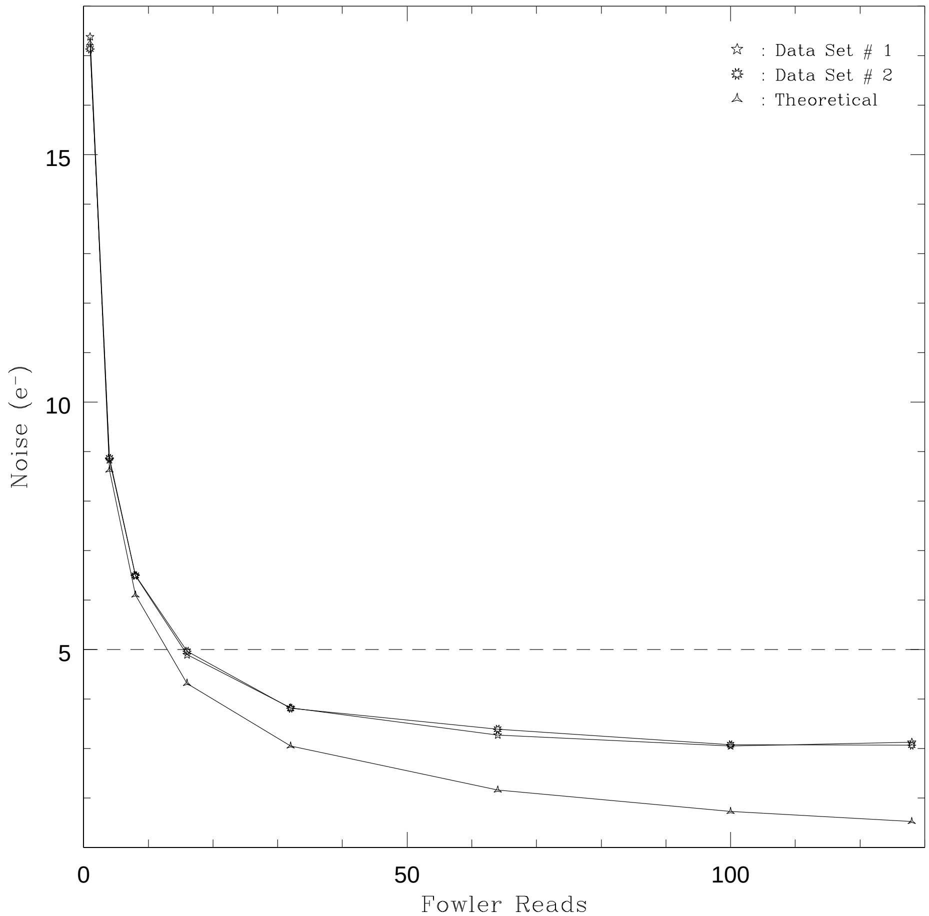

Figure 3.6 Read noise plot for the MOSFIRE detector using the SIDECAR ASIC readout electronics. There are two separate in-lab data sets shown compared to the theoretical read noise values assuming a noise reduction of $1/\sqrt{N}$. The read noise levels reach below 5 e^- by MCDS 16, which validates the ASIC's performance. The dashed line shows the 5 e^- level.

generations of infrared detectors. This measurement demonstrates that the dark current is a negligible source of noise for the MOSFIRE detector.

3.4.5 Gain Setting And Linearity

With our current settings, Teledyne reports a total gain of 2.15 e^-/DN for the MOSFIRE detector. To verify this number there are two different methods that can be used. The first is to estimate the gain using the following equation McLean (2008):

$$g = \frac{V_{fs} C}{2^n A_g e} \tag{3.1}$$

V_{fs} is the full-scale voltage swing allowed on the A/D unit, which is 3 V for the current configuration. C is the detector capacitance at $\sim 40 \times 10^{-15}$ farads, n is the number of bits, which is 16, and e is the charge of an electron. A_g is the total gain product. MOSFIRE uses the gain setting of 15.05 dB. To obtain the total gain product the conversion in Equation 3.2 can be used.

$$\text{dB} = 20\, log_{10}(A_g) \tag{3.2}$$

The resulting value from Equation 3.2 is 5.66 for A_g. By using all of the above values with Equation 3.1, the estimated gain is 2.05 e^-/DN.

Additionally, the gain can be measured using an independent method known as the variance method" or "photon transfer" method, which uses a sequence of exposures with increasing signal. No assumptions need to be made about the capacitance or gain, which is a benefit of the variance method. By plotting the variance versus the signal from this data set, the inverse slope of the corresponding line will result in the gain of the detector. There are two noise sources that contribute to these measurements: the photon noise of the signal photoelectrons (p) and the readout noise from the detector output amplifier (R). The two noise sources will add in quadrature:

$$(noise)^2 = p^2 + R^2 \tag{3.3}$$

The $(noise)^2$ is the variance. The above equation must be converted from photoelectrons to DN (or counts in the ADC) using the gain (g). The equation now becomes:

$$[\frac{(noise)}{g}]^2 = [\frac{p}{g}]^2 + [\frac{R}{g}]^2 \tag{3.4}$$

Here the $[\frac{(noise)}{g}]^2$ is the variance, V, in terms of DN. The photoelectron noise (p) is the square root of g*S, where S is the signal in DN. This leads to:

$$V = \frac{1}{g}S + [\frac{R}{g}]^2 \tag{3.5}$$

which is the equation of a straight line, where $\frac{1}{g}$ is the slope, $[\frac{R}{g}]^2$ is the y-intercept, and $V = (noise/g)^2$ is the variance. Since g can be obtained from the slope then R, the read noise for a CDS frame, can be independently calculated from the y-intercept of the line. The measured gain is 2.14 e^-/DN (Figure 3.7), which is in good agreement with Teledyne's value of 2.15 e^-/DN and is within less than a five percent difference from the estimated gain (2.05 e^-/DN). Therefore we adopt the gain value of 2.15 e^-/DN for the MOSFIRE detector. The read noise value calculated from the y-intercept (8.57 e^-) is less than our earlier measured value of $\sim$17 e^-. This difference can be attributed to the large error on the variance measurements and a similar error in CDS frames.

The linearity and saturation level of the detector can be measured from the same data set used for the gain calculation. The saturation level at the ADC limit

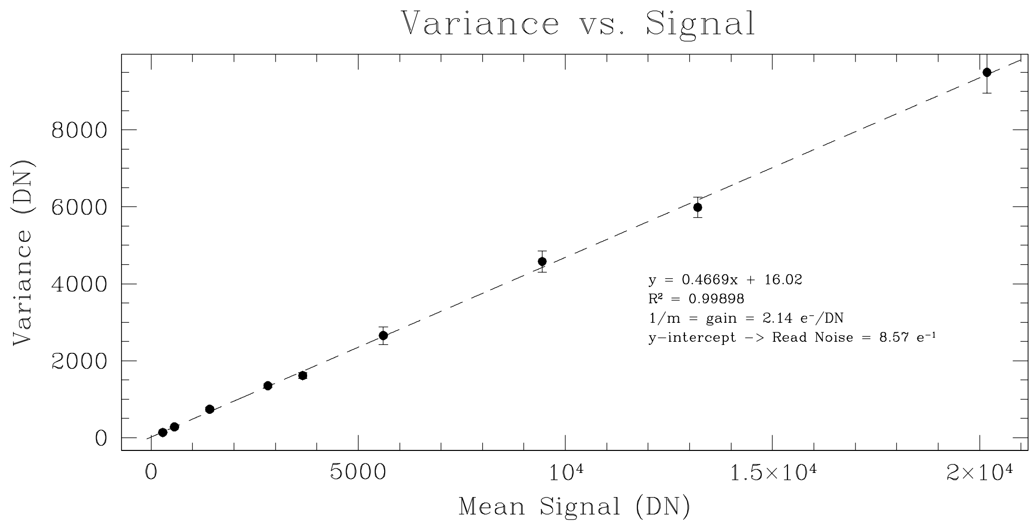

Figure 3.7 The "variance method" is shown here to estimate the detector gain. By using a sequence of exposures with increasing signal, the gain can be calculated from the inverse of the slope of the variance versus signal. The value calculated from this method (2.14 e^-/DN) is in very good agreement with Teledyne's value of 2.15 e^-/DN and is within less than 5% with the estimated value (2.05 e^-/DN).

was measured at ∼42,000 DN, which corresponds to ∼90,000 e^-. The detector was measured to be linear up to ∼80% of full well, after which it can be fit with a third order polynomial (Figure 3.8). This is a global correction and it is not applied to the final image before read out. For science cases which may come close to saturating the detector, such as exoplanet studies, a pixel-by-pixel linearity correction should be measured and then applied.

3.4.6 Bias Drifts

In early lab testing of the science-grade detector it was noted that CDS exposures with no illumination had negative DN counts. A CDS image is composed of 4 raw frames, with the first and third frames are reset frames while the second and fourth frame are used to calculate the final image. To understand the negative

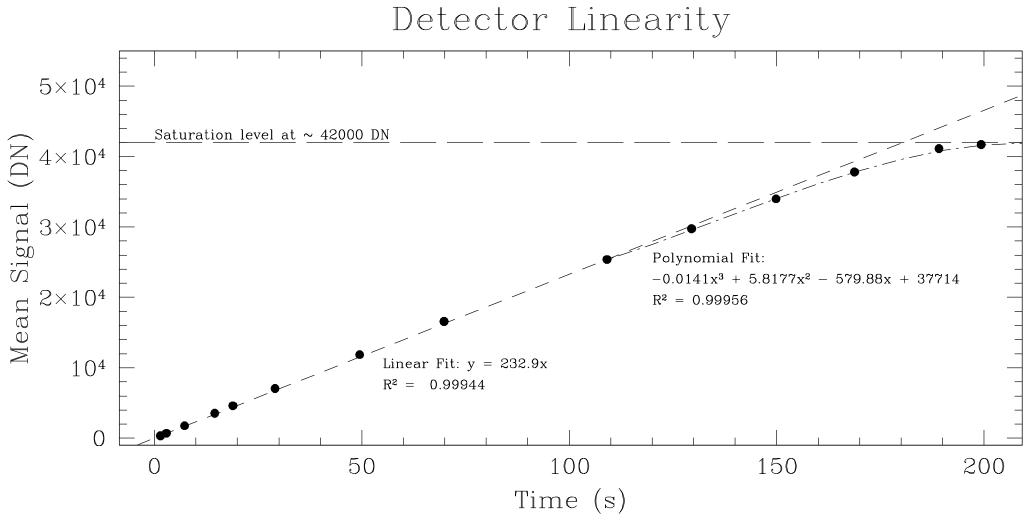

Figure 3.8 The detector was measured to hit the ADC limit at ∼42,000 DN, which corresponds to ∼90,000 e^-. It has a linear response up to ∼80% full well depth, after which the detector response can be well modeled with a polynomial fit.

DN counts, the individual raw frames were read out and examined separately. The results of this analysis showed a sharp drop in the readout directly after the detector is reset and that it takes approximately one readout time (1.45 seconds) before the signal settles (Figure 3.9). To resolve this anomaly, an extra frame can be read and ignored at the beginning of every exposure, allowing the detector to settle to the correct level after being reset. The total amount that the bias level drops is ∼ 8 DN, or ∼ 17 e^-, which is significantly smaller than the well depth that will typically be reached when integrating on a science target. In addition, the added "discarded" read causes an overhead in the total exposure time. We have elected to not use the "discard" frame following reset since the extra overhead in readout time is not desirable. In addition, we find that it is not critical to use the "discard" frame for MOSFIRE since MCDS mode will primarily be used for science exposures and the bias drift is more noticeable in CDS mode.

However, the option remains available in MOSFIRE's code for science cases that require very short exposure times and/or very precise flux calibration.

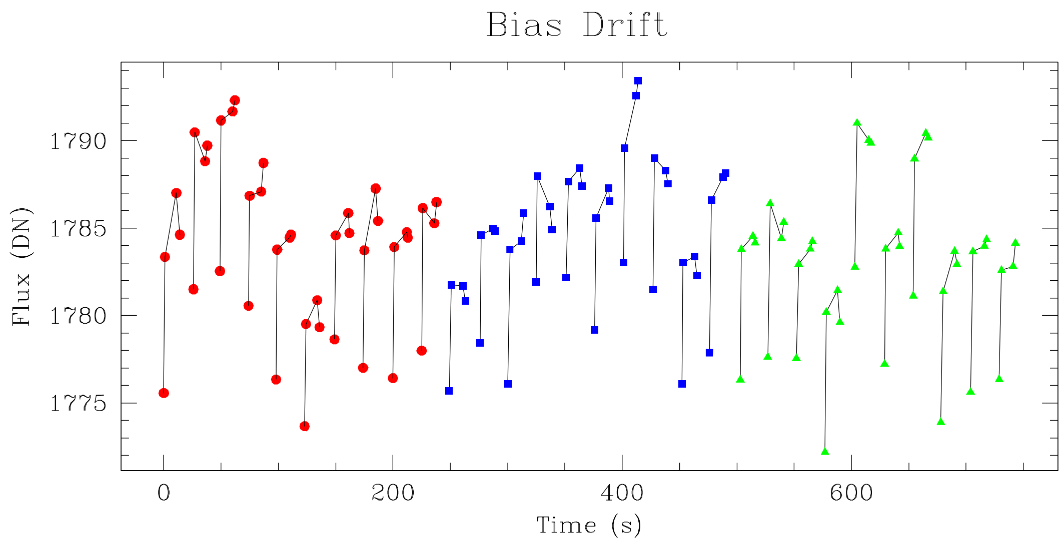

Figure 3.9 A CDS image is composed of 4 raw frames. Shown here are the 4 raw frames for a total of 30 separate CDS images. The different colors represent three sets of CDS images taken at different times (10 CDS images in each set). There is an obvious drop in the readout directly after the detector is reset in all 30 frames.

3.4.7 Persistence

Persistence is a known issue among infrared detectors (e.g., Smith et al. 2008). It occurs when charge becomes trapped within the detector, leaving a "ghost" image of the previous exposure. This extra charge will leak out slowly over time and can typically be modeled by an exponential decay. To characterize the persistence of the MOSFIRE detector, it was illuminated to reach a value close to the ADC limit at ~39,000 DN. The detector was then put into dark and seven consecutive 200 second exposures were taken. The residual counts measured above the inherent noise of the detector was considered to be persistence. From

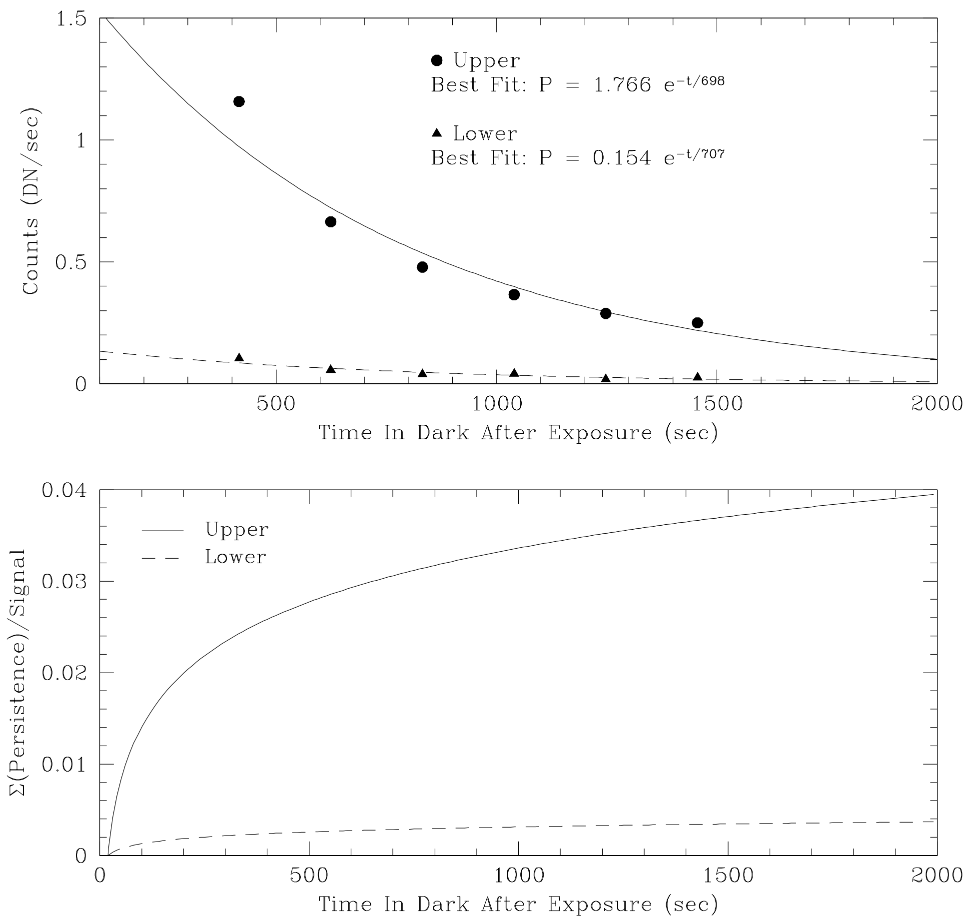

Figure 3.10 Data taken during cool down 10 in the lab were used to examine persistence. (Top) Time after exposure versus ADU (DN) per second. All positions in the spatial direction of the detector can be fit with an exponential function with almost the same time constant. The amplitude of persistence, though, is much higher for the top half of the detector. Data taken during cool down 8 was also examined that had a different level of illumination. The time constant was still approximately the same. (Bottom) Time after exposure versus the summed persistence over the original signal. The upper half of the detector shows much higher levels of persistence.

this experiment, the MOSFIRE detector has a calculated decay time constant of ∼660 seconds, as shown in Figure 3.10. With closer examination a factor of ∼10 difference is measured between the amplitude of the persistence along the spatial direction, perpendicular to the dispersion, of the detector. Data taken during cool down 8 that had a lower level of illumination compared to cool down 10 was also examined. The time constant appears to be consistent regardless of the level of illumination.

3.5 On-Sky Results

MOSFIRE obtained " first light" on 2012 April 4th. Many engineering tasks were completed to verify performance of the entire MOSFIRE system, including the detector system, over four separate commissioning runs from 2012 April to June. During this time the MOSFIRE team optimized observing procedures while also observing science targets to determine practical performance limits.

3.5.1 Read Noise

We took a series of dark images once MOSFIRE was installed in the telescope, since it was assumed that the telescope and surrounding systems could introduce new noise sources. A noise banding was noticed on the detector that appears perpendicular to the readout channels and which was not previously seen in the lab. Read noise tests were repeated in the same manner as discussed in Section 3.4.4. It was discovered that the read noise increased by approximately 3 e^- for CDS mode, but noise levels became comparable to in-lab testing in MCDS mode (Figure 3.11; Table 3.2). In order for MCDS readout to average over this added noise the banding must be variable in the time domain. No action was taken to eliminate the additional noise source since this negligible level of added noise will not affect MOSFIRE's performance.

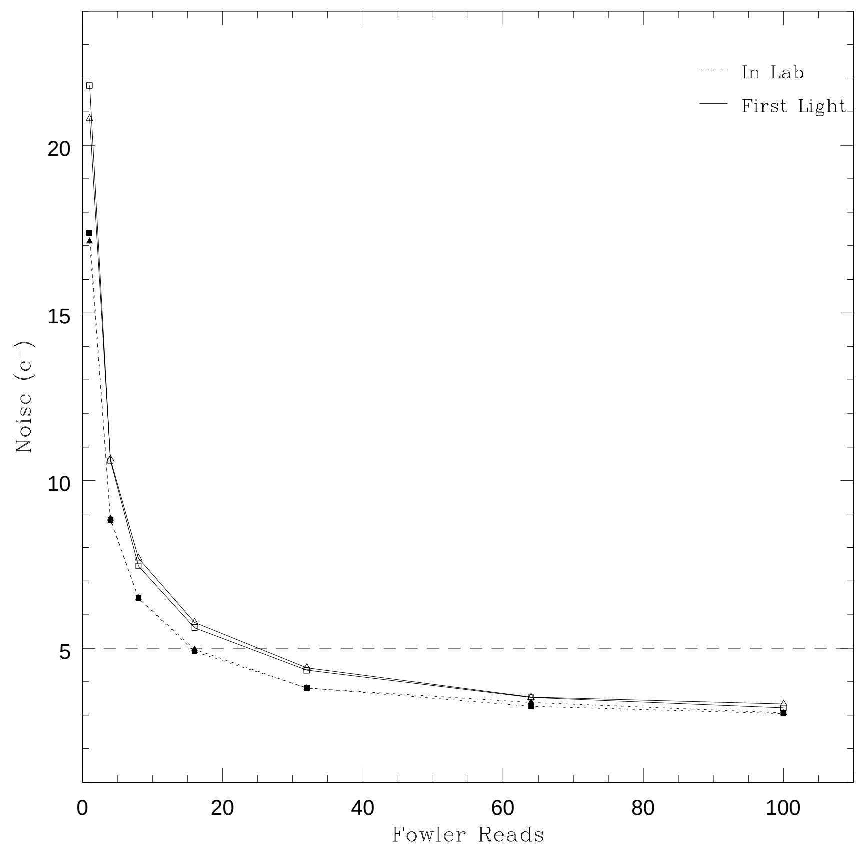

Figure 3.11 Read noise comparison between in-lab (dotted) and on the telescope (solid) measurements. The noise is slightly worse for CDS readout mode at the telescope, but it becomes comparable to in-lab data when MCDS readout with longer exposure times are used. The 5 e^{-} level is designated with a dashed line.

3.5.2 Science Verification

Optimizing the performance of the MOSFIRE detector was extremely important to be able to obtain the best possible scientific data. MOSFIRE's first light on the telescope occurred on 2012 April 4th and during the subsequent commissioning

Table 3.2. Read Noise Measurements At Keck Observatory

MCDS Reads	Telescope #1	Telescope #2	Lab #1	Lab #2
1	20.8	21.8	17.4	17.1
4	10.6	10.6	8.8	8.9
8	7.7	7.5	6.5	6.5
16	5.8	5.6	4.9	5.0
32	4.4	4.3	3.8	3.8
64	3.5	3.5	3.3	3.4
100	3.3	3.2	3.0	3.1

Note. — All noise values are reported in e^-

runs, the MOSFIRE team began science verification with the instrument. Both galactic and extragalactic targets were observed in imaging and spectroscopic modes.

To demonstrate MOSFIRE's imaging capability, several multi-color images were taken. Exposure times for imaging were found to be optimal at approximately 9, 4, and 4 seconds for J, H, K_s band respectively. The left-hand side of Figure 3.12 shows a JK_s color composite of the Antennae Galaxy taken during MOSFIRE commissioning. A 5-point dither pattern was used with a total integration of 58 seconds and 52 seconds at each position, respectively, for J and K_s.

Even though MOSFIRE is an exceptional wide-field imager, it will be used mainly for spectroscopic observations. During commissioning, numerous multi-object masks were observed of faint, high-redshift ($z \sim 2-3$) galaxies. For a typical K-band exposure, with a measured sky background of 17.32 (Vega), a 180 second integration time was shown to be optimal for subtracting OH lines. Typically, an ABAB nodding scheme was employed with a nod size of $\pm 1\farcs5$.

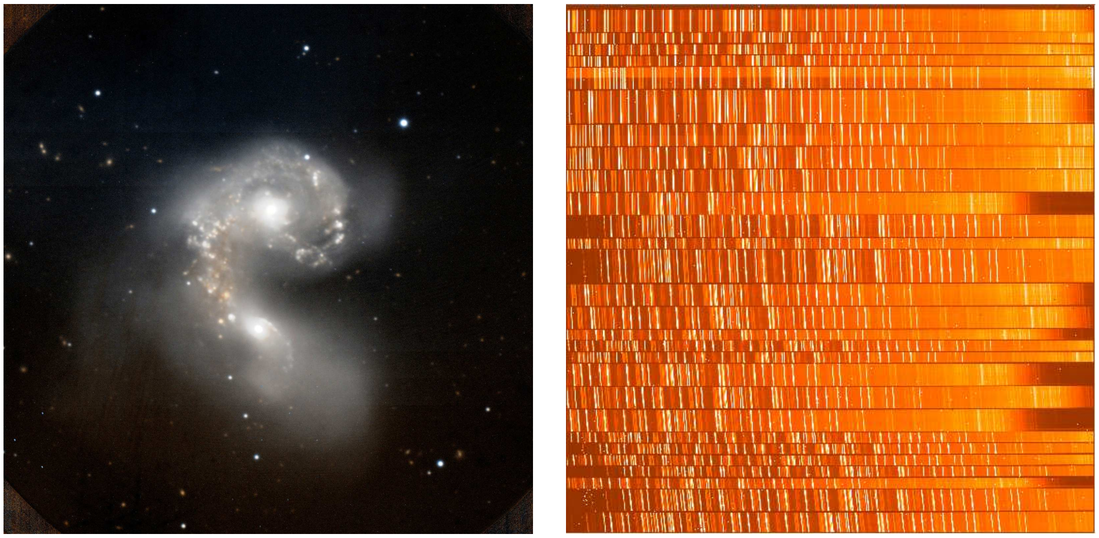

Figure 3.12 (Left) JK_s color composite of the Antennae Galaxy taken during MOSFIRE commissioning. Image created by Sarah Logsdon. (Right) MOSFIRE K-band multi-object spectra of $z \sim 2$ UV-selected star-forming galaxies. Due to the numerous OH lines that exist in the near-infrared, the commissioning team examined the best possible methods for reducing noise, while optimizing OH line subtraction.

The right-hand side of Figure 3.12 shows a MOSFIRE K-band multi-object spectroscopic image. MOSFIRE's higher sensitivity and multi-object capability will enable new scientific discoveries that were previously not feasible.

3.6 Summary

The H2RG selected for MOSFIRE has proven to be an outstanding device in many respects. The reference pixels have proven to work extremely well to mitigate any offsets that occur between amplifier readouts. The detector's voltage settings have been thoroughly tested to optimize MOSFIRE's performance. Measurements have shown low noise (< 5 e$^-$) and low dark current (< 0.008 e$^-$ s^{-1}

pixel^{-1}), which allows MOSFIRE to reach it's desired sensitivity goals. These measurements verify the ASIC and JADE2 performance, which was one of the major goals of this project. In addition, the MOSFIRE detector has high quantum efficiency and good uniformity. One issue with the MOSFIRE detector is the charge persistence. The levels of persistence, especially in the upper half of the detector, may cause issues, especially when changing from imaging to spectroscopic mode within a single night. Observers will need to exercise caution and allow sufficient decay time when changing modes.

Once installed at Keck Observatory, I demonstrated that the detector system worked correctly. The small amount of additional noise that was measured after installation into the telescope is deemed insignificant for the required sensitivity limits. During commissioning, the MOSFIRE team tested and demonstrated the appropriate observing procedures to ensure the best observational results for the Keck scientific community. MOSFIRE became available for the general Keck Observatory community in September of 2012. Since then it has become one of the most requested instruments at the observatory. Chapter 4 of my thesis discusses several important scientific results from MOSFIRE using spectroscopic data to better understand the physical mechanisms that are important during galaxy formation.

Figure 3.13 The MOSFIRE team in the Keck I observing room celebrating first light during commissioning. The team members from left to right are Charles Steidel, Nicholas Konidaris, Ryan Trainor, Jason Weiss, Gwen Rudie, Keith Matthews, Marc Kassis, Allan Honey, Sean Adkins, Ian McLean, Shui Kwok, myself, and Gregory Mace. There were many others who contributed to MOSFIRE's success. Important team members that were not present during this picture are Harland Epps, Bob Weber, Ted Aliado, Ken Magnone, Hector Rodriquez, John Cromer, John Canfield, Chris Johnson, George Brims, Jason Fucik, and Alice Shapley.

CHAPTER 4

The Mass-Metallicity Relation Of A $z \sim 2$ Protocluster With MOSFIRE

4.1 Introduction

Galaxy clusters constitute the most massive gravitationally bound structures in the universe, making them excellent laboratories for studying galaxy formation in the most extreme environments. Galaxy properties have been demonstrated to correlate with environment in the local universe (e.g., Hogg et al. 2004; Kauffmann et al. 2004; Clemens et al. 2006; van der Wel et al. 2010; Wetzel et al. 2012). Specifically, galaxies found in the central, densest regions of clusters at $z < 1$ are typically early-type galaxies with low star-formation rates (SFRs), while more active, late-type galaxies are preferentially located in the sparser edges of the cluster field. These observations suggest that environment plays a key role in the evolution of galaxies, with large-scale overdense regions appearing to foster the earliest sites of galaxy formation.

Detailed cluster studies have been done out to $z \sim 1$ (e.g., Holden et al. 2009; Patel et al. 2009), but there is limited information for clusters at $z > 1$ (but see e.g., Papovich et al. 2012). Protoclusters at $z > 2$ are still in the process of forming and have not yet virialized, making them perfect for studying the origin of the environmental trends observed locally. Measuring the physical properties (e.g., stellar mass, metallicity, velocity dispersion) of protocluster galaxies will facilitate a better understanding of the processes that are relevant in dense environments and the formation times of cluster versus field galaxies, where field galaxies are defined as those not residing within an overdense region.

A redshift-space overdensity at $z = 2.3$ was discovered in the HS1700+643 field during the course of a spectroscopic survey, which is likely a progenitor of the rich galaxy clusters that are observed at $z \sim 0$ (Steidel et al. 2005). This protocluster represents one of the best options for studying the relationship between the physical properties of galaxies and environment during the epoch when the global star-formation rate was at its peak since these galaxies were discovered using a well-defined redshift selection function, enabling a robust estimate of the galaxy overdensity. There exists a comprehensive data set for the HS1700 field that includes: UV spectroscopy (Steidel et al. 2004, 2005); ground-based optical, near-IR and Spitzer mid-IR photometry (Shapley et al. 2005a); HST/ACS (Peter et al. 2007); NB Lyα imaging (Digby-North et al. 2010); NB Hα imaging (Digby-North et al. 2010); and X-ray data (Digby-North et al. 2010). These data allow the identification of structures in redshift space and mapping of the sources on the sky, as well as trace SFRs, active galactic nuclei (AGN) activity and stellar populations (i.e., masses and ages).

With these existing data sets, Charles Steidel of Caltech and collaborators have identified a large sample of galaxies contained within the prominent redshift spike, including 37 BX/MD galaxies ($z \sim 2$ UV-selected galaxies, analogous to LBGs, see Figure 4.1). There are additionally 123 LAEs, 62 Hα Emitters (HAEs), 6 extended Lyα blobs, 75 Distant Red Galaxies (DRGs) identified in the HS1700 field. All of the narrowband objects, and a large fraction of the DRGs, are likely associated with the protocluster. Another benefit of this data set is the extensive spectroscopic coverage of field galaxies.

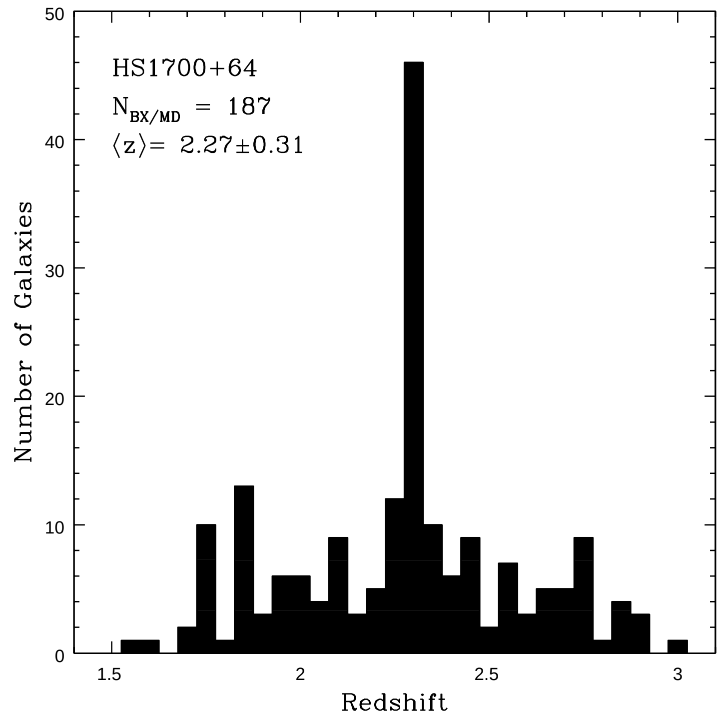

Figure 4.1 Histogram of BX/MD-selected galaxies in the HS1700 field. An obvious overdensity can be seen at $z \sim 2.3$.

Prior analysis of galaxies within and outside of overdense regions has revealed environmental effects where protocluster members have older ages and higher stellar masses than identically-selected galaxies outside of the protocluster (Steidel et al. 2005). However, HST/ACS morphologies of the same UV-selected galaxies do not indicate any significant trend for galaxies within the protocluster as compared to field galaxies at similar redshift (Peter et al. 2007). Near-infrared (rest-frame optical) spectroscopy is crucial for examining numerous physical properties of galaxies at $z \sim 2-3$, such as the metallicity and gas dynamics, to better understand the underlying physical processes occurring inside and out of overdense environments. However, the HS1700 field previously did not contain a systematic statistically comprehensive sample of near-IR spectroscopic data.

With the extremely efficient multiplexing capabilities of MOSFIRE, I have obtained JHK spectroscopy in the HS1700 field for a large number of protocluster and field galaxies. The emission lines [O II], Hβ, [O III], Hα, [N II], and [S II] can be measured with this near-IR data set. Based on the relative strengths of these emission lines I can infer numerous properties about the star-forming regions of the target galaxies. The velocity dispersion, which describes the dynamics of the gas bound to the galaxy, will be obtained from the Hα emission line. Oxygen is typically used to probe the gas-phase metallicity because it is the most abundant heavy element in star-forming galaxies. There are three commonly-used strong-line ratios used to estimate the oxygen abundance: $R_{23} \equiv$ ([O II]λ3727+[O III] $\lambda\lambda$4959,5007/ Hβ), $N2 \equiv$ log([N II]/Hα), and $O3N2 \equiv$ log([O III]λ5007/ Hβ)/([N II]λ6584/Hα). A comparison of all three indicators can be used for the HS1700 field. The electron density and temperature can also be calculated, respectively, from the [S II]$\lambda\lambda$6717,6732 ratio and the [O III]$\lambda\lambda$4959,5007/[O III]λ4363 ratio. Since the [O III]λ4363 to [O III]$\lambda\lambda$4959,5007 ratio has a maximum value of $\sim$10% for extremely low-metallicity galaxies and decreases at higher metallicities (Kakazu et al. 2007), I may only be able to place an upper limit on the electron temperature for most galaxies. The ionization parameter of star-forming galaxies is typically characterized by the ratio between the density of ionizing photons and the density of hydrogen atoms. The $O_{32} \equiv$ ([O III]$\lambda\lambda$4959,5007/[O II]$\lambda\lambda$3726,3729) indicator, which describes the local ionization state of the HII regions, can be utilized to estimate the ionization parameter. Dust extinction will be measured from Balmer line ratios, the $G - \mathcal{R}$ color, or SED modeling, which can be calculated from the ancillary data. SFRs can be inferred from the Hα luminosity, in addition to SFRs from rest-frame UV-luminosity (also available from ancillary data), to examine how environment affects star formation at these redshifts. The majority of these physical property measurements will be further discussed in Chapter 5.

In this chapter I investigate the connection between metallicity and stellar mass with respect to environment in the HS1700 field. The metallicity of a galaxy reflects the past history of star formation, and is additionally modulated by gas inflows and outflows (Finlator & Davé 2008; Peeples & Shankar 2011; Davé et al. 2012). A relationship between stellar mass and metallicity has been well established for local galaxies spanning over three orders of magnitude in stellar mass, where higher-mass galaxies have larger gas-phase metallicities (Tremonti et al. 2004). This trend has been shown to hold to at least $z \sim 3$ (Erb et al. 2006a; Maiolino et al. 2008), however it appears to shift towards lower metallicity at fixed stellar mass as redshift increases. Low-redshift studies of the mass-metallicity relation (MZR) with respect to environment have demonstrated that galaxies found in overdense regions have, on average, higher metallicities compared to field galaxies of the same mass (Cooper et al. 2008; Ellison et al. 2009). Similar measurements of metallicity as a function of environment have yet to be performed at high redshift.

For this sample of protocluster and field galaxies at $z \sim 2$ in HS1700, I have measured the important rest-frame optical diagnostic emission lines Hα and [N II]λ6584 to estimate the gas-phase oxygen abundance with the $N2$ indicator from MOSFIRE K-band spectra. This data set will make possible for the first time the examination of the MZR for high-redshift protocluster galaxies compared to a field control sample, which will lead to a better understanding of how gas supplies are regulated during the formation of galaxies in extreme environments. A flat ΛCDM cosmology with $\Omega_m = 0.3$, $\Omega_\Lambda = 0.7$, and $H_o = 70$ km s^{-1} Mpc^{-1} is assumed throughout this analysis.

4.2 Sample

The HS1700+643 field (α = 17:01:01, δ = +64:11:58) was observed as part of the Keck Baryonic Structure Survey (KBSS; Rudie et al. 2012). The KBSS was designed to explore the properties of star-forming galaxies at $z \sim 2 - 3$ and the connection between galaxies and the intergalactic medium (IGM) within the same cosmic volumes. As such, galaxies were targeted for spectroscopy in the fields of background, hyper-luminous QSOs with high-resolution Lyα forest spectra. The galaxy spectroscopic survey was conducted with the blue arm of the Low Resolution Imaging Spectrometer (LRIS-B) on the Keck I telescope (Oke et al. 1995; Steidel et al. 2004). Galaxies were selected based on their rest-frame UV colors using the optical photometric "BX" ($z = 2.20 \pm 0.32$) and "MD" ($z = 2.73 \pm 0.27$) criteria of Adelberger et al. (2004) and Steidel et al. (2004, 2003). Steidel et al. (2005) identified a highly significant ($\delta \sim 7$) redshift-space overdensity of galaxies at $z = 2.300$ in the $15\farcm3 \times 15\farcm3$ HS1700 field in the course of the KBSS. The majority of high-redshift protoclusters have been identified around radio galaxies using narrowband imaging tuned to find Lyman Alpha Emitters (LAEs) (e.g., Venemans et al. 2007; Kodama et al. 2007; Wylezalek et al. 2013). In contrast, the HS1700 protocluster consists of a serendipitous discovery of a redshift spike within a spectroscopic survey with a well-defined redshift selection function, allowing for a robust estimate of galaxy overdensity.

I selected roughly equal numbers of UV spectroscopically-confirmed galaxies within and outside the redshift-space overdensity in order to conduct a detailed analysis of how environment affects the physical properties of $z \sim 2$ galaxies. Protocluster members are defined as galaxies at $z = 2.3 \pm 0.015$, while "field" galaxies are defined as residing outside of the redshift-space overdensity, but between $2.0 \lesssim z \lesssim 2.6$.

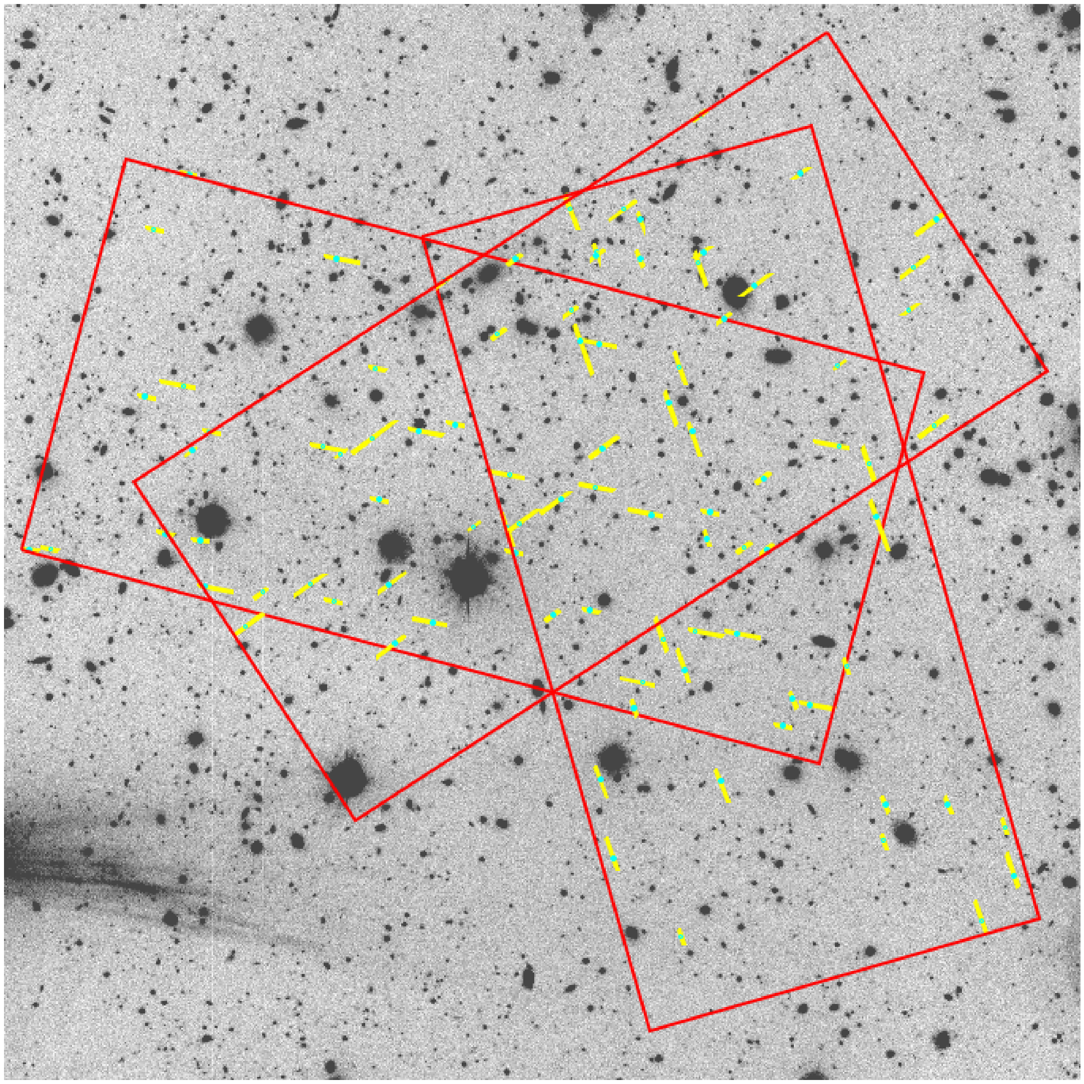

Figure 4.2 A section of the $\mathcal{R}$-band image for the HS1700 field with the three MOSFIRE masks used for this analysis. The image is $8' \times 8'$, with north up and east to the left. The MOSFIRE spectroscopic field-of-view for each mask is shown in red. Each slit is shown in yellow, while each object that was observed is shown in cyan.

I used the MAGMA slitmask design tool[1] to create three separate masks which included 24 protocluster galaxies and 21 field galaxies. A sample of 46

[1] http://www2.keck.hawaii.edu/inst/mosfire/magma.html

photometric candidates without spectroscopic redshifts were included to fill any empty slits on the three MOSFIRE masks. Figure 4.2 shows an overlay of all three masks on an $8' \times 8'$ section of the HS1700 $\mathcal{R}$-band image. The stellar mass (calculated from SED fitting, see Section 4.4.1) and K_s-band magnitude distributions of the galaxies selected indicate that my MOSFIRE protocluster and field samples are representative of their respective parent spectroscopic protocluster and field samples. For protocluster galaxies the mean and standard deviation for stellar mass and K_s magnitude (AB) of the MOSFIRE and parent samples are, respectively, $\langle \log(M_*)_{\rm MOS} \rangle = 10.3$ M$_\odot \pm 0.5$ and $\langle \log(M_*)_{\rm parent} \rangle = 10.3$ M$_\odot \pm 0.5$, $\langle K_{s,\rm MOS} \rangle = 22.6 \pm 0.5$ and $\langle K_{s,\rm parent} \rangle = 22.7 \pm 0.6$. For field galaxies the mean stellar mass and K_s magnitude (AB) of the MOSFIRE and parent samples are, respectively, $\langle \log(M_*)_{\rm MOS} \rangle = 10.1$ M$_\odot \pm 0.4$ and $\langle \log(M_*)_{\rm parent} \rangle = 10.2$ M$_\odot \pm 0.5$, $\langle K_{s,\rm MOS} \rangle = 23.0 \pm 0.5$ and $\langle K_{s,\rm parent} \rangle = 22.9 \pm 0.7$.

4.3 Observations And Data Reduction

Both photometric and spectroscopic data are required for the analysis of the MZR. I utilized broadband ancillary photometry for the stellar mass estimates and MOSFIRE K-band spectroscopy for gas-phase metallicity. In this section I describe both data sets and the reduction processes.

4.3.1 Broadband Ancillary Photometry

The HS1700 field photometric data, which was collected by Steidel and collaborators, spans the wavelength range from rest-frame ultraviolet to infrared. $U_nG\mathcal{R}$ imaging was performed on the William Herschel 4.2 meter telescope (WHT) with the Prime Focus Imager (Steidel et al. 2004). Near-IR JK_s imaging was ob-

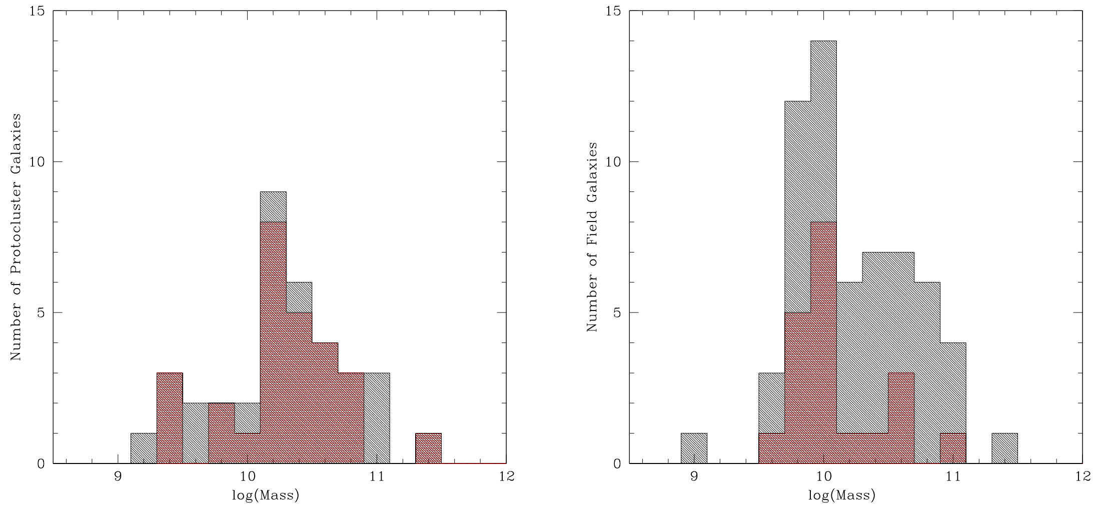

Figure 4.3 Histogram comparison of the stellar masses calculated from SED fitting (see Section 4.4.1) for the sample presented in this paper (red) and the parent sample (black). Both the protocluster and the field galaxies are representative of their respective parent samples. The stellar masses for my sample of protocluster galaxies and the parent sample are, respectively, $\langle \log(M_*)_{\rm MOS} \rangle = 10.3\ {\rm M}_\odot \pm 0.5$ and $\langle \log(M_*)_{\rm parent} \rangle = 10.3\ {\rm M}_\odot \pm 0.5$. The stellar masses for my sample of field galaxies and the parent sample are, respectively, $\langle \log(M_*)_{\rm MOS} \rangle = 10.1\ {\rm M}_\odot \pm 0.4$ and $\langle \log(M_*)_{\rm parent} \rangle = 10.2\ {\rm M}_\odot \pm 0.5$.

tained on the Palomar 5.1 meter Hale telescope with the Wide Field Infrared Camera (WIRC) (Erb et al. 2006c) and H-band imaging was completed with *HST*/WFC3-F160W (Law et al. 2012). Furthermore, HS1700 has photometric data from *Spitzer*/IRAC (Shapley et al. 2005b) and MIPS (Reddy et al. 2010). A complete description of the reduction of these data is contained in Reddy et al. (2012) and references therein.

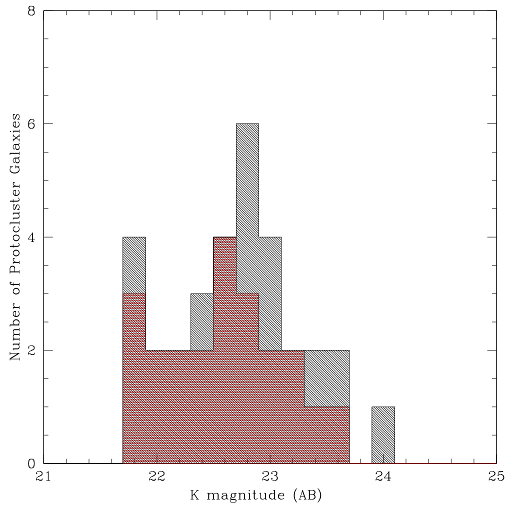

Figure 4.4 Histogram comparison of the K_s-band magnitudes in AB for the sample presented in this paper (red) and the parent sample (black). Both the protocluster and the field galaxies are representative of their respective parent samples. The K_s-band magnitudes for my sample of protocluster galaxies and the parent sample are, respectively, $\langle K_{s,\mathrm{MOS}} \rangle = 22.6 \pm 0.5$ and $\langle K_{s,\mathrm{parent}} \rangle = 22.7 \pm 0.6$. The K_s-band magnitudes for my sample of field galaxies and the parent sample are, respectively, $\langle K_{s,\mathrm{MOS}} \rangle = 23.0 \pm 0.5$ and $\langle K_{s,\mathrm{parent}} \rangle = 22.9 \pm 0.7$.

4.3.2 MOSFIRE Spectroscopy

K-band near-IR spectroscopy of the HS1700 field was obtained using the MOSFIRE instrument (McLean et al. 2012) on the Keck I telescope. The MOSFIRE K-band filter is centered at 2.162 μm with a full-width at half-maximum (FWHM) of 0.483 μm. The data were acquired over six nights during MOSFIRE commissioning runs on 2012 May 6th, 7th, and 9th and June 2nd, 5th, and 6th. As discussed in section 4.2, three separate MOSFIRE K-band masks were observed in the HS1700 field. Each individual exposure time was 3 minutes, with a total integration time of 172 minutes, 180 minutes, and 45 minutes on, respectively, masks 1, 2 and 3. All targets were observed with a slit width of $0\farcs7$ using an AB dither sequence with $3''$ offsets. The spectral resolution as determined from sky lines is $\sim$6 Å, which corresponds to $\Delta v \sim 80$ km s^{-1} ($R \simeq$3600). The seeing conditions over the six nights averaged $\sim 0\farcs5$. Of the original 21 targeted field galaxies, two galaxies were determined from Hα to reside outside of the "field" redshift space and two had redshifts such that Hα fell off of the spectral format. Excluding these four objects results in a total of 17 field galaxies that were expected to have Hα detections. I detected Hα for 22 out of 24 protocluster galaxies (92%) and for 15 out of 17 field galaxies (88%) where Hα fell within the MOSFIRE spectral format.

There are 6 new protocluster galaxy detections, including BX759, which was previously identified as a field galaxy due to an incorrect LRIS redshift measurement and 5 new field galaxy detections. I measured Hα for a total of 28 protocluster galaxies and 20 field galaxies, of which 17 protocluster galaxies and 5 field galaxies also have [N II] detections. Protocluster member BNB19 was discovered using a narrowband filter tuned to detect Lyα emission. As all other objects in the sample were selected on the basis of their rest-frame UV continuum colors, I have excluded BNB19 from this analysis, resulting in a final protocluster sample of 27 galaxies.

I utilized the MOSFIRE data reduction pipeline (DRP)[2] to reduce all of the data. The DRP produces two-dimensional wavelength-calibrated, sky-subtracted, registered and combined spectra for each object, along with a corresponding inverse variance spectrum. I then extracted one-dimensional spectra from the two-dimensional reduced science and variance images using standard `IRAF` routines. The resulting science and error spectra were placed on an absolute flux scale using observations of an A0 star obtained during the MOSFIRE runs. Each flux-

[2]http://code.google.com/p/mosfire/

calibrated, one-dimensional spectrum was then placed in a vacuum, heliocentric frame (Figure 4.5).

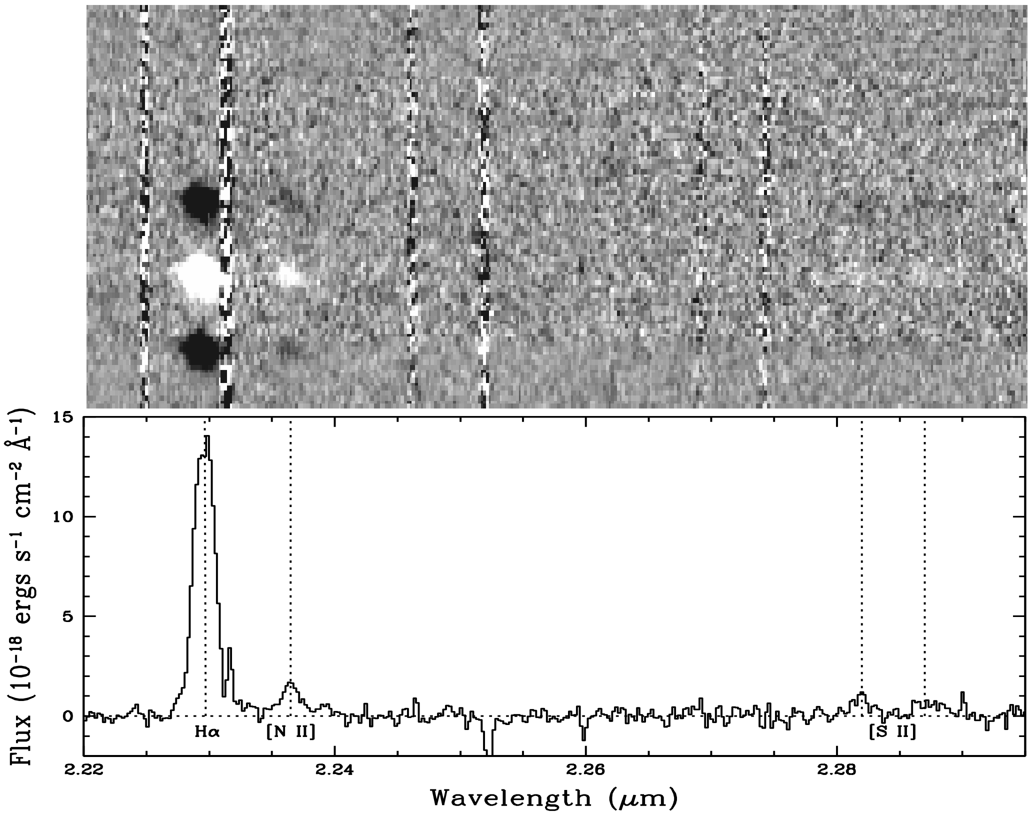

Figure 4.5 (Top) Example MOSFIRE 2D spectrum for object BX490 produced from the MOSFIRE Data Reduction Pipeline. (Bottom) Corresponding 1D spectrum after extraction and flux calibration. The emission lines Hα, [N II]λ6584, and [S II]$\lambda\lambda$6717,6732 are labeled from left to right.

Table 4.1. Physical Properties In The HS1700 Field

Object	$z_{\mathrm{H}\alpha}$	$\mathcal{R}$[a]	K_s[a,b]	M_*[c]	$F_{\mathrm{H}\alpha}$[d]	$F_{[NII]}$[d]	12 + log(O/H)[e]	σ[f]	SFR[g]
Protocluster Galaxies									
BNB19[h]	2.2850	23.33	–	–	6.7±0.6	1.2±0.2	8.48±0.02	103^{+18}_{-18}	12
BM658	2.2939	25.29	–	0.3	1.0±0.1	<0.1	<8.37	43^{+14}_{-17}	2
BX505[i]	2.3094	25.17	22.7	4.4	4.9±0.2	2.3±0.3	8.71±0.03	89^{+6}_{-6}	21
BX563	2.2924	23.82	22.29	2.0	11.1±0.2	1.0±0.2	8.30±0.01	108^{+2}_{-2}	44
BX585	2.3085	24.71	23.35	0.5	3.9±0.2	<0.2	<8.18	93^{+7}_{-7}	10
BX649	2.2960	24.90	23.3	1.8	5.6±0.3	1.1±0.2	8.49±0.01	60^{+4}_{-4}	15
BX684[h]	2.2935	23.51	–	–	7.0±0.3	1.1±0.3	8.44±0.02	95^{+6}_{-6}	12
BX689[h]	2.2840	23.90	–	–	8.4±0.5	1.1±0.2	8.39±0.01	71^{+7}_{-7}	15
BX710	2.2960	23.96	22.03	3.6	15.8±0.2	1.7±0.2	8.35±0.01	91^{+2}_{-2}	50
BX711	2.2962	25.07	22.68	6.3	11.0±0.3	0.8±0.2	8.25±0.01	51^{+2}_{-2}	35
BX759	2.3096	24.43	23.08	1.3	2.2±0.3	<0.3	<8.43	28^{+8}_{-10}	9
BX763	2.2932	24.25	22.79	1.5	7.1±0.2	1.1±0.2	8.44±0.01	54^{+3}_{-3}	19
BX789[h]	2.3006	25.16	–	–	3.1±0.4	<0.4	<8.36	92^{+20}_{-20}	5
BX810	2.2937	24.68	22.61	2.3	9.9±0.4	1.5±0.3	8.43±0.01	108^{+4}_{-4}	32

Table 4.1—Continued

Object	$z_{\mathrm{H}\alpha}$	$\mathcal{R}$[a]	K_s[a,b]	M_*[c]	$F_{\mathrm{H}\alpha}$[d]	$F_{[NII]}$[d]	12 + log(O/H)[e]	σ[f]	SFR[g]
BX879	2.3077	23.50	22.38	1.2	3.7±0.3	0.7±0.1	8.50±0.02	39^{+6}_{-6}	16
BX893	2.3092	24.38	23.2	2.7	1.7±0.3	<0.3	<8.46	30^{+13}_{-18}	4
BX909	2.2949	23.73	22.27	3.7	14.8±0.4	1.6±0.3	8.35±0.01	113^{+4}_{-4}	47
BX913	2.2918	23.88	22.41	4.3	4.4±0.2	0.6±0.1	8.39±0.01	38^{+3}_{-4}	18
BX917	2.3081	24.43	21.88	7.6	14.0±0.5	2.1±0.3	8.43±0.01	158^{+7}_{-7}	47
BX918	2.3078	24.34	22.89	1.8	5.0±0.4	<0.7	<8.42	165^{+11}_{-11}	12
BX929	2.3081	23.83	22.88	1.9	5.0±0.5	<0.3	<8.18	51^{+7}_{8}	12
BX935[h]	2.2860	25.18	–	–	4.2±0.4	<0.3	<8.27	73^{+13}_{-13}	7
BX939	2.2984	24.46	22.92	0.6	7.9±0.4	<0.4	<8.16	70^{+6}_{-6}	28
BX950	2.2968	24.51	22.51	1.5	3.3±0.3	<0.5	<8.43	73^{+6}_{-7}	10
BX951	2.3067	23.17	21.89	2.7	5.4±0.3	1.1±0.3	8.51±0.02	70^{+5}_{-5}	16
BX984	2.2976	23.51	21.97	2.3	10.3±0.4	1.1±0.3	8.34±0.01	127^{+8}_{-8}	26
MD109	2.2950	25.46	23.62	1.6	2.5±0.2	<0.2	<8.32	64^{+9}_{-9}	7
MD69	2.2899	24.85	21.9	20.1	9.4±0.4	2.8±0.2	8.60±0.01	129^{+4}_{-4}	42

Table 4.1—Continued

Object	$z_{\mathrm{H}\alpha}$	$\mathcal{R}$[a]	K_s[a,b]	M_*[c]	$F_{\mathrm{H}\alpha}$[d]	$F_{[NII]}$[d]	12 + log(O/H)[e]	σ[f]	SFR[g]
Field Galaxies									
BM568	2.3901	24.72	–	1.1	2.1±0.2	<0.3	<8.41	<12	4
BM619	2.2668	24.04	–	1.1	7.4±0.2	<0.8	<8.34	51^{+2}_{-2}	20
BX490	2.3973	22.88	21.84	1.2	30.2±0.4	3.4±0.2	8.36±0.01	109^{+2}_{-2}	110
BX535	2.6382	25.16	23.46	2.9	4.4±0.5	<0.3	<8.27	89^{+14}_{-14}	22
BX575	2.4348	23.82	22.74	0.6	8.8±1.1	<0.6	<8.22	156^{+32}_{-32}	26
BX592	2.4746	24.87	–	0.8	2.2±0.2	<0.2	<8.33	48^{+8}_{-9}	9
BX604	2.2012	24.72	23.17	1.1	4.6±0.2	<0.4	<8.28	67^{+5}_{-5}	10
BX609	2.5714	24.12	23.2	0.8	6.2±0.5	<0.4	<8.23	115^{+15}_{-15}	25
BX625	2.0768	24.52	23.7	0.6	3.1±0.2	0.3±0.1	8.31±0.01	85^{+8}_{-8}	5
BX632	2.2353	25.12	–	1.7	1.8±0.3	<0.1	<8.25	57^{+9}_{-9}	4
BX691	2.1912	25.33	22.53	9.9	9.6±0.3	1.9±0.3	8.50±0.01	127^{+4}_{-4}	29
BX708	2.4006	23.92	23.46	0.7	6.7±0.5	<0.3	<8.11	64^{+8}_{-8}	27
BX713	2.1394	24.48	23.03	4.7	4.9±0.2	0.4±0.2	8.27±0.02	52^{+4}_{-4}	12
BX717	2.4371	24.78	23.74	0.8	3.7±0.2	<0.3	<8.24	51^{+4}_{-4}	10
BX752	2.4016	24.86	22.69	4.4	8.7±0.7	2.4±0.3	8.58±0.02	137^{+9}_{-9}	31

Table 4.1—Continued

Object	$z_{\mathrm{H}\alpha}$	$\mathcal{R}$[a]	K_s[a,b]	M_*[c]	$F_{\mathrm{H}\alpha}$[d]	$F_{[NII]}$[d]	12 + log(O/H)[e]	σ[f]	SFR[g]
BX772	2.3436	24.96	23.02	3.6	4.6±0.4	<0.3	<8.25	77^{+13}_{-14}	12
BX801	2.0393	24.11	–	1.0	9.7±0.3	<0.9	<8.31	85^{+3}_{-3}	25
BX880	2.4381	24.98	–	0.6	1.0±0.1	<0.1	<8.40	42^{+8}_{-9}	3
BX881	2.1822	24.99	23.95	0.4	1.3±0.2	<0.7	<8.76	93^{+26}_{-27}	3
MD77	2.5091	24.86	22.94	0.8	7.7±0.4	<0.3	<8.13	146^{+8}_{-8}	42

[a]Magnitudes are on the AB system.

[b]Objects with no reported K_s magnitude are not detected down to a 3σ limit of 24.05 AB.

[c]Stellar mass in units of 10^{10} $M_\odot$.

[d]Emission-line flux and error in units of 10^{-17} erg s^{-1} cm^{-2}.

[e]Errors listed are determined solely from emission-line flux measurements and do not include the systematic uncertainty in the $N2$ calibration.

[f]Velocity dispersion in units of km s^{-1}.

[g]Star-formation rates in units of $M_\odot$ yr^{-1}.

[h]Insufficient photometric data for stellar mass and $E(B-V)$ estimate. Object not included in MZR analysis. SFR not dust corrected.

[i]Gas-phase oxygen abundance above solar, where solar is defined as $12 + \log(\mathrm{O/H})_\odot = 8.66$.

4.4 Physical Properties

4.4.1 Stellar Masses

The stellar mass reveals the efficiency with which a galaxy has converted its gas into stars, making it an important physical property for understanding how galaxies form and evolve. I estimated the stellar masses for objects in this sample as in Reddy et al. (2012), using the full rest-frame UV through IR broadband spectral energy distribution (SED) to find the best-fit stellar population model. A brief overview of the procedure is described within this section.

Flux contribution from strong nebular emission lines can be a significant source of contamination to the observed photometry. Specifically, strong Lyα emission can enhance the flux in the U_n or G bands depending on redshift. In addition, the optical nebular emission line Hα can affect the measured K_s flux for the $z \sim 2$ HS1700 objects. The broadband photometry in the rest-frame ultraviolet was already adjusted for the effect of Lyα emission/absorption by Reddy et al. (2012) when the measurements were available. To adjust for Hα in the K_s band, I adopted the correction method described in Papovich et al. (2001), where the rest-frame equivalent width (EW) of the emission line, E_0, introduces a magnitude difference of

$$\Delta m = -2.5 \log[1 + \frac{E_0(1+z)}{\Delta\lambda}] \tag{4.1}$$

I corrected the rest-frame optical photometry by utilizing the Hα measurements obtained from the MOSFIRE spectra. There are a total of 11 objects that are not detected in K_s band and an additional 2 objects that have Hα redshifted out of the K band. For the remaining 34 objects the K_s-band magnitude was used to estimate the continuum flux density (corrected for line emission) and consequently EW of Hα, since none of the MOSFIRE spectra contain significant continuum. The average (median) magnitude difference calculated from the Hα emission line correction is $\Delta m = 0.14$ (0.12). Figure 4.6 demonstrates the difference in the estimated stellar masses when the corrected K_s-band magnitude is used.

Once the photometry was corrected for nebular emission, the spectral energy distribution (SED) for each galaxy was fit by applying the latest solar metallicity models of S. Charlot & G. Bruzual (in preparation) that include the Marigo & Girardi (2007) prescription for the thermally-pulsating Asymptotic Giant Branch (TP-AGB) evolution of low- and intermediate-mass stars. For each galaxy a constant, exponentially decreasing, and exponentially increasing star formation history (SFH) was considered. The best-fit model was determined by minimizing its χ^2 with respect to the observed $U_n G\mathcal{R}$+JK_s+F160W+IRAC (3.6-8.0μm) photometry. This minimization then determined the SFR, $E(B-V)$, age, and stellar mass for each object. An example SED model is shown in Figure 4.7.

I assume a constant SFH with a minimum allowed age of 50 Myr for all of the objects presented in this thesis. This minimum age limit is chosen to reflect the dynamical timescale as interpreted from velocity dispersion and size measurements of $z \sim 2$ UV-selected star-forming galaxies (Erb et al. 2006b; Law et al. 2012). Using an exponentially decreasing or increasing SFH does not change the conclusions from this study.

Stellar masses were estimated for 23 protocluster galaxies and all 20 field galaxies using the SED fitting procedure described above. Four protocluster galaxies (BX684, BX689, BX789, and BX935) do not have sufficient multi-wavelength broadband photometric coverage for accurate stellar mass estimates, and are not

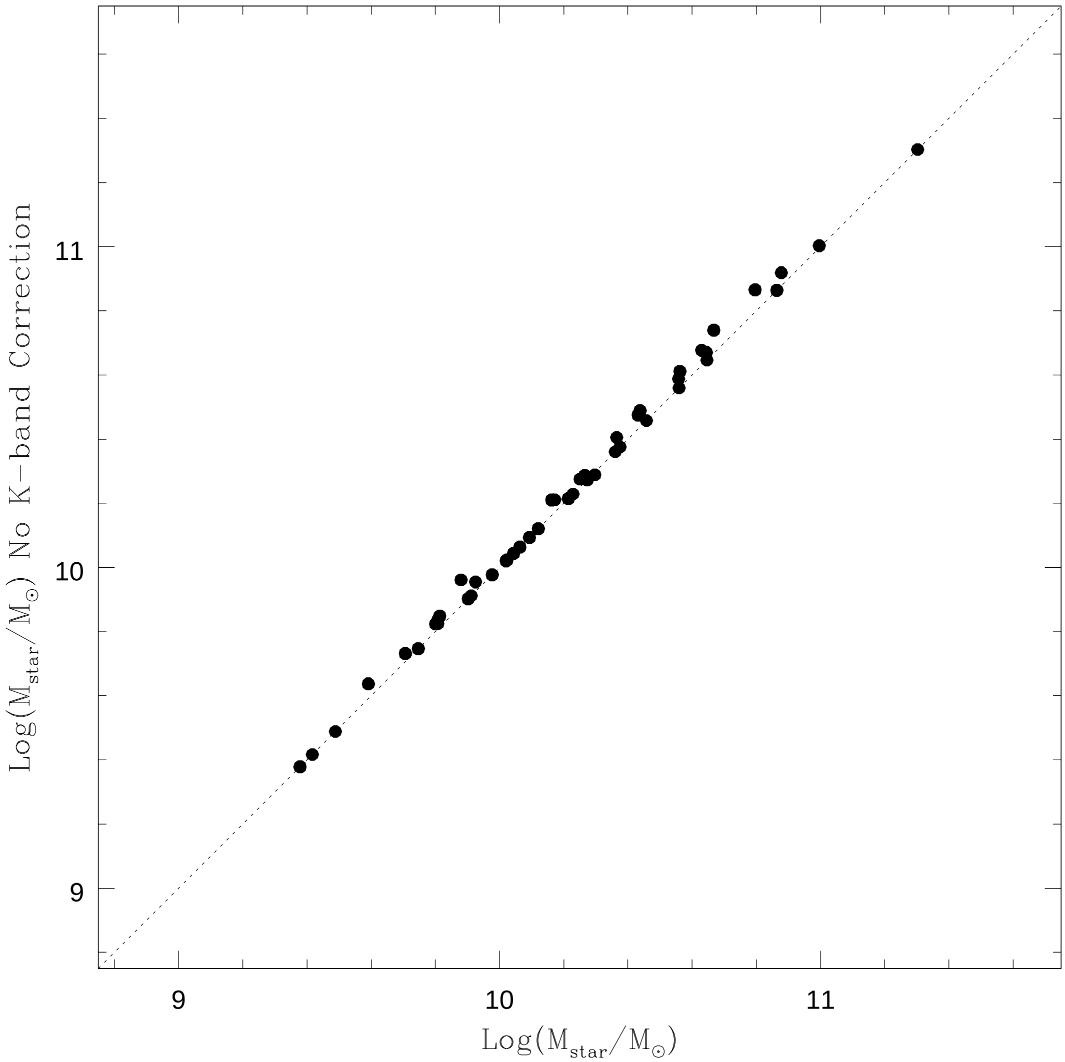

Figure 4.6 Comparison of estimated stellar masses with and without the K_s band corrected for Hα emission. The dotted line represents a one-to-one correlation. Without the correction, the stellar mass is typically over estimated, with an average (median) ratio of the difference in stellar mass to the corrected stellar mass of $\Delta M_\star/M_\star = 0.091$ (0.095).

included in the following mass-metallicity analysis. The stellar masses for the sample are listed in Table 4.1. The average stellar mass estimated for protocluster members, $M_* = 3.2 \times 10^{10}$ M$_\odot$, is approximately twice as large as that of the

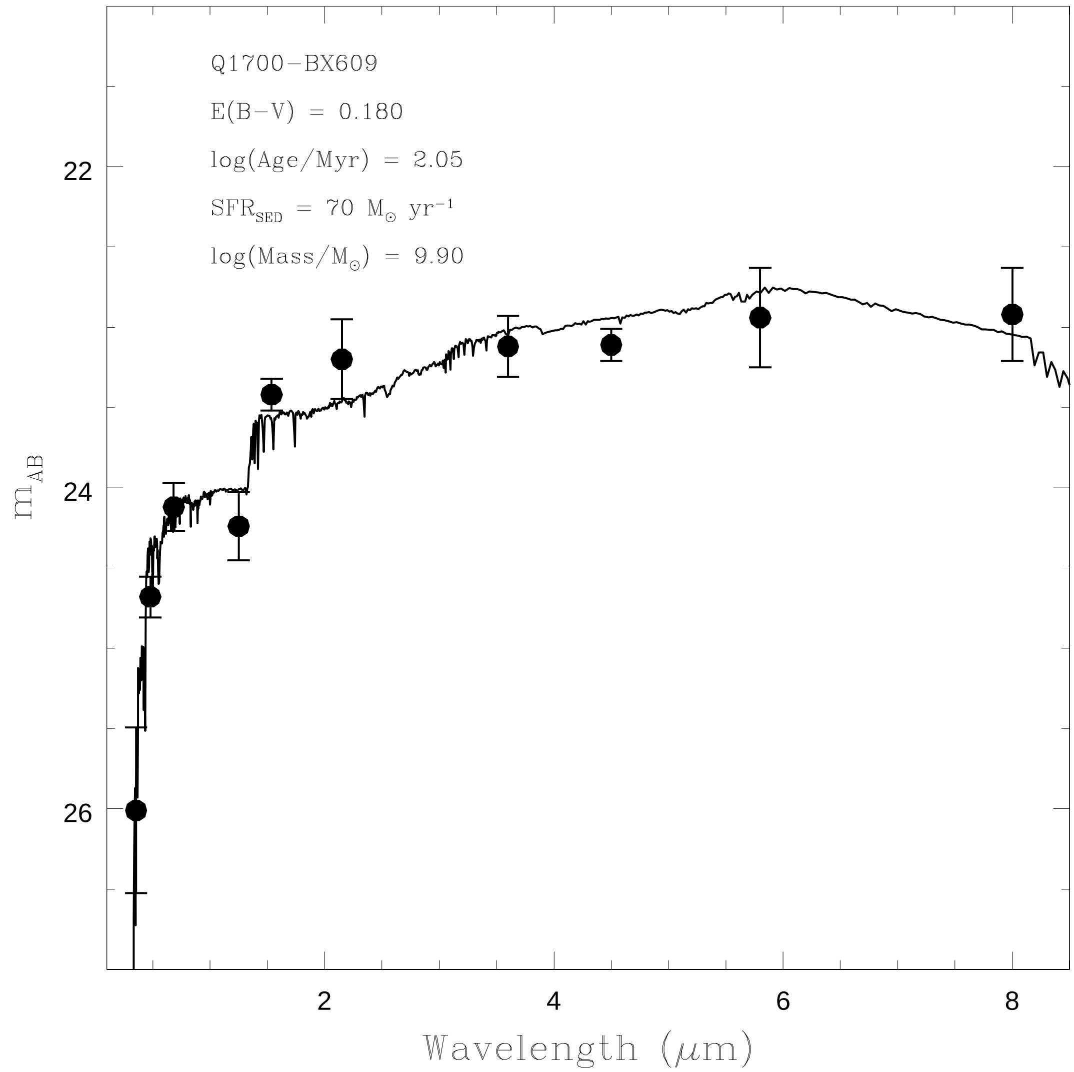

Figure 4.7 SED modeling for object BX609 using rest-frame ultraviolet through infrared broadband photometric data. The black line represents the best-fit stellar population synthesis model assuming a constant star formation history with a minimum allowed age of 50 Myr.

field galaxy sample, $M_* = 1.9 \times 10^{10}$ M$_\odot$, which suggests that the protocluster galaxies have experienced a more advanced build-up in stellar mass compared to field galaxies. This mass difference between protocluster and field galaxies was already noted by Steidel et al. (2005).

4.4.2 Metallicities

Gas-phase metallicity reflects the entire past history of star formation, in addition to being affected by infall of metal-poor gas and outflow of metal-enriched gas (Finlator & Davé 2008; Davé et al. 2011, 2012). There are several different methods typically used for evaluating the metallicity in a galaxy. The most direct method employs the ratio between the [O III]λ4363 auroral line and lower excitation lines such as [O III]$\lambda\lambda$5007,4959, which allows a direct measurement of the oxygen abundance via the electron temperature (T_e) of the gas. However, [O III]λ4363 is a very weak emission line in lower-metallicity galaxies and decreases at higher metallicities (Kakazu et al. 2007). Galaxies observed at high redshift are not only fainter, but most UV-selected galaxies identified to date are not particularly metal deficient, making the [O III]λ4363 too weak to detect. Due to the difficulties in measuring the gas-phase metallicity with the direct method, empirical calibrations have been developed, which fit a relationship between the "direct" T_e method and strong-line ratios in H II regions.

To determine the metallicity, I used the $N2$ indicator, defined as $N2 \equiv \log([\text{N II}]\lambda6584/\text{H}\alpha)$, which traces gas-phase oxygen abundance (Pettini & Pagel 2004). Since Hα and [N II] are close in wavelength, systematic uncertainties in $N2$ from dust extinction, flux calibration, and instrumental effects are insignificant. However, one drawback of $N2$ is the saturation of this ratio above solar metallicity, making it an unreliable tracer of metallicity in this regime. To calculate $N2$, I measured the flux for Hα and [N II] simultaneously using a fixed central wavelength and FWHM based on the best-fit parameters for Hα, which is the brighter line. A combined fit was obtained for both emission lines by fitting Gaussian profiles using the `IRAF` task, `splot`.

I employed a Monte Carlo technique to measure the uncertainties in the centroid, flux, and FWHM. For each object, 500 fake spectra were created by perturbing the flux at each wavelength of the true spectrum by a Gaussian random number with the standard deviation set by the level of the 1σ error spectrum. Line measurements were obtained from the fake spectra in the same manner as the actual data. The standard deviation of the distribution of measurements from the artificial spectra was adopted as the error on the centroid, flux, and FWHM. For objects with no detected [N II] emission, 500 simulated spectra were created in the same manner as described above to measure upper limits. The flux was summed at the nominal position of [N II] over an interval defined by the extent of the measured $H\alpha$ emission line above the continuum in each simulated spectra. I defined the 1σ upper limit as the standard deviation of the distribution of the calculated flux from the artificial spectra.

To determine the gas-phase oxygen abundance from $N2$, I used the calibration from Pettini & Pagel (2004), which was established from a linear fit to a large sample of local extragalactic H II regions with both $N2$ measurements and direct T_e-based oxygen abundance estimates. According to this calibration,

$$12 + \log(\mathrm{O/H}) = 8.90 + 0.57 \times N2 \tag{4.2}$$

This relation has an inherent 1σ dispersion of ± 0.18 dex, which is the dominant source of error in the metallicity measurements for individual galaxies. It should be noted that since the conversion between $N2$ and gas-phase oxygen abundance was calibrated from a sample of low-redshift galaxies, this conversion may not be valid for high-redshift galaxies (Shapley et al. 2005a; Liu et al. 2008). However, the differential nature of this study between protocluster and field galaxies at $z \sim 2$ mitigates the importance of this concern. Metallicities and uncertainties are listed for each object in Table 4.1.

4.5 Mass-Metallcity Relation

The existence of a correlation between the mass of a galaxy and the gas-phase metallicity was first noted in the late 1970s by Lequeux et al. (1979). Since then the correlation between metallicity and stellar mass has been firmly established for nearby galaxies and traced out to $z \sim 3$ for star-forming galaxies (Tremonti et al. 2004; Erb et al. 2006a; Kewley & Ellison 2008; Mannucci et al. 2009). The source of this relation, though, remains uncertain. Numerous models have been created to explain the origin and observed evolution of the MZR (e.g., Finlator & Davé 2008; Oppenheimer & Davé 2008; Davé et al. 2012). Observations of the MZR provide the much needed constraints for these galaxy formation models in order to understand how gas reservoirs are regulated in galaxies.

At $z \sim 0$ it has been demonstrated that galaxies found in overdense regions have enhanced gas-phase metallicities compared to field galaxies at the same stellar mass (Cooper et al. 2008; Ellison et al. 2009). At higher redshift, the relationship among mass, metallicity, and environment has not been well studied due to small sample sizes and a lack of robust environmental measurements. Examining the MZR with respect to environment provides a unique probe into how baryons cycle in and out of galaxies, and offers additional constraints on galaxy formation models. My measurements of gas-phase metallicities for galaxies within and surrounding the HS1700 protocluster present a unique opportunity for connecting metallicity and environment at early epochs.

Figure 4.8 shows the gas-phase metallicity versus stellar mass for protocluster (in red) and field galaxies (in black) in the sample. Downward arrows indicate 1σ upper limits. The data from Erb et al. (2006a) are also shown (in blue) in Figure 4.8. These authors examined the MZR based on the $N2$ indicator for a sample of 87 star-forming galaxies at $\langle z \rangle = 2.3$ binned by stellar mass to construct composite spectra. In contrast, the MOSFIRE data points are from *individual* objects. Measurements of individual galaxies are important to understand the inherent scatter of the MZR, in addition to enabling a more direct, object-by-object, comparison to other physical properties such as SFRs. The dotted curve is the MZR derived by Erb et al. (2006a) using the $N2$ indicator for ∼53,000 SDSS galaxies (Tremonti et al. 2004) after the application of a downward shift of 0.56 dex as implied by the Erb et al. 2006a data. The protocluster and field galaxies are distributed around the fit, with the majority appearing to fall below the Erb et al. (2006a) trend, which corresponds to a lower metallicity for a given stellar mass. The dashed horizontal line indicates the solar gas-phase oxygen abundance ($12 + \log(\mathrm{O/H})_{\odot} = 8.66$; Asplund et al. 2004), where the $N2$ indicator saturates. One of the HS1700 objects, BX505, has a measured gas-phase metallicity above solar.

To detect differences between the protocluster and field galaxy samples, I binned the galaxies by stellar mass and constructed composite MOSFIRE spectra for each bin. A caveat related to using composite spectra is that they do not reflect the scatter among the individual points. However, given that more than half of the objects in the sample have measured upper limits in [N II]/Hα, composite spectra offer the most robust method to examine the average [N II]/Hα ratio and corresponding metallicity in each bin. I created low- and high-mass bins for both protocluster and field samples. These bins were designed so that the average mass was roughly equivalent for the corresponding protocluster and field subsamples at both low and high mass. For the protocluster sample, there are 6 galaxies in the lower mass bin and 17 in the higher mass bin. For the field sample, there are 14 galaxies in the lower mass bin and 6 in the higher mass bin. To create the composite spectrum for each bin, I first shifted each individual spectrum into the rest frame using the redshift calculated from the observed Hα

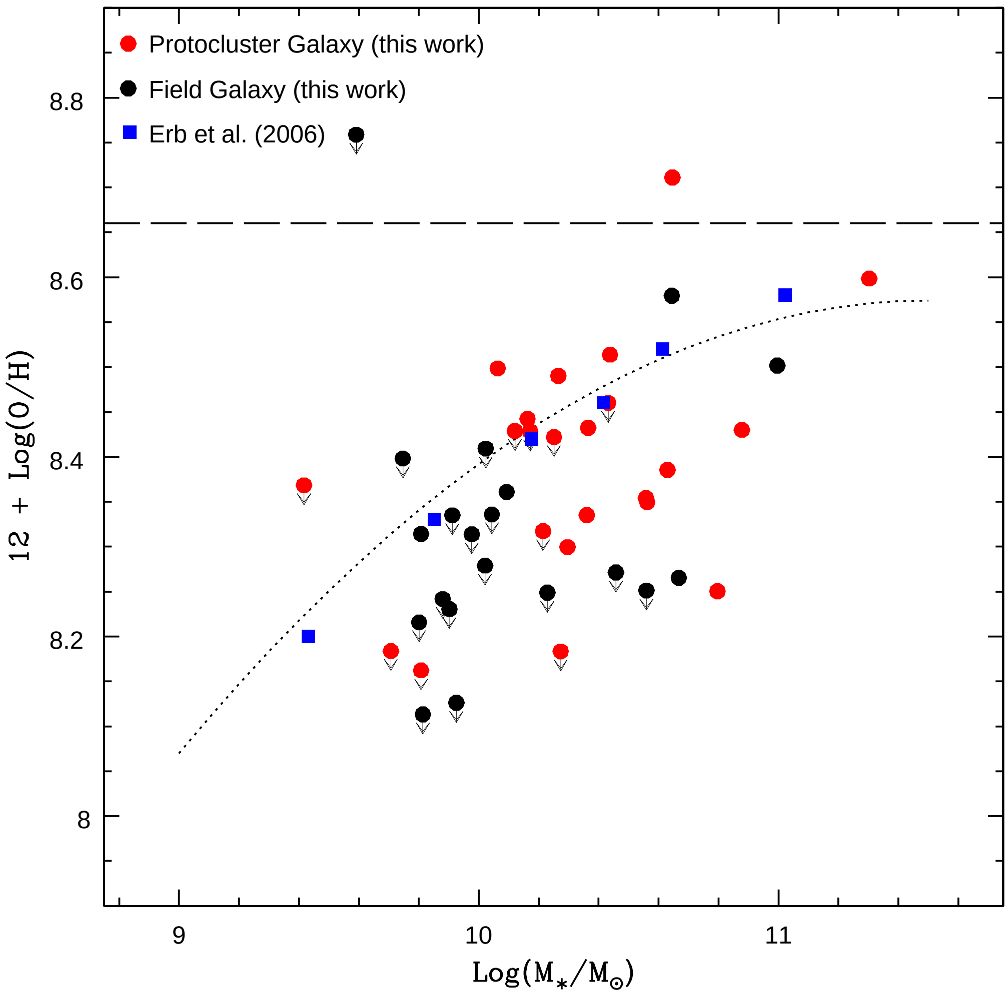

Figure 4.8 MZR for the protocluster (red circles) and field (black circles) galaxy samples at $z \sim 2$ using the $N2$ indicator. The dashed horizontal line represents solar abundance, where $N2$ saturates. The blue squares are from Erb et al. (2006a), indicating star-forming galaxies at $\langle z \rangle = 2.3$, based on composite spectra binned by stellar mass. The dotted curve is the MZR based on ~53,000 SDSS galaxies after an downward shift of 0.56 dex, as in Erb et al. (2006a). The error in metallicity is dominated by the systematic uncertainties from the $N2$ calibration, which is ± 0.18 dex.

wavelength. Next I converted each spectrum from F_λ to L_λ using the monochromatic luminosity distance to remove any redshift dependence on the observed flux:

$$L_\lambda = 4\pi D_L^2 \times (1+z) \times F_\lambda \tag{4.3}$$

where D_L is the luminosity distance. Finally, the `IRAF` task *scombine* was used to compute the average at each wavelength of the rest-frame spectra with a minimum/maximum pixel rejection (Figure 4.9). Hα and [N II] were measured and the corresponding $N2$-based metallicities were estimated for each composite spectrum in the same manner as described for the individual galaxies.

Figure 4.10 shows the gas-phase oxygen abundance calculated with the $N2$ index from each mass bin plotted versus the corresponding mean stellar mass. The horizontal bars show the range of stellar masses in each bin. The metallicity measurement errors were calculated from a Monte Carlo approach, where 500 fake spectra were made by bootstrap sampling the galaxies within each mass bin. The vertical metallicity error bars include the error from the $N2$ calibration of 12 + log(O/H), reduced by $N^{1/2}$ where N is the number of objects in the composite spectrum, as well as the uncertainties in the measurements of the Hα and [N II] fluxes from the bootstrap Monte Carlo method.

The field galaxies in Figure 4.10 show a clear trend similar to the one in Erb et al. (2006a), but shifted down by ~ 0.1 dex in metallicity at fixed stellar mass. To quantify the significance of this difference, I applied best-fit linear regressions to both the field galaxies and the Erb et al. (2006a) data. The parameters of the linear regressions to the Erb et al. (2006a) and field galaxy data sets are consistent within the 1σ errors, demonstrating that the two data sets are not significantly different.

Figure 4.10 also indicates that there is no strong correlation between stel-

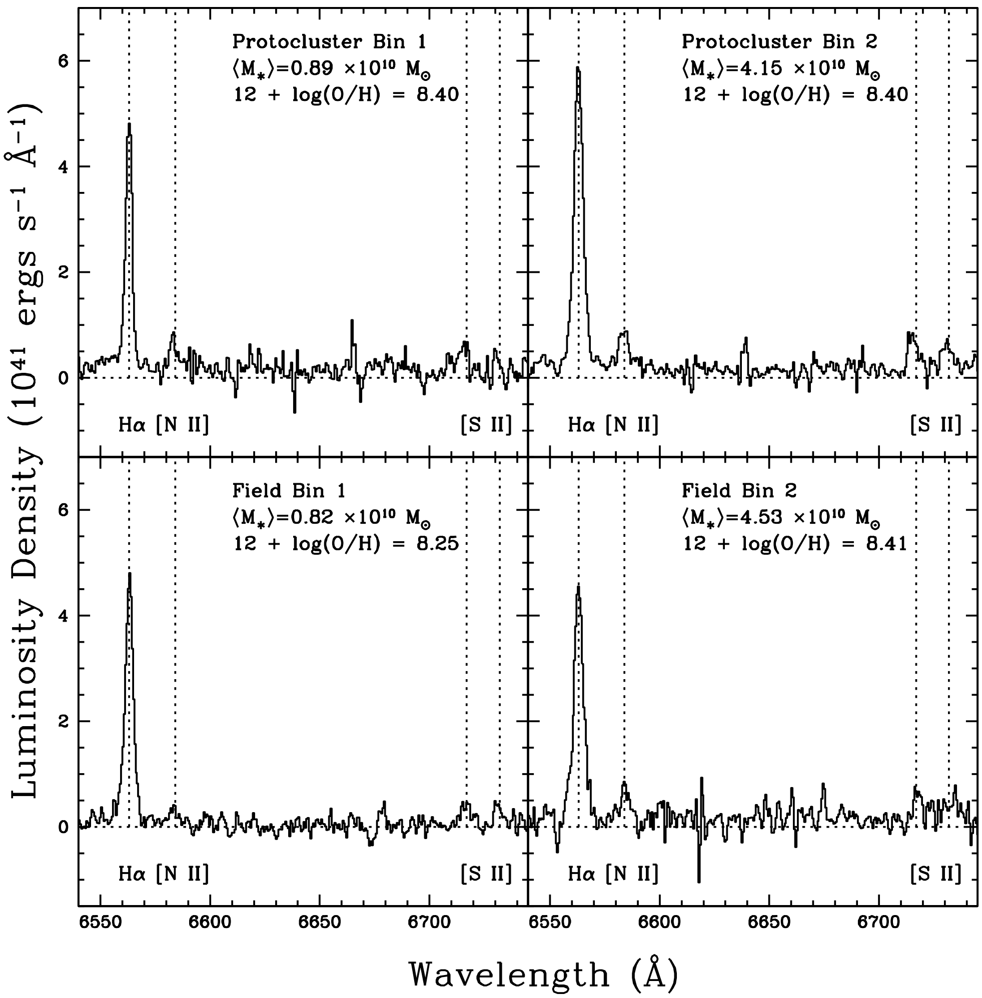

Figure 4.9 Rest-frame composite spectra for each protocluster and field galaxy bin. The first and second columns are, respectively, the low and high mass bins. The top row features protocluster galaxy composites and the bottom row shows the field galaxy composites. From left to right, Hα, [N II]λ6584, and [S II]$\lambda\lambda$6717,6732 are marked on each spectrum. In addition, each bins respective mean stellar mass and metallicity are labeled for each bin.

lar mass and metallicity for protocluster galaxies, with both mass bins having approximately the same measured gas-phase metallicity. A comparison between protocluster and field trends reveals that the high-mass protocluster and field bins are consistent with each other in metallicity. It is at lower masses that the

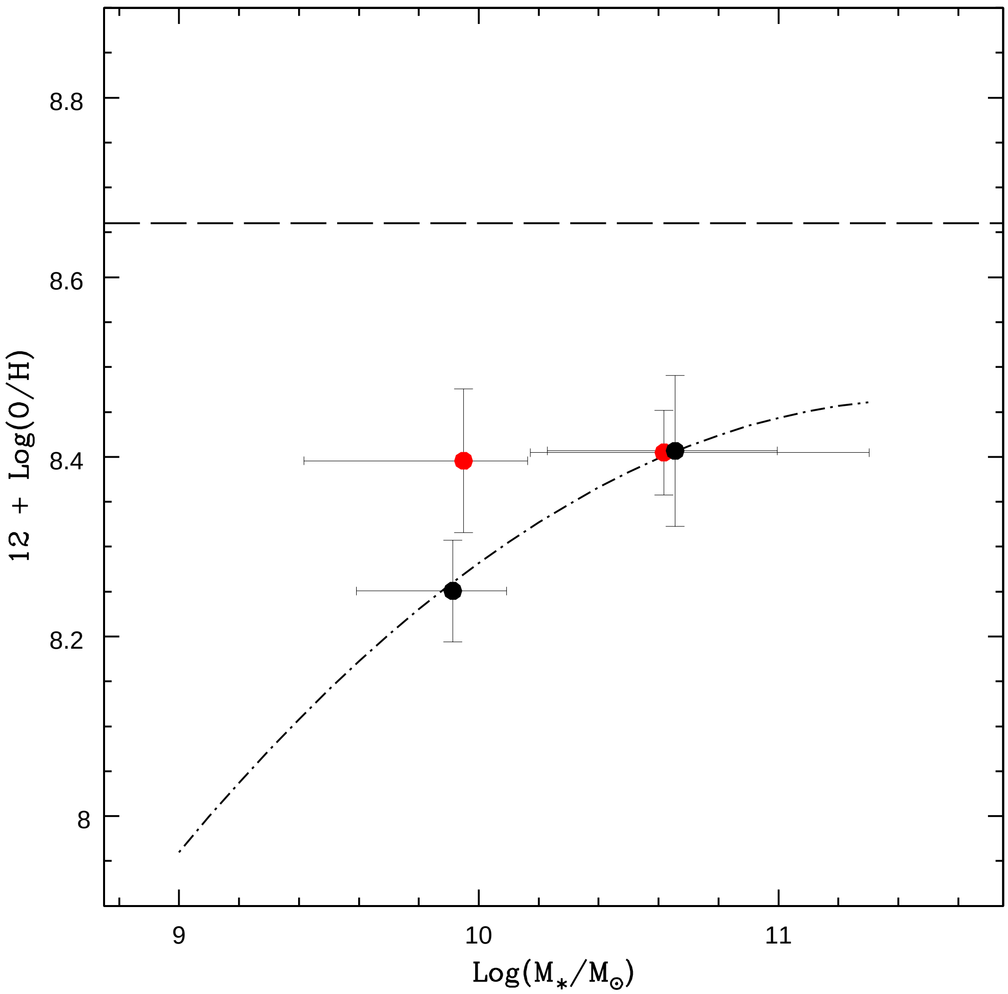

Figure 4.10 MZR for protocluster and field galaxies binned by stellar mass. The horizontal bars represent the mass range in each bin. The vertical error bars represent the 1σ error from the emission line measurements and the $N2$ calibration. The dotted line is the same as from Erb et al. (2006a) except that it has been shifted downward by 0.67 dex from the Tremonti et al. (2004) fit instead of 0.56 dex. The field galaxies appear to follow the trend presented in Erb et al. (2006a), while the protocluster galaxies show no strong correlation with mass and metallicity, with both protocluster galaxy mass bins having approximately the same measured gas-phase metallicity.

two samples diverge, with the protocluster metallicity significantly higher than that of the field sample.

4.6 Discussion

In this section, the physical mechanisms that may give rise to the observed $z \sim 2$ trends between environment and metallicity in the HS1700 field are discussed. Davé et al. (2011) utilize cosmological hydrodynamical simulations of galaxy formation to investigate how inflows, outflows, and star formation affect the metal content and gas fraction in a galaxy over cosmic time. Specifically, these authors examine the effect of local environment on the metallicities of simulated galaxies. In Davé et al. (2011) environment is defined by measuring the local galaxy density in a $1h^{-1}$ Mpc top-hat sphere. Galaxies at densities greater than 0.5σ above the mean are considered to reside in high-density regions. The Davé et al. (2011) simulations reveal an enhancement of the mean metallicity for objects found in overdense regions at $z = 0$ using either "momentum-driven winds" or "no-winds" models. Finlator & Davé (2008) also advance the model of momentum-driven winds to reproduce the MZR from Tremonti et al. (2004) at $z \sim 0$ and Erb et al. (2006a) at $z \sim 2$. Outflows have been shown to be ubiquitous for $z \sim 2-3$ UV-selected star-forming galaxies (Pettini et al. 2001; Shapley et al. 2003; Steidel et al. 2010). To verify the presence of outflows in the HS1700 sample, I examined the offset between the Lyα emission and interstellar absorption lines to the systemic redshift as calculated from Hα. The average offsets for the protocluster and field galaxies are, respectively, ~ 600 km s^{-1} and ~ 460 km s^{-1}, which supports the presence of winds. Therefore, the no-winds model clearly does not provide an accurate description of these systems, leaving the momentum-driven scenario. With this prescription for winds, the enhancement in metallicity disappears in galaxies with masses greater than 10^{11} M$_\odot$ (see Figure 14 in Davé et al. 2011).

Steidel et al. (2005) established that the HS1700 protocluster corresponds to a physical overdensity of $\frac{\Delta\rho}{\langle\rho\rangle} \sim 2$. Qualitatively, the momentum-driven winds model can replicate the MZR of the protocluster members if the assumption is made that the Davé et al. (2011) results for environmental dependence exist at $z \sim 2$ for an overdensity similar to that found in HS1700. In detail, Davé et al. use a different density estimator which makes a quantitative comparison not viable. In addition, these authors indicate that the environmental metallicity enhancement disappears at a stellar mass that is a factor of two more massive than suggested in my results. This discrepancy may be attributed to the difference in redshift between the Davé et al. simulated objects at $z = 0$ and the protocluster and field galaxies at $z \sim 2$ if the transition for the disappearance of the metallicity enhancement occurs at lower masses during earlier epochs.

Davé et al. (2011) suggest that the metallicity enhancement in overdense environments at $z = 0$ may be due to the differentially higher enrichment of intergalactic gas in such regions, resulting in cluster galaxies accreting additional metals compared with field galaxies. At $z \sim 2$, however, when the IGM has had less time for differential enrichment, the significance of this effect is unclear. Furthermore, the observed metallicity enhancement for HS1700 protocluster galaxies exhibits a mass dependence, with a larger metallicity offset at lower stellar masses. This mass dependence indicates that a general enhancement of the metallicity of infalling gas in an overdensity cannot alone explain the environmental MZR trend observed. Davé et al. (2011) turn to the results of Oppenheimer & Davé (2008) to explain the origin of a mass-dependent environmental trend in metallicity.

As reported by Oppenheimer & Davé (2008), environment is a primary factor determining how far winds can carry metals, and how long it will take for the metals to fall back into the galaxy and be "recycled." Specifically, these authors demonstrate in their simulation that the timescale for metals to be recycled is inversely correlated with environmental density, such that metals are recycled more rapidly in denser environments (see panel (b) of Figure 12 and Figure 14 in Oppenheimer & Davé 2008). Accordingly, low- to intermediate-mass protocluster galaxies will recycle their metals more efficiently due to residing in an overdense environment, compared with field galaxies of the same mass. However, at the highest masses, wind recycling is so effective that all galaxies re-accrete their ejected metals quickly regardless of environment. These mass-dependent results of wind recycling are reflected qualitatively in Figure 4.10, with an offset between the protocluster and field MZRs at lower stellar mass, but not at higher stellar mass. In detail, however, the actual high mass threshold at which the environmental effect disappears must also be matched. Models of galactic outflows at $z \sim 2$ including environments similar to the HS1700 overdensity are needed to investigate if the environmental dependence of wind recycling is a viable explanation for the MZR trends I observe.

4.7 Summary And Conclusions

I have utilized MOSFIRE data from the Keck Observatory to examine the gas-phase oxygen abundance of 23 protocluster and 20 field galaxies with respect to stellar mass in the HS1700 field. Metallicities were measured from the $N2 \equiv \log([\mathrm{N\ II}]/\mathrm{H}\alpha)$ indicator, while stellar masses were estimated from stellar population modeling of rest-frame UV through IR photometry. With these measurements, I first examined the correlation between stellar mass and metallicity for each *individual* galaxy and conclude that the sample is distributed around the Erb et al. (2006a) fit, with the majority of galaxies found below this trend corresponding to a lower metallicity for a given stellar mass. Next, I created composite spectra to study any differences in the MZR for protocluster and field galaxies. A high- and low-mass bin was created for both populations, where the bins were designed so that the average stellar mass was approximately equivalent for the corresponding protocluster and field subsamples at both low and high mass. The field composite data points are slightly lower but consistent with previous studies of $z \sim 2$ star-forming galaxies (i.e., Erb et al. 2006a) within the 1σ errors. The protocluster galaxies, however, demonstrate no strong correlation between metallicity and stellar mass. In detail, the protocluster and field high-mass bins for both samples are consistent, while the low-mass protocluster bin is measured to have a higher metallicity than that of the corresponding low-mass field bin.

To understand the physical mechanisms responsible for the observed environmental dependence on the MZR, I examined galaxy formation models present in the literature. Recent cosmological hydrodynamical simulations of galaxy formation suggest that winds carrying metals will recycle faster back to the host galaxy in an overdense environment, which may lead to cluster galaxies having enhanced gas-phase metallicity at moderate stellar mass. At high stellar masses, though, wind recycling is so effective that all galaxies re-accrete their ejected metals quickly. Qualitatively, these models can replicate the observed environmental trend demonstrated in the HS1700 field. Galaxy formation models featuring an environment similar to that in HS1700 at $z \sim 2$ needs to be investigated to quantify whether enriched infall caused by wind recycling provides a viable explanation for the observations presented here. This work represents the first analysis of an environmental dependence on the MZR at $z \sim 2$, a crucial step towards understanding how gas reservoirs are regulated in extreme environments during galaxy formation.

CHAPTER 5

Future Work

Galaxies form through numerous complex processes. While my thesis research represents an important step in comprehending how gas supplies are regulated during galaxies formation, there remains much work to fully understand the physical processes responsible for the formation and evolution of galaxies during the epoch of $z \sim 2-3$. With data I currently have in hand, I will continue to examine the role that various physical processes play in how galaxies form.

5.1 Project I Future Work

Developing detailed models of multiple-peaked Lyα emission profiles that utilize the constraints put forth by the Hα and [O III]λ5007 measurements I conducted during *Project I* of my thesis is an ongoing endeavor. Recently, great strides have been made towards creating more realistic Lyα radiative transfer models. Specifically, Dijkstra & Kramer (2012) have simulated clumpy gas outflows in non-spherical geometries. These authors demonstrate that a bi-polar clumpy outflow, similar to what is seen in local starburst galaxies, best reproduce the observed Lyα haloes that are discussed in Steidel et al. (2011). In the future, my collaborators and I plan to work together with the authors of Dijkstra & Kramer (2012) to create models constrained by the measured physical quantities described in *Project I* so as to reproduce the observed Lyα spectral line shape, while simultaneously replicating the observed interstellar absorption line features. I will compare these models to each of the objects presented in Kulas et al. (2012b) with respect to the systemic velocity of the galaxy, which will result in obtaining accurate estimates of the gas column density and mass outflow rates in $z \sim 2-3$ superwinds, representing a critical component of galaxy formation.

In addition, I have recently used NIRSPEC at Keck Observatory to observe Hα or [O III]λ5007 for 4 additional galaxies that show the signature of $infalling$ gas. These objects will increase the current sample size of galaxies that exhibit signs of actively accreting gas, allowing for a better statistical analysis. Future work will include translating these Lyα multiple-peaked profile into velocity space based on the Hα or [O III]λ5007 measurements. These profiles, along with the original two objects that demonstrate signatures of infalling gas, will then be examined with respect to Lyα radiative transfer models with the goal of accurately replicating the profile shapes and locations with respect to the systemic velocity. This analysis will provide estimates of gas mass $inflow$ rates and column densities where currently there are no observational constraints.

5.2 Project III Future Work

$Project\ III$ of my thesis examines the mass-metallicity relation with respect to environment at $z \sim 2$ by utilizing $K-$band data from MOSFIRE. The entire JHK spectroscopic data set of the HS1700 field can be used to examine numerous other physical properties besides metallicity and stellar mass that will lend insight into how gas supplies are controlled during galaxy formation. The Hα emission line can be used to measure the velocity dispersion of the galaxy, while the Hα luminosity, along with the $E(B-V)$ value calculated from the SED fitting, can be utilized to obtain dust-corrected star-formation rates (SFRs). This data set can also be used to examine the validity of the fundamental metallicity relation (FMR; Mannucci et al. 2010), which states that the stellar mass, metallicity, and SFR of star-forming galaxies are defined by a tight three-dimensional surface with no evolution from $z = 0 - 2.5$. In addition, the MOSFIRE JHK spectroscopy can be utilized to investigate whether UV-selected star-forming galaxies at $z \sim 2$ are offset from local star-forming galaxies on the Baldwin, Phillips and Terlevich diagram (BPT diagram; Baldwin et al. 1981), which has been noted in other high-redshift studies (e.g., Shapley et al. 2005a; Hainline et al. 2009), and if so, what are the possible physical mechanisms responsible for this offset.

5.2.1 Velocity Dispersion

The Hα emission line width can be used to investigate the velocity dispersion, which reflects the dynamics of the gas in the potential well within the central few kiloparsecs of the galaxy. The velocity dispersion results from random motions, rotation, merging, or most likely, some combination of all of these, in the interstellar gas. I have measured the velocity dispersion for all 28 protocluster galaxies and for 19 out of the 20 field galaxies. For the field galaxy, BM568, I estimated an upper limit on the velocity dispersion due to the measured line width not being significantly higher than the instrumental resolution. The velocity dispersion was calculated as $\sigma_v = (\text{FWHM}/2.355) \times (c/\lambda_{obs})$, where λ_{obs} is the observed wavelength of Hα. The intrinsic FWHM was determined by subtracting the instrumental FWHM, which was estimated from the widths of night sky lines, from the observed FWHM in quadrature.

Uncertainties in the velocity dispersion were determined using the method outlined in Erb et al. (2006c). I calculated an upper (lower) limit by taking the observed FWHM value and adding (subtracting) the standard deviation found from the Monte Carlo method described in Section 4.4.2. If the lower limit was less than the instrumental resolution, an upper limit was calculated as a 1σ standard deviation (i.e., for BM568). The mean values for the 28 protocluster galaxies and the 19 field galaxies are, respectively, $\langle\sigma_{v,proto}\rangle = 81 \pm 7$ km s^{-1} and $\langle\sigma_{v,field}\rangle = 83 \pm 10$ km s^{-1} (where the error represents the standard deviation of the mean, see left-hand side of Figure 5.1). Both populations have velocity dispersions that are similar to values found in other $z \sim 2$ UV-selected star-forming galaxy studies (e.g., Erb et al. 2006c; Kulas et al. 2012b). Velocity dispersion measurements and corresponding uncertainties for each galaxy are listed in Table 4.1.

The correlation between σ_v versus stellar mass has been examined by other $z \sim 2$ studies (e.g., Erb et al. 2006c; Förster Schreiber et al. 2009), but this relation has not been investigated with respect to environment at this redshift. The σ_v versus stellar mass for protocluster and field galaxies is plotted on the right-hand side of Figure 5.1. A rigorous analysis will be conducted to understand any observed trend the emerges between σ_v and stellar mass for objects in the HS1700 field.

5.2.2 Star-Formation Rates

The star-formation rates were calculated from the Hα luminosity using the equation defined in Kennicutt (1998a): SFR (M$_\odot$ yr^{-1}) = $4.389 \times 10^{-42} \times L_{\mathrm{H}_\alpha}$ (ergs s^{-1}). A Chabrier initial mass function (IMF) was assumed, which decreases the SFR by a factor 1.8 compared to a Salpeter IMF. To account for dust extinction, the $E(B-V)$ values calculated from the SED modeling were used with the Calzetti et al. (2000) extinction law. Field object BX490 appears to be a young galaxy which is rapidly forming stars, with a dust-corrected SFR of 110 $M_\odot$ yr^{-1}. Not

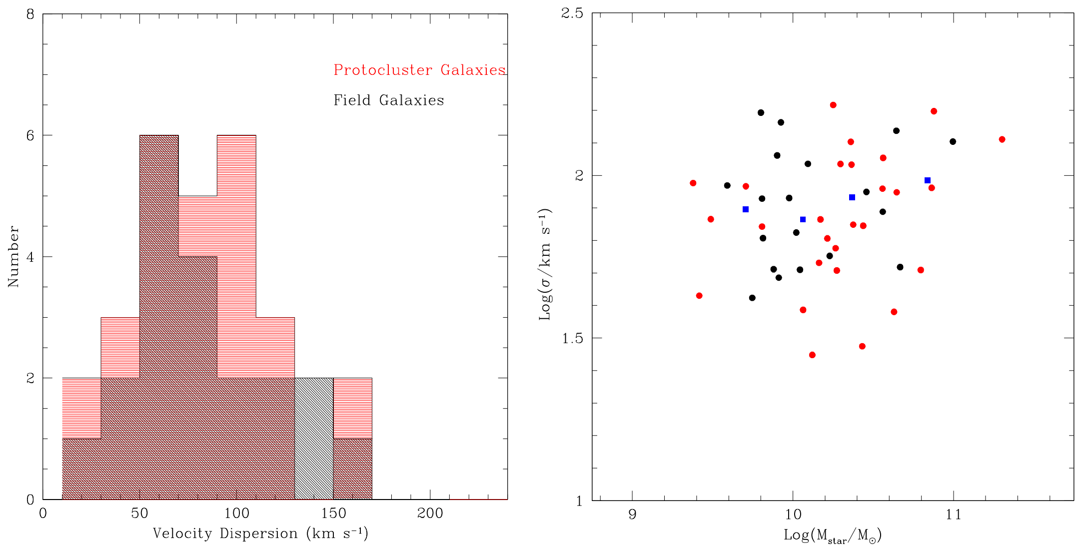

Figure 5.1 (Left) Histogram of the velocity dispersion, σ_v, for protocluster (red) and field (black) galaxies. The mean value of the velocity dispersion for the protocluster and field galaxies are, respectively, $\langle\sigma_{v,proto}\rangle = 81 \pm 7$ km s^{-1} and $\langle\sigma_{v,field}\rangle = 83 \pm 10$ km s^{-1}. (Right) The velocity dispersion versus the stellar mass. Red points are protocluster galaxies and back points are field galaxies. The blue squares represent the average σ_v in four stellar mass bins, where each mass bin is constructed with both protocluster and field galaxies and contain approximately the same number of objects.

including BX490, the average dust-corrected SFRs are 22 ± 14 $M_\odot$ yr^{-1} and 17 ± 12 $M_\odot$ yr^{-1}, respectively, for the protocluster and the field galaxy samples (see left-hand side of Figure 5.2). SFRs for each object is listed in Table 4.1.

The right-hand side of Figure 5.2 illustrates the relationship between SFR and stellar mass for the protocluster and field galaxies. A correlation between SFR and stellar mass has been demonstrated for other studies of $z \sim 2$ star-forming galaxies (e.g., Erb et al. 2006b; Daddi et al. 2007; Reddy et al. 2012), however it has not been examined with respect to environment at this redshift. It will be of interest to quantitatively examine the SFR-$M_\star$ relation for the MOSFIRE

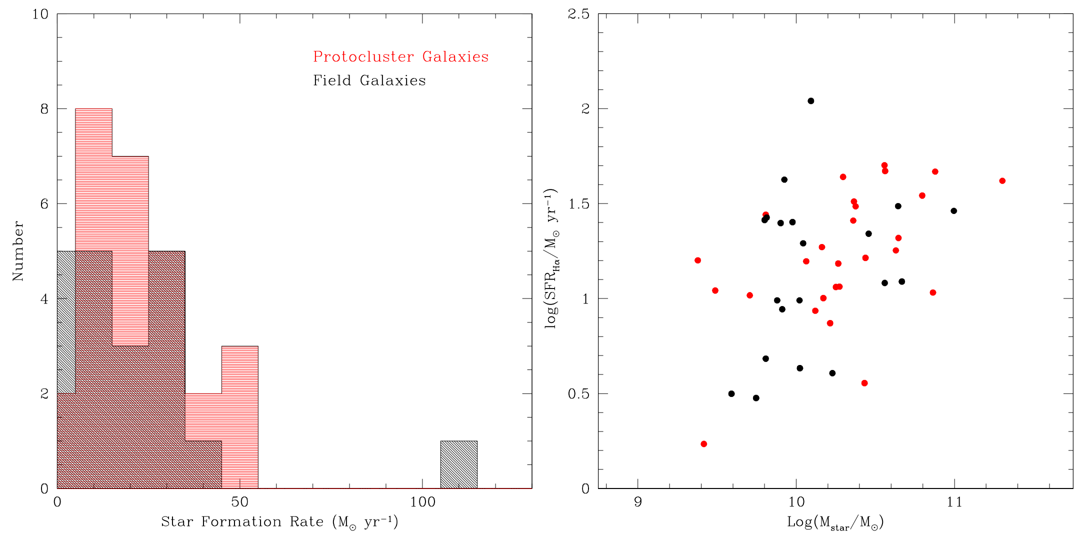

Figure 5.2 (Left) Histogram of the measured SFRs for protocluster (red) and field galaxies (black). The SFRs for the protocluster galaxies are slightly higher, 22 $M_\odot$ yr^{-1}, compared to the field galaxies, 17 $M_\odot$ yr^{-1}, when not including the field galaxy BX490, which appears to be a young object rapidly forming stars at a rate of 110 $M_\odot$ yr^{-1}. (Right) Relationship between SFR and stellar mass. Red points are protocluster galaxies and black points are field galaxies.

sample. In addition, further analysis with respect to other physical properties, such as metallicity, will provide additional insight into the processes responsible for any correlation that may be found.

The specific star-formation rate (sSFR; SFR per unit stellar mass) as a function of stellar mass is an additional relationship that has been studied for star-forming galaxies at high redshift (e.g., Bauer et al. 2005; Erb et al. 2006b; Reddy et al. 2006). The left-hand side of Figure 5.3 shows sSFR versus stellar mass for the protocluster and field galaxies. Future analysis will be done to interpret if the MOSFIRE sample shows the same correlation as other studies, in addition to investigating whether environment affects this relationship.

5.2.3 Fundamental Metallicity Relation

Recent evidence suggests a tight correlation among the stellar mass, metallicity, and SFR among local galaxies (Mannucci et al. 2010). All three of these properties can form a surface in a three-dimensional space which Mannucci et al. call the Fundamental Metallicity Relation (FMR). These authors claim that the FMR shows no evolution from $z = 0 - 2.5$, which would suggest the observed evolution of the mass-metallicity relation up to $z = 2.5$ is due to galaxies at higher redshift having larger SFRs, and consequently lower metallicities. Recently, Belli et al. (2013) have demonstrated good agreement with the FMR for lensed galaxies at $z \sim 2 - 3$.

In addition, Mannucci et al. (2010) assert that a projection onto the $M_\star$ and SFR axes significantly reduces the scatter of the observed metallicity. These authors define the quantity μ_α, which is a linear combination of $M_\star$ and SFR that they claim minimizes the dispersion of the metallicity: $\mu_{0.32} = M_\star - 0.32$ SFR. The right-hand side of Figure 5.3 shows the observed correlation of metallicity versus $\mu_{0.32}$ for the protocluster and field objects color coded by sSFR, which demonstrates how the MOSFIRE sample can be used to examine the validity of the FMR and analyze how environment may affect this observed relation.

5.2.4 The BPT Diagram

The Baldwin, Phillips and Terlevich diagram (BPT diagram; Baldwin et al. 1981) utilizes the [O III]/Hβ and [N II]/Hα ratios to determine the principal excitation mechanism, either star-formation or AGN activity, occurring inside of a galaxy. Star-forming galaxies reside in the lower left of the diagnostic diagram, while AGN occupy the space in the upper right. Kauffmann et al. (2003) deduced an empirical differentiation between where star-forming and AGN galaxies should be

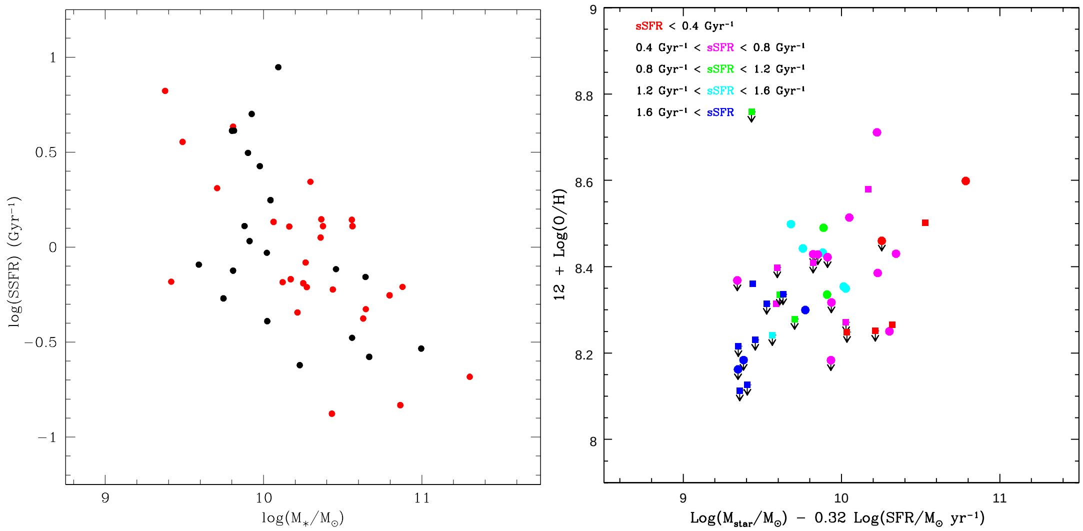

Figure 5.3 (Left) Specific star-formation rate (sSFR) with respect to stellar mass for both the protocluster galaxies (red) and field galaxies (black). (Right) Metallicity versus $\mu_{0.32}$ (which is defined as $\log(M_\star) - 0.32 \log(\mathrm{SFR})$ from Mannucci et al. 2010). Protocluster galaxies (circles) and field galaxies (squares) are both plotted. Galaxies are color coded with respect to sSFR (Gyr^{-1}): sSFR < 0.4 (red), $0.4 <$ sSFR < 0.8 (magenta), $0.8 <$ sSFR < 1.2 (green), $1.2 <$ sSFR < 1.6 (cyan), sSFR > 1.6 (blue).

located on the BPT diagram by using a large sample of local galaxies from the Sloan Digital Sky Survey (SDSS). In addition, Kewley et al. (2001) calculated a theoretical limit based on photoionization and stellar population synthesis models of where star-forming galaxies should reside.

Approximately forty $z \sim 2-3$ star-forming galaxies reported in the literature have had the measurements required for placement on the BPT diagram and around half of these galaxies are gravitationally lensed objects, which can increase the errors in line flux measurements due to uncertainties in the lensing modeling. The majority of these ~ 40 galaxies appear to be offset from the narrow region formed by local star-forming galaxies on the BPT diagram (e.g., Hainline et al. 2009; Richard et al. 2011). The source of this offset is uncertain, but has been attributed to differences between the physical conditions in local and high-redshift star-forming galaxies (Shapley et al. 2005a; Brinchmann et al. 2008). Larger sample sizes of individual galaxies will help to constrain the cause of this offset, which will provide greater insight into the physical conditions and chemical abundances of the gas supplies that fuel star formation in galaxies. In addition, it is important to understand how high-redshift galaxies differ from local samples since empirically calibrated conversion factors, such as abundance indicators, assume that high-redshift objects, on average, are similar to the low-redshift objects on which the calibration is based.

Currently, my sample MOSFIRE consists of 27 $z \sim 2$ star-forming galaxies that have both [O III] and Hα, significantly increasing the number of *individual non-lensed* high-redshift galaxies that can be placed on the BPT diagram. Figure 5.4 displays these objects on the BPT diagram with the local sample of SDSS star-forming galaxies over plotted in contours. The majority of the objects are offset in the same location on the BPT diagram as demonstrated by the previous high-redshift studies, with an enhanced [O III]/Hβ for a given [N II]/Hα.

Brinchmann et al. (2008) compare spectral evolution models to SDSS local galaxy spectra to analyze the relationship between [O III]/Hβ and [N II]/Hα. These authors find that the high-redshift galaxies are experiencing much higher levels of star formation than galaxies at lower redshift with the same stellar mass. Brinchmann et al. (2008) conclude that the upward shift in the BPT diagram can be attributed to a larger reservoir of ionizing photons from the higher rate of star formation. This increase in the number of ionizing photons will be evident in the ionization parameter, which describes the ratio between the density of ionizing photons to the density of hydrogen atoms within a radius r from the ionizing source, as has been suggested from theoretical modeling of nebular emission from star-forming galaxies (e.g., Kewley et al. 2001).

The ionization parameter can be written as

$$U \propto (Q\ n_e\ \epsilon^2)^{1/3} \tag{5.1}$$

where Q is the rate of hydrogen ionizing photons, ϵ is the volume filling factor of the gas, and n_e is the number density of hydrogen (Charlot & Longhetti 2001). The number density can be examined with the [S II]$\lambda\lambda$6717,6732 line ratio. Hainline et al. (2009) measured the [S II] ratio in two lensed $z \sim 2$ galaxies and found densities of $\sim 10^3$ cm^{-3}, which is an order of magnitude higher than what is typically found in local star-forming galaxies (e.g., Liu et al. 2008; Pilyugin et al. 2010). High values of n_e, such as those found by Hainline et al., could produce an increase in the ionization parameter. A total of nine objects from the HS1700 MOSFIRE sample that can be placed on the BPT diagram have detected [S II] emission lines, enabling the study of the offset from the BPT diagram compared to the electron density with respect to environment, which has previously not been examined. I leave this analysis to future work.

The ionization parameter can be estimated from the O_{32} parameter ([O III]$\lambda\lambda$4959,5007/[O II]$\lambda\lambda$3726,3729), which requires J- and H-band spectroscopic data for $z \sim 2$ objects. I have recently obtained J-band and higher quality H-band spectroscopic data for the HS1700 field on 2013 May 24th and 31st and June 1st, which will allow for the direct measurement of the ionization parameter. The O_{32} parameter, however, is strongly dependent on metallicity as discussed in Kewley & Dopita (2002). The [O II]$\lambda\lambda$3726,3729 lines are excited by relatively hot electrons and so diminish in cooler, higher-metallicity HII regions. In addition, [O III]$\lambda\lambda$4959,5007 decreases rapidly at higher metallicity regimes, causing a decrease in the O_{32} parameter. A comparison of O_{32} for low- and high-redshift galaxies must be examined at fixed metallicity to discriminate between this effect. I will be able to discern whether the ionization parameter is indeed different for $z \sim 2$ star-forming galaxies versus low-redshift objects since I have metallicity measurements for the MOSFIRE HS1700 sample. The investigation of the O_{32} parameter is left to future work.

Finally, in addition to the examination of the HS1700 protocluster, I have also obtained HK spectroscopy for a protocluster at $z = 3.09$ found in the SSA22a field using the MOSFIRE instrument. The SSA22a field has a comprehensive ancillary data set that consists of UV spectroscopy (Steidel et al. 2003), ground-based optical, near-IR and *Spitzer* mid-IR photometry (Uchimoto et al. 2008), HST/ACS (Geach et al. 2009), NB Lyα imaging (Matsuda et al. 2004), and X-ray data (Lehmer et al. 2009). There are 27 Lyman Break Galaxies (LBGs) spectroscopically confirmed within the SSA22a spike, with an additional 130 Lyman Alpha Emitters (LAEs) and 2 extended Lyα blobs. With the HK spectroscopic data, I will measure the [O II], [O III], and Hβ emission lines for protocluster and field galaxies. From these emission lines, I will examine the velocity dispersion, metallicity from the R_{23} indicator, the electron temperature, the electron density from [O II]$\lambda\lambda$3726,3729 and the local ionization state in the HII regions. Analysis of this protocluster will extend the understanding of galaxy formation to an earlier epoch and will allow for a detailed investigation of possible evolutionary trends between $z \sim 3$ and $z \sim 2$ in overdense environments. I plan to continue the research discussed in this chapter during my postdoctoral position at the NASA Ames Research Center.

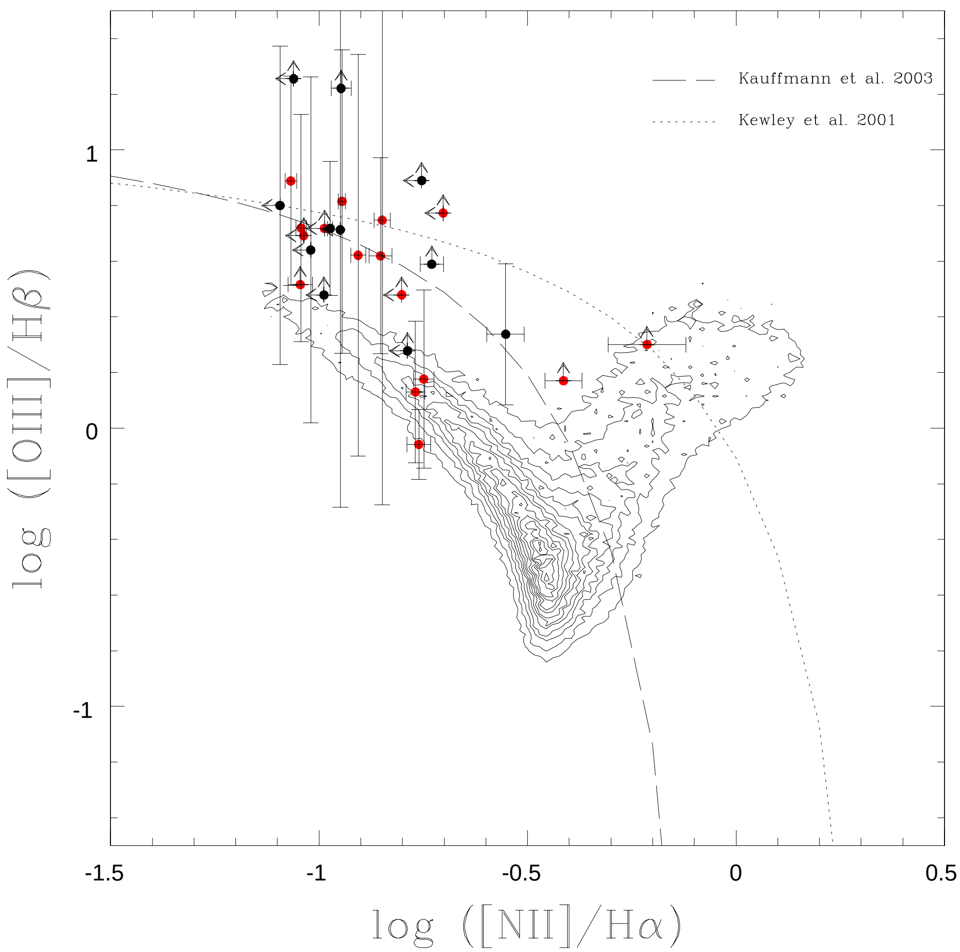

Figure 5.4 Preliminary analysis of the diagnostic BPT diagram for the HS1700 protocluster (red) and field (black) galaxies. Contours are local galaxies from the SDSS. The majority of the high-redshift galaxies in the HS1700 field show an offset compared to the local star-forming sample. The MOSFIRE JHK spectroscopic data set for this sample will offer a unique probe into understanding the cause of this offset.

CHAPTER 6

Conclusion

Understanding how galaxies form and evolve over cosmic time remains one of the crucial unresolved questions in astronomy. The epoch of $2-3$ Gigayears after the Big Bang, corresponding to $z \sim 3$ and $z \sim 2$, respectively, is a particularly advantageous time to study galaxy formation since it coincides with the peak of the global star formation rate of galaxies (e.g., Bouwens et al. 2009). During this time period galaxies are building up the bulk of their stellar mass. In addition, large-scale outflows and cold inflows are prevalent, which are expected to regulate the amount of gas available for star formation. For my doctoral thesis, I worked on the development of the MOSFIRE instrument, a powerful new infrared spectrograph for ground-breaking observations of the high-redshift universe. Concurrently, I applied near-infrared observations obtained from the Keck 10-meter telescopes to advance the understanding of the physical processes involved in the formation of galaxies at $z \sim 2-3$.

6.1 Constraining Galaxy Formation Models With Multiple-Peaked Lyα Emission Profiles

Outflows have been demonstrated to be universal among high-redshift UV-selected star-forming galaxies, yet estimates of fundamental physical quantities such as gas column densities and mass outflow rates in these superwinds have remained difficult to estimate. Determining the values of these parameters are crucial to understand the affect these outflows have on the amount of gas available to form stars, as well the chemical enrichment and thermodynamics of the surrounding intergalactic medium (IGM). The Lyα feature is one of the most widely used probes of galactic-scale winds. In principle, since Lyα is a resonant line, the structure of the resultant emission feature reflects the velocity field and density distribution of the gas through which it has emerged. Specifically, the morphology of multiple-peaked Lyα emission profiles increases the number of measurable outflow properties compared to a single-peaked profile.

I have utilized a large database of high-redshift objects with Lyα emission to determine the frequency of multiple-peaked systems, which had previously never been examined. This analysis provides a global perspective on the potential of using Lyα morphology to reveal $z \sim 2-3$ gaseous structure. I created a systematic algorithm which determined that $\sim$30% of UV-selected star-forming galaxies at $z \sim 2-3$ with Lyα emission contain multiple-peaked profiles. From this analysis I have shown that multiple-peaked Lyα emission profiles can be used to statistically examine the velocity field and density distribution of the gas surrounding these objects.

I obtained measurements of Hα ($z \sim 2$) or [O III]λ5007 ($z \sim 3$) using the NIRSPEC instrument (McLean et al. 1998) at Keck Observatory for 18 of the UV-selected star-forming galaxies with multiple-peaked Lyα emission. For each object I have calculated accurate systemic redshifts, nebular line widths, and intrinsic ionizing photon fluxes to remedy the lack of observational constraints for galaxy formation models. One of the simple models that has been commonly compared with individual spectra is that of an expanding shell of gaseous material (Verhamme et al. 2006, 2008; Schaerer & Verhamme 2008). In order to investigate whether such a system could reproduce the observed profiles, I used the radiative transfer code developed in Zheng & Miralda-Escudé (2002) and Kollmeier et al. (2010) to generate the observed Lyα spectra emerging from expanding/infalling shell models similar to those presented in Verhamme et al. (2006). I found significant discrepancies between the models and all 18 multiple-peaked Lyα emission profiles, demonstrating that the location of the multiple-peaked Lyα profile *and* interstellar absorption features must be established in velocity space to constrain the gas density and velocity distribution in large-scale outflows.

In addition, recent hydrodynamical cosmological simulations suggest that there should be large amounts of *infalling* gas at these same redshifts, fueling the observed large star-formation rates (e.g., Kereš et al. 2009). Observationally, though, this has remained a challenge to confirm. Two of the multiple-peaked Lyα emission profiles show evidence of infalling gas. These profiles may represent the elusive observational signature of accreting pristine gas. Recently, I have observed Hα or [O III]λ5007 for four other multiple-peaked Lyα emission profiles that demonstrate possible signatures of infalling gas to gain a larger statistical sample size, which will allow for more robust constraints to be placed on the existing models.

This analysis of multiple-peaked Lyα emission profiles is an important initial step in understanding the physical properties of outflowing gas. These constraints can enable an accurate estimate of the rate at which gas is flowing in and out of galaxies, which represents one of the major goals in the study of galaxy formation.

6.2 Advanced Astronomical Instrumentation With MOSFIRE

The continuous development of innovative instrumentation is critical to advance the study of galaxy formation. For over 4 years I was part of the instrumentation team for the Multi-Object Spectrometer For Infrared Exploration (MOSFIRE) instrument, which was lead by Dr. Ian McLean. MOSFIREs' characteristics of being a near-infrared multi-object spectrograph makes it ideal for the detailed examination of $z \sim 2 - 3$ star-forming galaxies. Specifically, the important rest-frame optical emission lines will shift into the near-infrared by $z \sim 2$, while the multi-object aspect will enable large statistical samples to be observed in a fraction of the time compared to a single-slit spectrograph.

My main project on the MOSFIRE instrument was to lead the characterization of the properties of the science-grade detector and ensure that MOSFIRE could reach the designated desired sensitivity limits. Over a period of several years, I measured the dark current, read noise, linearity, persistence, and the gain conversion, while simultaneously testing different voltage settings to find the optimal configuration for the detector. Dark current plus instrument background is measured at <0.008 e^- s^{-1} pixel^{-1} on average, which is a factor of ~100 improvement over previous generations of infrared detectors. Using Multiple Correlated Double Sampling (MCDS), a read noise value of less than 5e^- rms is achieved with 16 samples and the lowest noise of 3e^- rms occurs for 64 samples, which validates the ASIC's performance and verifies that MOSFIRE can reach the prescribed sensitivity goal. My measurements of charge persistence has demonstrated the dependence on exposure level and shows a large gradient across this detector. However, the decay time constant is always ~660 seconds regardless of different levels of illumination.

In addition, during my time as a MOSFIRE team member, I worked on the integration of the entire instrument. Furthermore, I validated the detectors performance on sky during the instrument commissioning, which took place during Spring of 2012. MOSFIRE is currently fully operational at Keck Observatory and is now producing important scientific data for research topics ranging from galaxy formation to exoplanet studies.

6.3 Examination Of A High-Redshift Protocluster

In the local universe an environmental trend has been well established, with massive quiescent early-type galaxies found in the central region of clusters while active late-type galaxies are located in the less dense areas. Protoclusters at $z > 2$ are still in the process of forming and have not yet virialized, making them perfect for studying the "seeds" of the environmental trend that is seen locally. I have used the MOSFIRE instrument to measure the important rest-frame optical emission lines (e.g., Hα, [O III], [N II], Hβ, [O II]) for a protoclusters at $z \sim 2$ in the HS1700 field to examine the physical processes that are relevant for galaxy formation in extreme environments.

The K-band data from MOSFIRE enables a detailed study of the mass-metallicity relation (MZR) with respect to environment at $z \sim 2$. I used Hα and [N II]λ6584 to determine the metallicity for the protocluster and field galaxy subsamples using the $N2 \equiv \log([\text{N II}]/\text{H}\alpha)$ strong-line indicator. In addition, I utilized the rest-frame UV to infrared photometry for modeling the SED to obtain estimates of the stellar mass for each galaxy. The final sample for the MZR analysis contained 23 protocluster and 20 field galaxies. Each individual object was examined with respect to the mass-metallicity diagram, in addition to being compared to the data from Erb et al. (2006a). Erb et al. used composites of 87 star-forming galaxies at $\langle z \rangle = 2.3$ binned by stellar mass. Measurements of *individual* galaxies are important for understanding the inherent scatter of the MZR, in addition to enabling a more direct, object-by-object comparison to other physical properties such as star-formation rates. The MOSFIRE data set revealed that the protocluster and field galaxies were distributed around the Erb et al. fit, with the majority falling below the trend.

Composite spectra were then made which consisted of low- and high-mass bins for both the protocluster and field galaxies in order to better detect any subtle differences between the two subsamples. The field galaxies follow the similar trend as that seen by previous studies, where more massive galaxies have larger metallicities. The protocluster galaxies, however, do not show a strong dependence of metallicity on stellar mass. Specifically, the low-mass bin for the protocluster galaxies displays an enhancement in metallicity with respect to the low-mass field bin, while the high-mass bins are consistent for both subsamples.

The environmental effect demonstrated by the protocluster galaxies can be qualitatively explained by wind recycling. Recent cosmological hydrodynamical simulations suggest that wind recycling becomes more efficient in denser environments, enabling lower-mass protocluster galaxies to re-accrete their metals faster compared to field galaxies of the same stellar mass. At high stellar masses, however, wind recycling is so effective that all galaxies re-accrete their ejected metals quickly regardless of environment. Detailed modeling will need to be performed to establish if wind recycling can quantitatively explain these observations of the MZR in overdense regions at high redshift. This research with MOSFIRE represents the first analysis of an environmental dependence on the MZR at $z \sim 2$, which will increase the understanding of how gas reservoirs are controlled in extreme environments during galaxy formation and provide the needed observational constraints for galaxy formation models.

6.4 Concluding Remarks

Galaxy formation is governed by a complex system of accreting and outflowing gas. The research discussed in this thesis examines how gas supplies are regulated in galaxies during the epoch when the global star-formation rate density was at a maximum. My dissertation has demonstrated the importance of near-infrared spectroscopy to comprehensively examine the physical processes occurring during galaxy formation. Furthermore, I have shown how innovative instrumentation like MOSFIRE is crucial to obtain ground-breaking observations of high-redshift galaxies. While the research presented here represents significant progress forward in understanding how galaxies form and evolve, it also highlights the importance of developing advanced models to accurately interpret the observations.

The future represents an exciting time for astronomy as new facilities such as the James Webb Space Telescope (JWST) and the Thirty Meter Telescope (TMT) come online. I will continue my research described in Chapter 5 as a NASA postdoctoral fellow to further the understanding of galaxy formation. In addition, during my postdoctoral tenure I will broaden my instrumentation knowledge by supporting the development of future NASA instruments for the SOFIA (Stratospheric Observatory For Infrared Astronomy) project. The results from my thesis will inform and guide subsequent studies to better interpret the complex processes that govern how galaxies form and evolve.

Bibliography

Adelberger, K. L., Steidel, C. C., Pettini, M., Shapley, A. E., Reddy, N. A., & Erb, D. K. 2005, ApJ, 619, 697

Adelberger, K. L., Steidel, C. C., Shapley, A. E., Hunt, M. P., Erb, D. K., Reddy, N. A., & Pettini, M. 2004, ApJ, 607, 226

Adelberger, K. L., Steidel, C. C., Shapley, A. E., & Pettini, M. 2003, ApJ, 584, 45

Ahn, S., Lee, H., & Lee, H. M. 2002, ApJ, 567, 922

Asplund, M., Grevesse, N., Sauval, A. J., Allende Prieto, C., & Kiselman, D. 2004, A&A, 417, 751

Baldwin, J. A., Phillips, M. M., & Terlevich, R. 1981, PASP, 93, 5

Barnes, L. A., Haehnelt, M. G., Tescari, E., & Viel, M. 2011, MNRAS, 416, 1723

Bauer, A. E., Drory, N., Hill, G. J., & Feulner, G. 2005, ApJL, 621, L89

Belli, S., Jones, T., Ellis, R. S., & Richard, J. 2013, ArXiv e-prints

Birnboim, Y. & Dekel, A. 2003, MNRAS, 345, 349

Bouwens, R. J., Illingworth, G. D., Franx, M., Chary, R.-R., Meurer, G. R., Conselice, C. J., Ford, H., Giavalisco, M., & van Dokkum, P. 2009, ApJ, 705, 936

Brinchmann, J., Pettini, M., & Charlot, S. 2008, MNRAS, 385, 769

Bruzual, G. & Charlot, S. 2003, MNRAS, 344, 1000

Calzetti, D., Armus, L., Bohlin, R. C., Kinney, A. L., Koornneef, J., & Storchi-Bergmann, T. 2000, ApJ, 533, 682

Chabrier, G. 2003, PASP, 115, 763

Charlot, S. & Longhetti, M. 2001, MNRAS, 323, 887

Clemens, M. S., Bressan, A., Nikolic, B., Alexander, P., Annibali, F., & Rampazzo, R. 2006, MNRAS, 370, 702

Cooke, J., Berrier, J. C., Barton, E. J., Bullock, J. S., & Wolfe, A. M. 2010, MNRAS, 403, 1020

Cooper, M. C., Tremonti, C. A., Newman, J. A., & Zabludoff, A. I. 2008, MNRAS, 390, 245

Daddi, E., Dickinson, M., Morrison, G., Chary, R., Cimatti, A., Elbaz, D., Frayer, D., Renzini, A., Pope, A., Alexander, D. M., Bauer, F. E., Giavalisco, M., Huynh, M., Kurk, J., & Mignoli, M. 2007, ApJ, 670, 156

Davé, R., Finlator, K., & Oppenheimer, B. D. 2011, MNRAS, 416, 1354

—. 2012, MNRAS, 421, 98

Dekel, A., Birnboim, Y., Engel, G., Freundlich, J., Goerdt, T., Mumcuoglu, M., Neistein, E., Pichon, C., Teyssier, R., & Zinger, E. 2009, Nature, 457, 451

Digby-North, J. A., Nandra, K., Laird, E. S., Steidel, C. C., Georgakakis, A., Bogosavljević, M., Erb, D. K., Shapley, A. E., Reddy, N. A., & Aird, J. 2010, MNRAS, 948

Dijkstra, M., Haiman, Z., & Spaans, M. 2006, ApJ, 649, 14

Dijkstra, M. & Kramer, R. 2012, MNRAS, 424, 1672

Dijkstra, M., Lidz, A., & Wyithe, J. S. B. 2007, MNRAS, 377, 1175

Ellison, S. L., Simard, L., Cowan, N. B., Baldry, I. K., Patton, D. R., & McConnachie, A. W. 2009, MNRAS, 396, 1257

Erb, D. K., Shapley, A. E., Pettini, M., Steidel, C. C., Reddy, N. A., & Adelberger, K. L. 2006a, ApJ, 644, 813

Erb, D. K., Shapley, A. E., Steidel, C. C., Pettini, M., Adelberger, K. L., Hunt, M. P., Moorwood, A. F. M., & Cuby, J. 2003, ApJ, 591, 101

Erb, D. K., Steidel, C. C., Shapley, A. E., Pettini, M., Reddy, N. A., & Adelberger, K. L. 2006b, ApJ, 647, 128

—. 2006c, ApJ, 646, 107

Fardal, M. A., Katz, N., Gardner, J. P., Hernquist, L., Weinberg, D. H., & Davé, R. 2001, ApJ, 562, 605

Finlator, K. & Davé, R. 2008, MNRAS, 385, 2181

Förster Schreiber, N. M., Genzel, R., Bouché, N., Cresci, G., Davies, R., Buschkamp, P., Shapiro, K., Tacconi, L. J., Hicks, E. K. S., Genel, S., Shapley, A. E., Erb, D. K., Steidel, C. C., Lutz, D., Eisenhauer, F., Gillessen, S., Sternberg, A., Renzini, A., Cimatti, A., Daddi, E., Kurk, J., Lilly, S., Kong, X., Lehnert, M. D., Nesvadba, N., Verma, A., McCracken, H., Arimoto, N., Mignoli, M., & Onodera, M. 2009, ApJ, 706, 1364

Fowler, A. M. & Gatley, I. 1990, ApJL, 353, L33

Fumagalli, M., Prochaska, J. X., Kasen, D., Dekel, A., Ceverino, D., & Primack, J. R. 2011, MNRAS, 418, 1796

Geach, J. E., Alexander, D. M., Lehmer, B. D., Smail, I., Matsuda, Y., Chapman, S. C., Scharf, C. A., Ivison, R. J., Volonteri, M., Yamada, T., Blain, A. W., Bower, R. G., Bauer, F. E., & Basu-Zych, A. 2009, ApJ, 700, 1

Hainline, K. N., Shapley, A. E., Kornei, K. A., Pettini, M., Buckley-Geer, E., Allam, S. S., & Tucker, D. L. 2009, ApJ, 701, 52

Hansen, M. & Oh, S. P. 2006, MNRAS, 367, 979

Hogg, D. W., Blanton, M. R., Brinchmann, J., Eisenstein, D. J., Schlegel, D. J., Gunn, J. E., McKay, T. A., Rix, H.-W., Bahcall, N. A., Brinkmann, J., & Meiksin, A. 2004, ApJL, 601, L29

Holden, B. P., Franx, M., Illingworth, G. D., Postman, M., van der Wel, A., Kelson, D. D., Blakeslee, J. P., Ford, H., Demarco, R., & Mei, S. 2009, ApJ, 693, 617

Kakazu, Y., Cowie, L. L., & Hu, E. M. 2007, ApJ, 668, 853

Kauffmann, G., Heckman, T. M., Tremonti, C., Brinchmann, J., Charlot, S., White, S. D. M., Ridgway, S. E., Brinkmann, J., Fukugita, M., Hall, P. B., Ivezić, Ž., Richards, G. T., & Schneider, D. P. 2003, MNRAS, 346, 1055

Kauffmann, G., White, S. D. M., Heckman, T. M., Ménard, B., Brinchmann, J., Charlot, S., Tremonti, C., & Brinkmann, J. 2004, MNRAS, 353, 713

Kelson, D. D. 2003, PASP, 115, 688

Kennicutt, Jr., R. C. 1998a, ARAA, 36, 189

—. 1998b, ApJ, 498, 541

Kereš, D., Katz, N., Fardal, M., Davé, R., & Weinberg, D. H. 2009, MNRAS, 395, 160

Kereš, D., Katz, N., Weinberg, D. H., & Davé, R. 2005, MNRAS, 363, 2

Kewley, L. J. & Dopita, M. A. 2002, ApJS, 142, 35

Kewley, L. J., Dopita, M. A., Sutherland, R. S., Heisler, C. A., & Trevena, J. 2001, ApJ, 556, 121

Kewley, L. J. & Ellison, S. L. 2008, ApJ, 681, 1183

Kodama, T., Tanaka, I., Kajisawa, M., Kurk, J., Venemans, B., De Breuck, C., Vernet, J., & Lidman, C. 2007, MNRAS, 377, 1717

Kollmeier, J. A., Zheng, Z., Davé, R., Gould, A., Katz, N., Miralda-Escudé, J., & Weinberg, D. H. 2010, ApJ, 708, 1048

Kornei, K. A., Shapley, A. E., Erb, D. K., Steidel, C. C., Reddy, N. A., Pettini, M., & Bogosavljević, M. 2010, ApJ, 711, 693

Kulas, K. R., McLean, I. S., & Steidel, C. C. 2012a, in Society of Photo-Optical Instrumentation Engineers (SPIE) Conference Series, Vol. 8453

Kulas, K. R., Shapley, A. E., Kollmeier, J. A., Zheng, Z., Steidel, C. C., & Hainline, K. N. 2012b, ApJ, 745, 33

Laursen, P., Razoumov, A. O., & Sommer-Larsen, J. 2009a, ApJ, 696, 853

Laursen, P., Sommer-Larsen, J., & Andersen, A. C. 2009b, ApJ, 704, 1640

Laursen, P., Sommer-Larsen, J., & Razoumov, A. O. 2011, ApJ, 728, 52

Law, D. R., Steidel, C. C., Shapley, A. E., Nagy, S. R., Reddy, N. A., & Erb, D. K. 2012, ApJ, 759, 29

Lehmer, B. D., Alexander, D. M., Chapman, S. C., Smail, I., Bauer, F. E., Brandt, W. N., Geach, J. E., Matsuda, Y., Mullaney, J. R., & Swinbank, A. M. 2009, MNRAS, 400, 299

Lequeux, J., Peimbert, M., Rayo, J. F., Serrano, A., & Torres-Peimbert, S. 1979, A&A, 80, 155

Liu, X., Shapley, A. E., Coil, A. L., Brinchmann, J., & Ma, C. 2008, ApJ, 678, 758

Madau, P. 1995, ApJ, 441, 18

Madau, P., Ferguson, H. C., Dickinson, M. E., Giavalisco, M., Steidel, C. C., & Fruchter, A. 1996, MNRAS, 283, 1388

Maiolino, R., Nagao, T., Grazian, A., Cocchia, F., Marconi, A., Mannucci, F., Cimatti, A., Pipino, A., Ballero, S., Calura, F., Chiappini, C., Fontana, A., Granato, G. L., Matteucci, F., Pastorini, G., Pentericci, L., Risaliti, G., Salvati, M., & Silva, L. 2008, A&A, 488, 463

Mannucci, F., Cresci, G., Maiolino, R., Marconi, A., & Gnerucci, A. 2010, MNRAS, 408, 2115

Mannucci, F., Cresci, G., Maiolino, R., Marconi, A., Pastorini, G., Pozzetti, L., Gnerucci, A., Risaliti, G., Schneider, R., Lehnert, M., & Salvati, M. 2009, MNRAS, 398, 1915

Marigo, P. & Girardi, L. 2007, A&A, 469, 239

Matsuda, Y., Yamada, T., Hayashino, T., Tamura, H., Yamauchi, R., Ajiki, M., Fujita, S. S., Murayama, T., Nagao, T., Ohta, K., Okamura, S., Ouchi, M., Shimasaku, K., Shioya, Y., & Taniguchi, Y. 2004, AJ, 128, 569

McLean, I. S. 2008, Electronic Imaging in Astronomy: Detectors and Instrumentation (Second Edition) (Praxis Publishing)

McLean, I. S., Becklin, E. E., Bendiksen, O., Brims, G., Canfield, J., Figer, D. F., Graham, J. R., Hare, J., Lacayanga, F., Larkin, J. E., Larson, S. B., Levenson, N., Magnone, N., Teplitz, H., & Wong, W. 1998, in Society of Photo-Optical Instrumentation Engineers (SPIE) Conference Series, Vol. 3354, Society of Photo-Optical Instrumentation Engineers (SPIE) Conference Series, ed. A. M. Fowler, 566–578

McLean, I. S., Steidel, C. C., Epps, H., Matthews, K., Adkins, S., Konidaris, N., Weber, B., Aliado, T., Brims, G., Canfield, J., Cromer, J., Fucik, J., Kulas, K., Mace, G., Magnone, K., Rodriguez, H., Wang, E., & Weiss, J. 2010, in Society of Photo-Optical Instrumentation Engineers (SPIE) Conference Series, Vol. 7735, Society of Photo-Optical Instrumentation Engineers (SPIE) Conference Series

McLean, I. S., Steidel, C. C., Epps, H. W., Konidaris, N., Matthews, K. Y., Adkins, S., Aliado, T., Brims, G., Canfield, J. M., Cromer, J. L., Fucik, J., Kulas, K., Mace, G., Magnone, K., Rodriguez, H., Rudie, G., Trainor, R., Wang, E., Weber, B., & Weiss, J. 2012, in Society of Photo-Optical Instrumentation Engineers (SPIE) Conference Series, Vol. 8446, Society of Photo-Optical Instrumentation Engineers (SPIE) Conference Series

McLinden, E. M., Finkelstein, S. L., Rhoads, J. E., Malhotra, S., Hibon, P., Richardson, M. L. A., Cresci, G., Quirrenbach, A., Pasquali, A., Bian, F., Fan, X., & Woodward, C. E. 2011, ApJ, 730, 136

Neufeld, D. A. 1990, ApJ, 350, 216

Oke, J. B., Cohen, J. G., Carr, M., Cromer, J., Dingizian, A., Harris, F. H., Labrecque, S., Lucinio, R., Schaal, W., Epps, H., & Miller, J. 1995, PASP, 107, 375

Oppenheimer, B. D. & Davé, R. 2008, MNRAS, 387, 577

Osterbrock, D. E. 1962, ApJ, 135, 195

—. 1989, Astrophysics of gaseous nebulae and active galactic nuclei

Papovich, C., Bassett, R., Lotz, J. M., van der Wel, A., Tran, K.-V., Finkelstein, S. L., Bell, E. F., Conselice, C. J., Dekel, A., Dunlop, J. S., Guo, Y., Faber, S. M., Farrah, D., Ferguson, H. C., Finkelstein, K. D., Häussler, B., Kocevski, D. D., Koekemoer, A. M., Koo, D. C., McGrath, E. J., McLure, R. J., McIntosh, D. H., Momcheva, I., Newman, J. A., Rudnick, G., Weiner, B., Willmer, C. N. A., & Wuyts, S. 2012, ApJ, 750, 93

Papovich, C., Dickinson, M., & Ferguson, H. C. 2001, ApJ, 559, 620

Patel, S. G., Kelson, D. D., Holden, B. P., Illingworth, G. D., Franx, M., van der Wel, A., & Ford, H. 2009, ApJ, 694, 1349

Peeples, M. S. & Shankar, F. 2011, MNRAS, 417, 2962

Peter, A. H. G., Shapley, A. E., Law, D. R., Steidel, C. C., Erb, D. K., Reddy, N. A., & Pettini, M. 2007, ApJ, 668, 23

Pettini, M. & Pagel, B. E. J. 2004, MNRAS, 348, L59

Pettini, M., Shapley, A. E., Steidel, C. C., Cuby, J., Dickinson, M., Moorwood, A. F. M., Adelberger, K. L., & Giavalisco, M. 2001, ApJ, 554, 981

Pilyugin, L. S., Vílchez, J. M., Cedrés, B., & Thuan, T. X. 2010, MNRAS, 403, 896

Quider, A. M., Pettini, M., Shapley, A. E., & Steidel, C. C. 2009, MNRAS, 398, 1263

Rauch, M., Becker, G. D., Haehnelt, M. G., Gauthier, J.-R., Ravindranath, S., & Sargent, W. L. W. 2011, MNRAS, 418, 1115

Reddy, N. A., Erb, D. K., Pettini, M., Steidel, C. C., & Shapley, A. E. 2010, ApJ, 712, 1070

Reddy, N. A., Pettini, M., Steidel, C. C., Shapley, A. E., Erb, D. K., & Law, D. R. 2012, ApJ, 754, 25

Reddy, N. A., Steidel, C. C., Fadda, D., Yan, L., Pettini, M., Shapley, A. E., Erb, D. K., & Adelberger, K. L. 2006, ApJ, 644, 792

Reddy, N. A., Steidel, C. C., Pettini, M., Adelberger, K. L., Shapley, A. E., Erb, D. K., & Dickinson, M. 2008, ApJS, 175, 48

Richard, J., Jones, T., Ellis, R., Stark, D. P., Livermore, R., & Swinbank, M. 2011, MNRAS, 413, 643

Rudie, G. C., Steidel, C. C., Trainor, R. F., Rakic, O., Bogosavljević, M., Pettini, M., Reddy, N., Shapley, A. E., Erb, D. K., & Law, D. R. 2012, ApJ, 750, 67

Schaerer, D. & Verhamme, A. 2008, A&A, 480, 369

Shapley, A. E., Coil, A. L., Ma, C., & Bundy, K. 2005a, ApJ, 635, 1006

Shapley, A. E., Steidel, C. C., Erb, D. K., Reddy, N. A., Adelberger, K. L., Pettini, M., Barmby, P., & Huang, J. 2005b, ApJ, 626, 698

Shapley, A. E., Steidel, C. C., Pettini, M., & Adelberger, K. L. 2003, ApJ, 588, 65

Smith, R. M., Zavodny, M., Rahmer, G., & Bonati, M. 2008, in Society of Photo-Optical Instrumentation Engineers (SPIE) Conference Series, Vol. 7021

Steidel, C. C., Adelberger, K. L., Shapley, A. E., Erb, D. K., Reddy, N. A., & Pettini, M. 2005, ApJ, 626, 44

Steidel, C. C., Adelberger, K. L., Shapley, A. E., Pettini, M., Dickinson, M., & Giavalisco, M. 2003, ApJ, 592, 728

Steidel, C. C., Bogosavljević, M., Shapley, A. E., Kollmeier, J. A., Reddy, N. A., Erb, D. K., & Pettini, M. 2011, ApJ, 736, 160

Steidel, C. C., Erb, D. K., Shapley, A. E., Pettini, M., Reddy, N., Bogosavljević, M., Rudie, G. C., & Rakic, O. 2010, ApJ, 717, 289

Steidel, C. C., Giavalisco, M., Pettini, M., Dickinson, M., & Adelberger, K. L. 1996, ApJL, 462, L17+

Steidel, C. C., Shapley, A. E., Pettini, M., Adelberger, K. L., Erb, D. K., Reddy, N. A., & Hunt, M. P. 2004, ApJ, 604, 534

Tapken, C., Appenzeller, I., Noll, S., Richling, S., Heidt, J., Meinköhn, E., & Mehlert, D. 2007, A&A, 467, 63

Tremonti, C. A., Heckman, T. M., Kauffmann, G., Brinchmann, J., Charlot, S., White, S. D. M., Seibert, M., Peng, E. W., Schlegel, D. J., Uomoto, A., Fukugita, M., & Brinkmann, J. 2004, ApJ, 613, 898

Uchimoto, Y. K., Suzuki, R., Tokoku, C., Ichikawa, T., Konishi, M., Yoshikawa, T., Omata, K., Nishimura, T., Yamada, T., Tanaka, I., Kajisawa, M., Akiyama, M., Matsuda, Y., Yamauchi, R., & Hayashino, T. 2008, PASJ, 60, 683 van der Wel, A., Bell, E. F., Holden, B. P., Skibba, R. A., & Rix, H.-W. 2010, ApJ, 714, 1779

Veilleux, S., Cecil, G., & Bland-Hawthorn, J. 2005, ARAA, 43, 769

Venemans, B. P., Röttgering, H. J. A., Miley, G. K., van Breugel, W. J. M., de Breuck, C., Kurk, J. D., Pentericci, L., Stanford, S. A., Overzier, R. A., Croft, S., & Ford, H. 2007, A&A, 461, 823

Verhamme, A., Schaerer, D., Atek, H., & Tapken, C. 2008, A&A, 491, 89

Verhamme, A., Schaerer, D., & Maselli, A. 2006, A&A, 460, 397

Wetzel, A. R., Tinker, J. L., & Conroy, C. 2012, MNRAS, 424, 232

Wylezalek, D., Galametz, A., Stern, D., Vernet, J., De Breuck, C., Seymour, N., Brodwin, M., Eisenhardt, P. R. M., Gonzalez, A. H., Hatch, N., Jarvis, M., Rettura, A., Stanford, S. A., & Stevens, J. A. 2013, ApJ, 769, 79

Yang, Y., Zabludoff, A., Jahnke, K., Eisenstein, D., Davé, R., Shectman, S. A., & Kelson, D. D. 2011, ApJ, 735, 87

Zheng, Z., Cen, R., Trac, H., & Miralda-Escudé, J. 2010, ApJ, 716, 574

Zheng, Z. & Miralda-Escudé, J. 2002, ApJ, 578, 33